

~~CONFIDENTIAL~~

NACA RM/A55C02



3 1176 00103 9149

~~NACA~~

# RESEARCH MEMORANDUM

THE UNSTEADY NORMAL-FORCE CHARACTERISTICS OF SELECTED  
NACA PROFILES AT HIGH SUBSONIC MACH NUMBERS

By Perry P. Polentz, William A. Page,  
and Lionel L. Levy, Jr.

Ames Aeronautical Laboratory  
Moffett Field, Calif.

CLASSIFICATION CHANGED

UNCLASSIFIED

LIBRARY COPY

JUN 1 1955

By authority of

*NACA Res. Dir. Effective*

*4 RN-113*

Date *3-19-57*

*NB 4-4-57*

LANGLEY AERONAUTICAL LABORATORY  
LIBRARY, NACA  
LANGLEY FIELD, VIRGINIA

CLASSIFIED DOCUMENT

This material contains information affecting the National Defense of the United States within the meaning of the espionage laws, Title 18, U.S.C., Secs. 793 and 794, the transmission or revelation of which in any manner to an unauthorized person is prohibited by law.

## NATIONAL ADVISORY COMMITTEE FOR AERONAUTICS

WASHINGTON

May 27, 1955

~~CONFIDENTIAL~~

[REDACTED]  
NATIONAL ADVISORY COMMITTEE FOR AERONAUTICSRESEARCH MEMORANDUMTHE UNSTEADY NORMAL-FORCE CHARACTERISTICS OF SELECTED  
NACA PROFILES AT HIGH SUBSONIC MACH NUMBERSBy Perry P. Polentz, William A. Page,  
and Lionel L. Levy, Jr.

## SUMMARY

A wind-tunnel investigation has been conducted at subsonic Mach numbers up to 0.9 and Reynolds numbers from 1 to 2 million to measure the root-mean-square variation of the normal forces on 27 representative NACA airfoil sections. The effects of thickness-chord ratio, camber, location of minimum pressure, and leading-edge radius were investigated. The principal statistical measures describing the unsteady normal force as a stationary random function of time were also determined. These measures are the spectral densities (sometimes referred to as generalized harmonic analyses) and the probability densities.

For Mach numbers of 0.75 and above, and lift coefficients below 0.6, maximum thickness was found to have the greatest effect on unsteady normal-force characteristics, reductions from 12 to 8 percent applied to the symmetrical NACA 65-series profiles diminishing the force as much as two-thirds. Decreases below 8 percent for these sections generally provided no further improvement, except in the small range of Mach numbers between 0.75 and 0.85 and for lift coefficients above 0.6. Camber up to 0.4 design lift coefficient had little influence on unsteady normal forces. A further increase to 0.6 design lift coefficient resulted in decreased magnitudes for the 12-percent-thick 65-series profiles even at Mach numbers as high as 0.88. The variations with position of minimum pressure and leading-edge radius were mostly unimportant, although an abnormally large leading-edge radius increased to some extent the magnitude of unsteady normal force.

Unsteady normal force was found to be a stationary random function of time with probability densities that are normally distributed. Representative spectral densities indicated that, for the 6-inch-chord models and the Reynolds numbers of the investigation, practically all of the unsteady normal force at low Mach numbers and high lift coefficients occurred at frequencies below 200 cycles per second. At high Mach numbers

[REDACTED]

and high unsteady normal-force coefficients; however, evidence was found that a significant proportion existed above this frequency.

Comparisons of buffet boundaries of four aircraft having straight wings, aspect ratios 4 to 6, with results for the corresponding airfoil sections show sufficiently good correlation at high Mach numbers and low lift coefficients to suggest that the wind-tunnel measurements of unsteady normal force on the profile are directly related to the buffeting found in flight.

Some of the unsteady force measurements were affected by the airfoil structure and spanwise variation of the unsteady forces. The methods derived to account for these effects, which make use of linear filter theory, the frequency response function of the airfoil structure, and the theory of stationary random time functions, may be useful in analyzing aircraft buffeting.

## INTRODUCTION

The buffeting of an airplane may be defined as an aerodynamically forced vibration of the airplane or of one or more of its components. Of the various recognized sources of buffeting - tail surfaces immersed in the wake of the wing, separated flow about the fuselage adjacent to locations such as the wing-fuselage juncture, and fluctuating lift on the wing associated with separated flow over the wing surface - the fluctuating lift is the least understood. The results reported in references 1 and 2 for the buffeting of tailless aircraft, moreover, indicate this source to be important, particularly at transonic Mach numbers.

Some wind-tunnel data concerning fluctuating lift on wings has been obtained from the measurement of pressure pulsations on the surfaces of airfoil sections reported in references 3 and 4, and from the instantaneous measurements of normal force described and discussed in reference 5. The present investigation was undertaken to supplement and amplify these results. In particular, it was desired to measure the unsteady normal forces of enough airfoil sections to determine the extent of occurrence and, in addition, the influence of the principal geometric parameters (maximum thickness, camber, position of minimum pressure, leading-edge radius) upon the unsteady force magnitudes.

The term "unsteady normal force" is defined as the difference between the mean and instantaneous values of normal force. It is distinguished from buffeting in that buffeting is a structural vibration; unsteady normal force is the force causing the vibration.

During the course of the investigation statistical analyses indicated that unsteady normal force is a stationary random process. Application of the theory of such processes (refs. 6, 7, and 8) to the unsteady force

problem determined the statistical functions required to define the process completely. The theory also suggested a means for relating unsteady normal force to the buffeting of elastic bodies. This relationship was applied to the airfoil models to obtain an alternative method for measuring unsteady normal forces. The successful outcome of this application suggested a procedure for relating aircraft buffeting to the unsteady normal force measured in two-dimensional flow; as a consequence, it may eventually be possible to predict, from wind-tunnel data, the buffeting of an airplane without the necessity of testing dynamically similar models. Because of its underlying importance, and relative unfamiliarity to aerodynamicists, a short account of the theory of stationary random functions of time is presented before discussion of the investigation itself.

## SYMBOLS

b	airfoil span, ft
$c_l$	section lift coefficient, dimensionless
$c_{l_i}$	design section lift coefficient, dimensionless
$c_n$	instantaneous section normal-force coefficient, dimensionless
$\Delta c_n$	instantaneous section unsteady normal-force coefficient, corrected, $\Delta c_n = c_n - \bar{c}_n$ , dimensionless
$\Delta c_n'$	instantaneous section unsteady normal-force coefficient, uncorrected, dimensionless
$\Delta c_{n_{av}}$	average of absolute value of section unsteady normal-force coefficient referred to the mean value, $\Delta c_{n_{av}} = \overline{ c_n - \bar{c}_n }$ , dimensionless
$\Delta c_{n_{rms}}$	root-mean-square-section unsteady normal-force coefficient, referred to the mean value, calculated from $\Delta c_{n_{av}}$ assuming the first-probability density to be normal, dimensionless
$\left[ \overline{(\Delta c_n')^2} \right]^{\frac{1}{2}}$	root-mean-square value of $\Delta c_n'$ , dimensionless
c	airfoil chord, ft

$E_W$	amplitude of output voltage of the wave analyzer, v
$e$	instantaneous value of a voltage wave form, v
$f$	frequency, cps
$f_A$	resonant frequency of airfoil model, cps
$f_T$	resonant frequency of wind tunnel, cps
$g(x,t)$	instantaneous normal loading per unit span, $\frac{\text{lb-force}}{\text{ft}}$
$G(f)$	spectral density, (time dependent variable) <sup>2</sup> /cps
$G_{\Delta c_n}(f)$	spectral density of uncorrected section unsteady normal-force coefficient, 1/cps
$G_{\Delta c_p}$	spectral density of the instantaneous pressure coefficient, 1/cps
$G_N(f)$	spectral density of unsteady normal force, (lb-force) <sup>2</sup> /cps
$j$	$\sqrt{-1}$ , dimensionless
$K$	constant of proportionality
$k$	elastic constant of the bending of the airfoil model caused by the normal force, lb-force/ft
$M$	Mach number, dimensionless
$m$	equivalent mass of airfoil model, slugs
$N$	instantaneous normal force on airfoil model, lb-force
$p$	pressure, lb-force/ft <sup>2</sup>
$R$	autocorrelation function, (time dependent variable) <sup>2</sup>
$r$	correlation coefficient, dimensionless
$S_{\Delta c_n} \left( \frac{cf}{U} \right)$	spectral density of uncorrected section unsteady normal-force coefficient normalized with respect to corresponding mean-square value of $\Delta c_n$ , dimensionless
$T$	time interval over which the average value of a function is computed, sec

t	time, sec
U	free-stream velocity, ft/sec
W	probability density of a stationary random function of time, dimensionless
x	distance along the airfoil span, ft
Y	frequency response function, dimensionless
y	time dependent variable of a stationary random function of time
y	variable of integration
$\alpha_0$	section angle of attack, deg
$\gamma$	velocity damping coefficient of airfoil model, $\frac{\text{lb-force}}{\text{ft/sec}}$
$\gamma_c$	critical velocity damping coefficient of airfoil model, $\frac{\text{lb-force}}{\text{ft/sec}}$
$\delta$	deflection of airfoil model at midspan caused by the normal force, ft
e	base of natural logarithms, dimensionless
$\lambda$	integral scale of correlation of normal loading per unit span, $\lambda = \int_0^{\infty} r(x)dx, \text{ ft}$
v	noise factor, a measure of the extraneous unsteady normal-force coefficient subtracted from $\Delta c_n'$ to obtain $\Delta c_n$ , dimension- less
$\tau$	time interval between two values of a stationary random function of time, sec
$\varphi$	frequency, used as a variable of integration, cps
$\omega$	angular frequency, radians/sec
$\omega_n$	undamped natural angular frequency of the airfoil models, radians/sec

## Superscripts

$\overline{y(t)}$  average with respect to time of a stationary time-dependent

$$\text{variable, } \overline{y(t)} = \lim_{T \rightarrow \infty} \frac{1}{T} \int_0^T y(t) dt$$

## Subscripts

A	airfoil
P	pressure cell
R	resonance compensating amplifier
S	strain gage
T	wind tunnel
TC	thermocouple meter
W	wave analyzer
i	input (except when used as $c_{i1}$ )
o	output (except when used as $\alpha_o$ )

## STATIONARY RANDOM FUNCTIONS OF TIME

A thorough understanding of the principles underlying the techniques developed for this project, and of many of the results obtained, depends upon a knowledge of the principles of the theory of stationary random processes. This theory has been employed extensively in the study of the effects of noise in communication networks, and in servomechanism theory (refs. 6 to 8). It has been found to be directly applicable to the investigation of unsteady normal forces on airfoil sections as well. The chief aspects of this theory therefore will be briefly recounted, emphasis being placed upon an orderly development from basic principles. An effort will also be made to explain the physical significance of the main concepts; and, further to impart a feeling for the subject, the relationships most frequently used in practice will be distinguished from those which are primarily of theoretical interest. The discussion will be confined to stationary random functions of time. A stationary random function of time

is not the same thing as a stationary random process. The distinction between the two, however, and the relation of one to the other (see refs. 7 and 8) involve the use of the ergodic hypothesis and other concepts, avoided here for the sake of simplification.

For the purpose of this report a random function of time is considered to be a single-valued function which varies in such a manner that no knowledge of previous values, however extensive or complete, is sufficient to predict any future value with certainty. Such a random function is stationary if the statistical quantities defining it are invariant with time and, hence, do not depend upon the origin selected for time measurements.

The fundamental quantities defining a stationary random function of time are the probability densities. For any stationary random function of time,  $y(t)$ , such as the one shown in part (a) of figure 1, it is possible to plot a histogram (fig. 1(b)) illustrating the proportion of total time the instantaneous amplitude lies between 0 and  $\Delta y$ , between  $\Delta y$  and  $2\Delta y$ , between  $2\Delta y$  and  $3\Delta y$ , etc. The choice of the interval  $\Delta y$  is arbitrary; allow it to approach zero. In the limit the discontinuous stepped curve of figure 1(b) will then approach the continuous curve of figure 1(c). The function represented by this continuous curve is the first probability density. It is a function of  $y$  only, and is not dependent upon time. Denoting this function as  $W_1(y)$ ,  $W_1(y_n)\Delta y$  represents the proportion of time the amplitude of  $y(t)$  lies in the interval between  $y_n$  and  $y_n + \Delta y$ . It also represents - and it is mainly for this reason that the concept is important - the probability of finding a value at any time  $t$  lying in such an interval.

In a similar manner, one may conceive of the joint probability of finding a pair of values of  $y$  at times  $t$  and  $t + \tau$  in the intervals  $(y_k, y_k + \Delta y_k)$  and  $(y_l, y_l + \Delta y_l)$ , respectively. This probability will be equal to the product of the two intervals and the second probability density; expressed symbolically it is  $W_2(y_k, y_l, \tau)\Delta y_k\Delta y_l$ . For a stationary random function of time this probability density likewise is not a function of time  $t$ , although it is dependent upon the time interval,  $\tau$ . Inasmuch as it is a function of the three independent variables,  $y_k$ ,  $y_l$ , and  $\tau$ , its graphic representation would require, in the general case, a space of four dimensions.

It is possible to continue in this fashion. One may thus obtain the third probability density,  $W_3(y_k, y_l, y_m, \tau_1, \tau_2)$ , representing the joint probability of finding a triple of values of  $y$  at times  $t$ ,  $t + \tau_1$ , and  $t + \tau_2$  in the intervals  $(y_k, y_k + \Delta y_k)$ ,  $(y_l, y_l + \Delta y_l)$ , and  $(y_m, y_m + \Delta y_m)$ , respectively. For a stationary random function of time this quantity likewise is independent of time. Extension to the fourth and higher probability densities is obvious.

Since the first and second probability densities provide most of the information useful in applications, nothing further will be said concerning those of higher order, other than to emphasize two facts: (a) for any stationary random function of time, the probability densities furnish complete quantitative information, and may therefore be considered as defining the function, and (b) from the probability density of any order, all those of lower order may be derived (see refs. 7 and 8); for example,

$$W_1(y_k) = \int_{-\infty}^{\infty} W_2(y_k, y_l, \tau) dy_l \quad (1)$$

Although the probability densities are the basic quantities defining a stationary random function of time and provide the foundation for the theoretical development of the subject, they are not extensively used in practice. Certain auxiliary variables derived from them are used instead. The more important of these are the mean value, the mean square, the autocorrelation function, and the spectral density. They are obtained from the probability densities by assuming that time averages are equal to the statistical averages furnished by the probability densities; namely,

$$\bar{y} \equiv \lim_{T \rightarrow \infty} \frac{1}{T} \int_0^T y(t) dt = \int_{-\infty}^{\infty} y W_1(y) dy \quad (2)$$

$$\overline{y(t)y(t+\tau)} \equiv \lim_{T \rightarrow \infty} \frac{1}{T} \int_0^T y(t)y(t+\tau) dt \quad (3a)$$

$$= \int_{-\infty}^{\infty} \int_{-\infty}^{\infty} y_k y_l W_2(y_k, y_l, \tau) dy_k dy_l \quad (3b)$$

A little reflection will show that these relationships are plausible; a more sophisticated line of reasoning, developed from fundamental considerations purposely avoided here, will be found in references 7 and 8.

Proceeding on this basis, one obtains immediately from the first probability density the mean values:

$$\bar{y}^0 = \int_{-\infty}^{\infty} W_1(y) dy = 1 \quad (4)$$

$$\bar{y} = \int_{-\infty}^{\infty} y W_1(y) dy \quad (5)$$

$$\overline{y^2} = \int_{-\infty}^{\infty} y^2 W_1(y) dy \quad (6)$$

$$\overline{y^n} = \int_{-\infty}^{\infty} y^n W_1(y) dy \quad (7)$$

Also, the autocorrelation function, defined as

$$R(\tau) \equiv \overline{y(t)y(t + \tau)} \quad (8)$$

comes directly from the second probability density by use of equations (3). Last of all, from the Wiener-Khintchine theorem, the spectral density is defined in terms of the autocorrelation function:

$$G(f) \equiv 4 \int_0^{\infty} R(\tau) \cos 2\pi f \tau d\tau \quad (9)$$

The significance of the autocorrelation function may be understood from consideration of the defining equation 3(a). If one imagines two curves  $y(t)$  and  $y(t + \tau_1)$  - the latter curve being derived from the former by shifting it  $\tau_1$  time units to the left - and computes the average value of the product of the two curves over a time  $T$ , which in the limit approaches infinity, one value,  $R(\tau_1)$ , will have been calculated for the autocorrelation function. Repetition of this procedure for other values of  $\tau$  determines the function. It is apparent that the result (i.e., the autocorrelation function) is independent of time, being dependent only on the time interval,  $\tau$ .

A further understanding of this function is provided by a comparison with the correlation coefficient,  $r$ , used in probability theory and defined by the following equation for any two variables  $x, z$ :

$$r \equiv \frac{\overline{xz}}{\sqrt{\overline{x^2}} \sqrt{\overline{z^2}}} \quad (10)$$

if

$$x = y(t)$$

$$z = y(t + \tau)$$

then

$$\begin{aligned}\overline{x^2} &= \overline{[y(t)]^2} = \overline{y^2} \\ \overline{z^2} &= \overline{[y(t + \tau)]^2} = \overline{[y(t)]^2} = \overline{y^2} \\ r &= \frac{\overline{y(t)y(t + \tau)}}{\overline{y^2}} \\ r &= \frac{1}{\overline{y^2}} R(\tau)\end{aligned}\quad (11)$$

It is thus apparent that, since  $\overline{y^2}$  is independent of time, the quantity  $\overline{y(t)y(t + \tau)}$  is a direct measure of the correlation coefficient  $r$  of the two variables  $y(t)$  and  $y(t + \tau)$ ; hence, the source of the term "correlation" in "autocorrelation function."

An interpretation of the spectral density can be derived from the defining equation (9), which, in effect, states it to be the cosine transformation of the autocorrelation function. Inasmuch as this latter function is even, the Fourier integral theorem may be used to establish the inverse relationship

$$R(\tau) = \int_0^{\infty} G(f) \cos 2\pi f \tau \, df \quad (12)$$

For  $\tau = 0$ , there is obtained

$$R(0) = \int_0^{\infty} G(f) \, df$$

and from the definition of  $R(\tau)$  (eq. (8))

$$R(0) = \overline{y(t)y(t)} = \overline{y^2}$$

hence

$$\int_0^{\infty} G(f) \, df = \overline{y^2} \quad (13)$$

and

$$\overline{y^2} = \lim_{\Delta f \rightarrow 0} [G(0)\Delta f + G(f_1)\Delta f + G(f_2)\Delta f + \dots]$$

~~CONFIDENTIAL~~

The spectral density therefore represents the spectrum (or frequency content) of the mean square value of the time-dependent variable,  $y$ . If one considers  $y$  to be composed of an infinite number of infinitesimally small, time-dependent sinusoidal waves, the frequencies of which are continuously distributed from zero to infinity (i.e., all frequencies are present), then the spectral density represents the relative magnitudes of the squares of the amplitudes of these infinitesimally small sinusoids. This interpretation closely parallels that of the Fourier transform of a transient function, which also decomposes a function of time into a frequency spectrum.<sup>1</sup>

The central importance of the spectral density lies in the fact that not only does it furnish valuable information in itself, but also most of the other useful quantities can be calculated from it. It has already been shown (eqs. (12) and (13)) how the autocorrelation function and mean-square value can be obtained from the spectral density. Another application, often used in the present investigation, is the relation between the spectral densities of the input and output of a linear filter<sup>2</sup> (see ref. 8):

$$G_o(f) = |Y(2\pi jf)|^2 G_i(f) \quad (14)$$

where  $Y(2\pi jf)$  is the complex frequency-response function of the filter defined and discussed in reference 8. During the course of the investigation it was experimentally observed that the airfoils behaved as linear mechanical filters. Since the impressed aerodynamic forces were stationary random functions of time, the experimental (or analog) solution of equation (14) afforded one means of measuring both the instantaneous normal force and the corresponding spectral density.

This variable also furnishes the mean-square value of  $dy/dt$ , or of any higher derivative:

---

<sup>1</sup>It is not surprising, therefore, to find that  $G(f)$  can be expressed in terms of the Fourier transform of  $y(t)$ . This approach is used in references 7 and 8.

<sup>2</sup>The term "linear filter" is used in the broad sense to designate any frequency sensitive device - electrical, mechanical, acoustical, etc. - the output of which is related to the input by a linear differential equation with constant coefficients. It consequently is a device which (a) responds to a sinusoidal input in such a fashion that the ratio of the amplitudes of output to input is a function only of the frequency (together with the physical constants of the filter), (b) has physical constants which are invariant with time, and (c) yields an output corresponding to the sum of any number of inputs which is equal to the sum of the outputs corresponding to each individual input (i.e., conforms to the principle of linear superposition).

---

$$\overline{\left(\frac{d^ny}{dt^n}\right)^2} = \int_0^\infty (2\pi f)^{2n} G_y(f) df \quad (15)$$

a relation which may be established with the aid of equation (14). Set

$$z(t) = \frac{d^ny}{dt^n}$$

Then  $\overline{z^2}$ , the quantity desired, is:

$$\begin{aligned} \overline{z^2} &= \int_0^\infty G_z(f) df \\ &= \int_0^\infty \frac{G_y(f)}{|Y(2\pi jf)|^2} df \\ Y(2\pi jf) &= \frac{1}{(j\omega)^n} \end{aligned}$$

$$\overline{\left(\frac{d^ny}{dt^n}\right)^2} = \int_0^\infty (2\pi f)^{2n} G_y(f) df \quad (15)$$

This brief sketch of the theory of a stationary random function of time may be summarized in the following manner. First, the basic variables from which the mathematical relationships are developed are the probability densities, a knowledge of which is both sufficient and necessary to define the function completely. Second, the principal tool required in this development is the hypothesis that time averages are equal to statistical averages. Third, the most useful quantities in practice are ordinarily not the probability densities, but the mean value, the mean square, the spectral density, the autocorrelation function, and others, all of which (except the mean value) can be computed directly from the spectral density. Fourth, for any linear filter there exists a simple relationship between the spectral density of the input and the output.

One additional observation should be made. If the first probability density is normally distributed, that is, is of the form

$$W_1(y) = \frac{1}{\sqrt{2\pi} \sqrt{y^2}} e^{-(y^2/2y^2)}$$

then a knowledge of it, together with the autocorrelation function, is sufficient to obtain the second and all higher probability densities, which also are normally distributed. The stationary random function of time is therefore defined completely. Furthermore, when such a signal is transmitted through a linear filter, the probability densities of the output signal likewise are normally distributed, and may consequently be calculated by use of the foregoing equations.

#### APPARATUS AND INSTRUMENTATION

##### Tunnel, Models, and Instrumentation for Steady Force Measurements

This investigation was conducted in the Ames 1- by 3-1/2-foot high-speed wind tunnel, which is a two-dimensional flow tunnel having a test section of the dimensions indicated. The two-dimensional airfoil models, of 6-inch and 12-inch chord, were constructed of solid aluminum alloy and mounted in the tunnel to span completely the 1-foot dimension of the test section (fig. 2). Contoured sponge-rubber gaskets were compressed between the model ends and the tunnel walls to prevent end leakage.

Static lift forces were measured by integrating the pressure reactions on the tunnel floor and ceiling, produced by the forces on the airfoil, in a manner similar to that described in reference 9. The pressure fluctuations at the orifices arising from unsteady lift forces were small and had no perceptible effect on the static values. Drag forces, used for Mach number corrections, were determined from wake survey measurements made with a rake of total head tubes. Angle of attack was measured to the nearest  $0.05^\circ$ .

##### Instrumentation for Unsteady Normal-Force Measurements

Two separate sets of instrumentation, each based upon a different principle, were developed to measure the instantaneous airfoil normal force. The first unit - the pressure-cell equipment - integrated the instantaneous pressure distribution around the profile. The second unit - the strain-gage equipment - measured the instantaneous normal-force reaction of the model itself. *How Calibrated*

Pressure-cell equipment. - The general arrangement and some of the details of the pressure-cell equipment are shown in figures 2 to 5. This equipment consisted of a group of capacitance-type pressure cells mounted in one wall of the tunnel adjacent to the model surface, as shown in figures 2 and 3. The output of the cells was combined electrically to

obtain an integrated signal proportional to the instantaneous normal force. Twenty-two pressure cells disposed in two lines of eleven cells each (fig. 3) were employed. Two different cell arrangements were utilized - straight line and curvilinear. The straight-line arrangement was better adapted to accommodate the variety of profiles tested, and consequently supplied the majority of the data reported.

A cross-sectional view of a pressure cell showing the main features and over-all dimensions is presented in figure 4. A complete description of the cell and some information concerning the methods of fabrication may be found in reference 10. As may be seen from the figure, the diaphragm forms one plate of a capacitor, and the spindle, the other. In operation, the diaphragm deflects under pressure, thus changing the capacitance by an amount proportional to the pressure imposed. The rear face of the diaphragm was vented to test-section static pressure for a known reference.

The cells were statically calibrated, after installation in test position, to  $\pm 0.1$  inch of water for a calibration range of  $\pm 60$  inches of water. Repetition of the calibration from time to time showed the cells to be very stable, no significant drift from any source, including temperature, being detected during the course of the investigation. The cell resonant frequency was high enough - approximately 25,000 cycles per second, or 20 times the highest aerodynamic component - to have no influence on the results. The sensitivity of each cell was kept within 5 percent of the average value of the group.

Power was supplied to the cells at 100 kilocycles per second and 50 volts (see fig. 5). This carrier wave was modulated by the change in cell capacitances caused by the variation of pressure on the diaphragms; after amplification it was demodulated, filtered to reject all frequencies above 3000 cycles per second, and measured with standard laboratory indicating instruments capacitor-coupled to reject the direct-current component. A highly damped, average-reading, vacuum-tube voltmeter indicated the average unsteady normal force, and a thermocouple meter indicated the root mean square.

*No. 1*  
 The side-wall location of the pressure cells for the measurement of unsteady normal forces has no precedent; it was chosen largely because of the mechanical difficulties inherent in any other arrangement. The results reported in reference 11, together with calculations based upon potential theory, however, suggested that approximately 90 percent of the static normal force would be measured. To verify this conclusion a comparison was made between the static normal force, measured by the pressure cells, and the static lift force, measured with the conventional wind-tunnel instrumentation, for a few models over the range of Mach numbers and angles of attack of interest. A typical result is summarized in figure 6 which shows several loci, on the Mach number and lift-coefficient plane, for

Please note:

~~CONFIDENTIAL~~  
 From ref 11. with 20 incidences at  $\alpha = 0^\circ$  and 20 at  $\alpha = 15^\circ$  used of a  $1\frac{1}{2}$  thick airfoil. The curves at  $\alpha = 6^\circ = .45$  .53 7  
 at  $\alpha = 15^\circ$  .57 .80

which the ratio of static normal force to static lift force is constant. Using this figure, it is possible to estimate immediately, for any combination of Mach number and lift coefficient, the proportion of normal force measured by the pressure cells. The area in which unsteady normal-force coefficient exceeds 0.005, the smallest magnitude reported in the ensuing results, is also shown. Comparison of this region with the loci demonstrates that, in the region of unsteady normal forces, the expectation of measuring 90 percent of the static normal force was approximately fulfilled.

A direct parallel cannot, of course, be drawn between results obtained for steady and unsteady normal force. The influence of the tunnel-wall boundary layer and the measurement of pressures in a nonisotropic turbulent-flow stream perpendicular to the direction of the desired component would be expected to exert a greater influence upon the unsteady results than on the steady ones. The realization of these difficulties, in fact, and the desire to appraise these and other effects was one of the major factors motivating the development of an alternative method of measurement. For reasons discussed further on, however, the pressure-cell arrangement was considered adequate for investigation of unsteady normal-force trends with airfoil geometry.

Strain-gage equipment.- The measurement of unsteady normal force with the strain-gage equipment, in essence, consisted of measuring the instantaneous vertical deflection of the airfoil at midspan by use of a strain gage, and of computing the imposed force causing this displacement from the differential equation describing the motion. To perform the required computations readily, an analog computer (termed a "resonance compensating amplifier"), operating directly on the strain-gage signal and providing the unsteady normal force continuously during testing, was developed. The root-mean-square value of the output of the resonance compensating amplifier was measured with a thermocouple meter.

The theory underlying the strain-gage technique, schematically illustrated in figure 7, is dependent upon the experimentally established fact that the airfoil models, when subjected to unsteady aerodynamic forces, behave very nearly as simply supported beams vibrating in the fundamental mode. The differential equation descriptive of this system (derived in ref. 12) is:

$$N_I = k\delta + \gamma \frac{d\delta}{dt} + m \frac{d^2\delta}{dt^2} \tag{16}$$

This equation is more suitable for the present investigation if the dependent variable  $\delta$  is replaced by an equivalent normal force. Define

$$N_0 = k\delta \tag{17}$$

$\gamma/c$	Cm at $\alpha = 7$	
surface	.57	.50
.1	.45	.54
.15	.41	.52
.20	.38	.48

$$\delta = \frac{1}{k} N_0 \quad (18)$$

Substituting equation (18) in equation (16):

$$N_1 = N_0 + \frac{\gamma}{k} \frac{dN_0}{dt} + \frac{m}{k} \frac{d^2N_0}{dt^2}$$

$$\frac{k}{m} = \omega_n^2$$

$$\frac{\gamma}{k} = \frac{2}{\omega_n} \frac{\gamma}{\gamma_c}$$

$$N_1 = N_0 + \frac{2}{\omega_n} \frac{\gamma}{\gamma_c} \frac{dN_0}{dt} + \frac{1}{\omega_n^2} \frac{d^2N_0}{dt^2} \quad (19)$$

Where  $N_0$ , according to the defining equation (17), is the static normal force required to produce the displacement  $\delta$ . The quantity  $N_0$  may therefore be taken as the output normal force corresponding to the input normal force  $N_1$  for the system described by equation (16). Since equation (16) is a linear differential equation with constant coefficients, the airfoil may be regarded as a linear mechanical filter, having input  $N_1$  and output  $N_0$ . Accordingly, by application of equation (14),

$$G_{N_0}(f) = |Y_A(j\omega)|^2 G_{N_1}(f) \quad (20)$$

If the amplitude of the frequency-response function of the resonance compensating amplifier,  $|Y_R(j\omega)|$ , is the reciprocal of the amplitude of the frequency-response function of the airfoil,  $|Y_A(j\omega)|$ , that is, if

$$|Y_R(j\omega)| = \frac{1}{|Y_A(j\omega)|} \quad (21)$$

the mean-square value of the output of the resonance compensating amplifier will be directly proportional to the mean-square value of the input normal force. From equation (13):

$$\overline{[e_R(t)]^2} = \overline{e_R^2} = \int_0^{\infty} G_R(f) df$$

$$G_R(f) = |Y_R(j\omega)|^2 G_S(f)$$

$$|Y_R(j\omega)| = \frac{1}{|Y_A(j\omega)|}$$

$$G_S(f) = K_1^2 G_A(f)$$

$$G_R(f) = K_1^2 \frac{G_A(f)}{|Y_A(j\omega)|^2}$$

$$G_A(f) = |Y_A(j\omega)|^2 G_{N_1}(f)$$

$$\overline{e_R^2} = K_1^2 \int_0^\infty G_{N_1}(f) df$$

$$= K_1^2 \overline{N_1^2}$$

This derivation assumes nothing about the effect of the resonance compensating amplifier on the phase relationships of the input and output signal. Consequently, if mean-square values are the only results required, it is not necessary to preserve phases, although the resonance compensating amplifier does so.

The amplitude of the frequency response function of the amplifier, obtained directly from the differential equation (19) by taking the Fourier transform of both sides, is

$$|Y_R(j\omega)| = \frac{1}{|Y_A(j\omega)|}$$

$$= \left| 1 + \frac{2}{\omega_n} \frac{\gamma}{\gamma_c} j\omega + \frac{1}{\omega_n^2} (j\omega)^2 \right|$$

$$= \sqrt{\left( 1 - \frac{\omega^2}{\omega_n^2} \right)^2 + 4 \left( \frac{\omega}{\omega_n} \right)^2 \left( \frac{\gamma}{\gamma_c} \right)^2} \quad (22)$$

The strain-gage bridge used to measure airfoil deflection consisted of four active legs, connected to minimize thermal effects, and mounted as indicated in figure 2 in shallow pockets machined in the airfoil surface.

The bridge was located at the chordwise position of maximum thickness at the midspan station, and the individual gages were oriented to maximize the signal resulting from lateral bending in the first mode.

The resonance compensating amplifier performed the computations indicated by the right-hand side of equation (19). It consisted of an amplifier followed by 2 units, each composed of a differentiating circuit plus an amplifier. The outputs of the first amplifier and the two following units, after passing through attenuators, were combined in a summing circuit, the output of which represented the instantaneous unsteady normal force. The attenuators were used to adjust the coefficients of the time dependent terms on the right-hand side of equation (19) to their proper relative magnitudes. A filter in the circuit ahead of the resonance compensating amplifier limited the band width of the strain-gage signal to frequencies between 10 and 600 cycles per second, a range determined adequate by inspection of typical unsteady-normal-force spectral-density curves. The mean-square value of the unsteady normal force was indicated by the thermocouple meter.

Three series of tests were made to determine the extent to which the airfoil obeyed the relationship (19), that is, constituted a linear mechanical filter: (a) dead-weight calibrations to determine linearity of deflection and of strain-gage output with load, (b) impact loading to measure linearity of velocity damping and conformance of  $N_0$  with the transient solution of equation (19), and (c) comparison of the calculated value of resonant frequency with that measured during free vibration, and with the resonant frequency existing during tunnel operation.

From the first group of tests it was determined that the strain gage versus load curve was linear within 1 percent and that the deflection was directly proportional to the load to the nearest 0.0001 inch, the limit of resolution of the measuring instrument.

The proportionality constant of velocity damping was more variable, in the worst case departing as much as 10 percent from the selected value, a result of nonlinear effects inherent in the complete system. However, since the contribution to the total unsteady force arising from the damping was less than 5 percent, this relatively large percentage error influenced the net result to a very small degree. Examination of the recorded oscilloscope traces of the transient motion and comparison with the exponentially damped sine wave calculated from equation (19) showed satisfactory agreement in all other respects.

The resonance compensating amplifier was tested by comparing observed values of gain at various frequencies with the corresponding quantities calculated from equation (22). As may be seen from figure 8, the agreement was excellent throughout the frequency range of interest.

Another test also was made. Calculated values of the spectral density of unsteady normal force (obtained by applying eqs. (20) and (22) to the spectral density of the strain-gage signal) were compared with corresponding values measured with the resonance compensating amplifier for airfoils at various combinations of Mach number and angle of attack. Results of one such experiment are shown in figure 9. While the agreement is not so good as was achieved by the direct comparison of the preceding test, it is considered satisfactory. Most of the discrepancy is thought to result from the inability to maintain wind-tunnel conditions completely constant for the period required to record the data.

Auxiliary instruments.- Certain auxiliary instruments were employed in conjunction with the measurement of unsteady normal forces. An assembly consisting of a narrow band pass (4.64 cps) wave analyzer, which automatically swept through the frequency range at a slow rate, and which drove a recording potentiometer, was used to obtain the continuous spectra from which spectral densities were computed. In addition, a pair of capacitance-type pressure cells - identical to those already described - was installed in the floor and ceiling of the wind tunnel as shown in figure 2. The signal from these cells was monitored to determine the onset of wind-tunnel resonance.

## TESTS

### Test Variables

Twenty-seven profiles, listed in table I, were selected to provide a variation of maximum thickness from 4- to 12-percent chord, of camber from 0 to 0.6 design lift coefficient, of position of minimum pressure from 30- to 60-percent chord, and of leading edge radius from 0- to 1.5-percent chord. These profiles were tested through the Mach number range between 0.5 and 0.9 and at lift coefficients generally extending from zero to maximum. Maximum lift, however, was not obtained at the highest Mach numbers because of choked flow. The Reynolds numbers of the tests are plotted as a function of Mach number for 6-inch-chord models in figure 10. In addition, Reynolds number was varied in two cases by doubling the chord of the model.

### Test Procedure

Comparative results for the two different methods of measuring unsteady normal force indicated that, although results obtained with the strain-gage instrumentation were considered the more reliable, data obtained with the pressure cells would be suitable for studying trends with

geometry. Inasmuch as the latter arrangement was better suited for testing large numbers of profiles, it was adopted, and strain-gage measurements were made for a few airfoil sections for comparison. An account of these comparative measurements may be found in Appendix A.

At each test point the signal from the floor and ceiling cells was recorded to indicate the effect of tunnel resonance. A subsidiary investigation conducted to appraise these results demonstrated that, while resonance existed, its effects were small and could be ignored. The details of this work are recounted in Appendix B, in which also is discussed the influence of airfoil resonance. This latter phenomenon likewise was decided to be of no importance.

The procedure for using the pressure-cell equipment was straightforward as, for the most part, was that entailed in the use of the strain-gage equipment. For the latter instrumentation, however, it was necessary to adjust the resonance compensating amplifier properly to account for the inertial, damping, and spring forces of each airfoil model. The method for doing so was established by noting from equation (19) that the adjustment depended only upon the airfoil resonant frequency  $\omega_n$ , and the damping ratio  $\gamma/\gamma_c$ . Both of these quantities were measured with the tunnel operating at the test conditions for which the aerodynamic data were obtained. The resonant amplitude was sufficiently pronounced to permit direct reading of the frequency from the uncompensated strain-gage signal. The damping ratio was computed from the frequency spectrum of the uncompensated strain-gage signal; its determination was dependent upon the fact that at resonant frequency, for the low damping ratios (0.02 to 0.04) invariably present, the ratio of the amplitudes of the compensated and uncompensated strain-gage signal is practically equal to  $2\gamma/\gamma_c$ . The latter amplitude was read directly from the frequency spectrum; that for the former was obtained by fairing a curve for the estimated value of the compensated strain-gage signal through the point of resonant frequency. It further turned out in practice that the damping ratios were so low that the corresponding adjustment was not at all critical. For this reason, after experience had demonstrated that 0.04 damping ratio was not likely to be exceeded, this value was used throughout the investigation.

#### Reduction of Data

Root-mean-square values of the unsteady normal-force coefficients were obtained by two different methods. Most of the pressure-cell results were calculated from the average values indicated by the vacuum-tube voltmeter, using the theoretical ratio  $\sqrt{\pi/2} = 1.253$ , of root mean square to average for a normally distributed probability density. Experimental data confirming the use of this ratio are presented during discussion of the statistical aspects of the data in the Results and Discussion section. The strain-gage results, on the other hand, as well as all comparative

pressure-cell data, were observed directly with a thermocouple meter, which provided correct root-mean-square values for all signals.

Some corrections were applied to the observed data. The lift coefficients and the free-stream Mach number were corrected for tunnel-wall effects by the methods of reference 13. Unsteady normal-force coefficients at all Mach numbers were corrected to remove the small amounts (tare values) of unsteady force invariably present at Mach numbers below 0.5 and lift coefficients near 0. These tares are thought to result from the turbulence inherent in the wind-tunnel air stream, as well as from that present in the tunnel-wall boundary layer. The procedures for making the corrections are described in Appendix C.

Spectral densities were computed from the wave analyzer results with the aid of the equation:

$$G_{N_1}(f_1) \approx \frac{[\overline{E_W(f_1)}]^2}{K_1^2 K_2^2 \int_{-f_0}^{+f_0} |Y_W(2\pi j\phi)|^2 d\phi} \quad (23)$$

where  $Y_W(2\pi j\phi)$  is the frequency-response function of the wave analyzer, and  $2f_0$  is the band pass width of the analyzer. The numerical value of

$$\int_{-f_0}^{+f_0} |Y_W(2\pi j\phi)|^2 d\phi \quad (4.64 \text{ cps})$$

was obtained by mechanical integration

of an experimental curve. Unless otherwise noted, the spectral-density plots of unsteady normal-force coefficients were calculated from the spectral densities of the output force,  $N_0$ , by use of this equation, together with equations (15) and (22). Correct fairing of the curves between points was determined from inspection of the continuously recorded frequency data.

The relationship (23) was derived in the following manner (see fig. 7). For any particular frequency setting,  $f_1$ , of the wave analyzer,

$$[\overline{E_W(f_1)}]^2 = \int_{-f_0}^{+f_0} G_W(f_1 + \phi) d\phi$$

where  $\phi$  is the frequency dependent variable of the output spectra.

$$G_W(f_1 + \phi) = |Y_W[2\pi j(f_1 + \phi)]|^2 K_2^2 G_R(f_1 + \phi)$$

$$\overline{[E_W(f_1)]^2} = K_2^2 \int_{-f_0}^{+f_0} |Y_W[2\pi j(f_1 + \varphi)]|^2 G_R(f_1 + \varphi) d\varphi \quad (24)$$

It is a characteristic of the wave analyzer employed that  $|Y_W[2\pi j(f_1 + \varphi)]|$  is the same for all frequency settings, therefore

$$|Y_W[2\pi j(f_1 + \varphi)]| = |Y_W(2\pi j\varphi)|$$

Also within the small range  $-f_0 < f < f_0$  (approximately 10 cps wide)

$$G_R(f_1 + \varphi) \approx G_R(f_1)$$

and

$$\begin{aligned} G_R(f_1) &= |Y_R(j\omega)|^2 K_1^2 |Y_A(j\omega)|^2 G_{N_1}(f_1) \\ &= K_1^2 G_{N_1}(f_1) \end{aligned}$$

Substitution of these relationships into (24) yields

$$\overline{[E_W(f_1)]^2} \approx K_1^2 K_2^2 G_{N_1}(f_1) \int_{-f_0}^{+f_0} |Y_W(2\pi j\varphi)|^2 d\varphi$$

thus

$$G_{N_1}(f_1) \approx \frac{\overline{[E_W(f_1)]^2}}{K_1^2 K_2^2 \int_{-f_0}^{+f_0} |Y_W(2\pi j\varphi)|^2 d\varphi} \quad (23)$$

which is the equation desired.

## RESULTS AND DISCUSSION

The principal results obtained in this investigation consist of (a) an appraisal of the effect of geometric parameters on the unsteady normal-force characteristics of airfoil sections over the Mach number range of 0.75 to 0.9 for lift coefficients of 0 to 0.6, (b) comparison of wind-tunnel results with flight measurements, (c) evaluation of the effect of

Reynolds number on the unsteady force measurements, (d) measurements of quantities describing unsteady normal force as a stationary random function of time, and (e) a suggested method for applying unsteady force data to the problem of airplane buffeting. Each of these topics is discussed in turn.

#### Effect of Airfoil Geometric Parameters

The effect of airfoil geometry was examined by comparing the unsteady normal-force characteristics of 23 profiles (see table I) having a variation in maximum thickness from 4- to 12-percent chord, in camber from 0 to 0.6 design lift coefficient, in position of minimum pressure from 30- to 60-percent chord, and in leading-edge radius from 0- to 1.5-percent chord. Lift coefficient versus angle of attack, unsteady normal-force coefficient as a function of lift coefficient, and contour plots of constant magnitudes of unsteady normal-force coefficient on the lift-coefficient and Mach number plane are shown in figures 11 to 34 for each of these profiles. The (a) and (b) parts of each figure contain the basic data from which part (c) is derived. The dashed lines appearing on some of the contour plots indicate portions of the curves obtained by extrapolating the  $\Delta c_{n_{rms}}$  vs.  $c_l$  curves, such extrapolations being resorted to only when supported beyond reasonable doubt by the trend of adjacent data. No symbols appear on parts (a) and (b) of figures 16, 17, and 19 to 22 because these figures were derived from cross plots of measurements at constant angle of attack (instead of constant Mach number). Results shown in figures 19 to 22 were obtained from the curvilinear cell installation (fig. 3); as shown in Appendix A they are not directly comparable with those measured with the straight-line-cell installation.

Inspection of the  $\Delta c_{n_{rms}}$  vs.  $c_l$  curves for these airfoil sections (part (b) of figs. 11 to 34) discloses that certain features are often present. At low Mach numbers the very sharp rise of  $\Delta c_{n_{rms}}$  from initially small values with little, or in some cases no, increase in lift coefficient is most noticeable. Reference to part (a) reveals that these sharp increases occur in the vicinity of maximum lift. For the higher Mach numbers, above 0.8 approximately, sizable amounts of unsteady normal force are present even at low lift coefficients.

From an examination of the contours of part (c) of the figures it is clear that, although the contour values are in geometric progression, the curves generally become more closely spaced as the region of unsteady normal force is progressively entered. The corresponding maximum unsteady normal-force gradient therefore rises sharply.

Data from the contour plots of these figures were cross-plotted to show the variation of unsteady normal force with thickness in figure 35,

with camber in figure 36, with position of minimum pressure in figure 37, and with leading-edge radius in figure 38. As will be noted from these figures, the data pertain primarily to lift coefficients between 0 and 0.6, and Mach numbers from 0.75 to 0.89. This lift-coefficient range is selected because of the limitations imposed by low Reynolds number, discussed further on.

Of these four parameters, thickness is shown to have the greatest influence. For the symmetrical NACA 65-series sections (fig. 35(a)), a reduction of thickness from 12 to 8 percent is accompanied at all lift coefficients by a marked decrease in unsteady normal force. With further reductions of thickness below 8 percent, however, this trend disappears and, for some combinations of lift coefficient and Mach number (e.g.,  $c_l = 0.4$ ,  $M = 0.85$  and  $c_l = 0.6$ ,  $M = 0.775$ ), even reverses itself, the unsteady normal force becoming larger as the thickness decreases. This reversal, however, is not universally present, as indicated by inspection of the comparative plots of  $\Delta c_{n,rms}$  vs.  $c_l$  presented in figure 39 for the NACA 65-series sections. Notice particularly that for Mach numbers 0.785, 0.809, and 0.832, above 0.6 lift coefficient, the 4- and 6-percent-thick sections show distinctly smaller values of unsteady normal-force coefficient than do those of 8-, 10-, and 12-percent thickness. These observations are generally substantiated by the results of references 3 and 5, although the pressure pulsations discussed in the former reference give little indication of increased unsteady normal-force coefficients with decreased thickness below 8 percent.

The results for the NACA 2-series airfoil sections for lift coefficients of 0.6 and below (fig. 35(b)) are by no means so clear cut, reductions of thickness below 8 percent sometimes being accompanied by increased unsteady normal force ( $c_l = 0.2$ ,  $M = 0.890$  and  $c_l = 0.4$ ,  $M = 0.890$ ), and sometimes, notably for  $c_l = 0.6$ , by a decrease. The trends however, except at  $c_l = 0.6$ , are not pronounced, and the conclusion that little is gained by reducing thickness below 8 percent appears valid for this family of profiles also.

There are few unqualified statements which can be made concerning the effects of camber, summarized in figure 36. The most interesting result is the decrease in unsteady normal force of the 12-percent-thick, NACA 65-series section accompanying an increase of camber from 0.4 to 0.6 design lift coefficient, which takes place at Mach numbers even as high as 0.875. Amounts of camber less than 0.4, however, in general have but little effect on unsteady normal-force magnitudes, not only for these sections but for the corresponding 4-percent-thick sections (fig. 36(b)) as well.

The trends of unsteady normal force with chordwise location of the position of minimum pressure for the 10-percent-thick, symmetrical, NACA 6-series airfoil sections (fig. 37) are considered relatively unimportant. At the higher lift coefficients (0.4 and 0.6), however, it is possible to

conclude that the most rearward position of minimum pressure investigated, 60-percent chord, is slightly unfavorable.

Results appraising the effect of leading-edge radius are summarized in figure 38. Inspection of this figure shows that, in general, although there is a slight trend in the direction of increased unsteady normal-force coefficient with increasing leading-edge radius, the tendency is not sufficiently pronounced to be conclusive. The weight of the evidence does indicate, however, that an abnormally large leading-edge radius is not favorable. This conclusion is supported by comparison of the results, previously presented in figure 35(a), for the NACA 65-series airfoil sections with those for the more bulbous nosed 2-series sections, figure 35(b). At comparable values of lift coefficient, Mach number, and thickness, the latter sections display a generally greater value of  $\Delta c_{n_{rms}}$  than do the former.

In summary it is seen that maximum thickness, of the four geometric parameters investigated, has the greatest effect upon unsteady normal-force characteristics at high subsonic Mach numbers and lift coefficients up to 0.6. The influence even of this parameter, however, is noticeably diminished for thicknesses below 8 percent for the profiles investigated, being pronounced only at lift coefficients above 0.6 and for just the small Mach number range extending from 0.76 to 0.86. For the 12-percent-thick NACA 65-series, camber above 0.4 design lift coefficient also affects unsteady normal force to a significant degree, showing beneficial results up to as high as 0.875 Mach number. Trends with leading-edge radius for radii below 1.2-percent chord, with camber for 4-percent-thick NACA 65-series profiles, and with position of minimum pressure for the NACA 6-series, 10-percent-thick, symmetrical profiles are relatively unimportant. Abnormally large leading-edge radii appear to be disadvantageous at high subsonic Mach numbers.

#### Comparison With Airplane Buffeting

The buffet boundaries reported in reference 14 for four straight-wing airplanes, aspect ratios 4.17, 5.17, 6.00, and 6.39, are compared in figure 40 with the unsteady normal-force coefficient contours measured for the corresponding airfoil sections at the wing-fuselage juncture. Buffet boundaries are used instead of contours because the boundaries mark the beginning of structural vibration and, by the same token, the first appearance of the aerodynamic force causing buffeting. There should therefore be some correspondence between the boundary and the 0.005 unsteady normal-force coefficient contour since this quantity, which is the smallest that could be reliably measured, also marks the first appearance of the disturbing force in the wind tunnel. This comparison, of course, fails to recognize differences due to Reynolds number. From inspection of this figure it is concluded that, while discrepancies exist (chiefly in the region

of high lift coefficients and moderate Mach numbers, as would be expected), the agreement is good enough to infer that the wind-tunnel measurements of unsteady normal force on the profile are directly related to the buffeting found in flight.

It is interesting to note the extremely sharp gradient of unsteady normal force across the contours displayed by the NACA 23018 airfoil section (fig. 40(a)), which, as will be seen later, also exists for the 23013 section. No other profile investigated shows such an abrupt rise of intensity, and the fact that the airplane equipped with this profile is known to have particularly violent buffeting characteristics may be taken as further evidence supporting the wind-tunnel results.

#### Effect of Reynolds Number

To gain some insight concerning the effect of Reynolds number on unsteady normal force, 12-inch-chord models of the NACA 23013 and of the 65-213,  $a = 0.5$  airfoil sections were tested up to the tunnel choking Mach number (0.7 approximately). The results are compared with 6-inch-chord airfoil data, figures 41 and 42, both the 6-inch- and 12-inch-chord data being obtained with the strain-gage instrumentation. Shown also in figure 42 is the same buffet boundary plotted in figure 40(b) for the airplane having the NACA 65-213,  $a = 0.5$  wing section. Although these data are scanty, they do indicate that increasing the Reynolds number from approximately 2 million to approximately 4 million significantly alters the unsteady normal-force characteristics. Comparisons, moreover, of 6-inch-chord data with flight data, and of 6-inch-chord data with 12-inch-chord data, show discrepancies that are in the same direction and of comparable magnitude, a result which further indicates that the Reynolds numbers of 1 to 2 million are undesirably low.

It will be observed that increased Reynolds numbers generally result in shifting the unsteady normal-force coefficient contours in the direction of increased lift coefficient (figs. 41 and 42). A possible explanation for this shift is the higher lift coefficients realized at higher Reynolds numbers at the same angle of attack. To investigate this possibility comparative plots of unsteady normal-force coefficient versus angle of attack were examined. It was found that practically all of the differences for the NACA 23013 airfoil section could thus be explained, but that practically none for the 65-213,  $a = 0.5$  section could be. Apparently, therefore, while the differences for this latter airfoil are connected in some way with the higher lift coefficients obtained at higher Reynolds numbers, the relationship is not direct and the available data are not sufficient to isolate the ultimate cause.

Some additional information concerning this matter is to be found from comparison of the spectral densities of figure 43. The upper half

of this figure presents the data, both ordinate and abscissa, in absolute units; in the lower half the ordinate is normalized with respect to  $(\Delta c_n')^2$  (i.e., the area under the curve) and the abscissa, with respect to reduced frequency, or Strouhal number. The agreement of the normalized plots is certainly good enough to provide hope that extrapolation to larger scales may be accomplished on the basis of Strouhal number; however, it cannot be emphasized too strongly that the supporting evidence for doing so is very meager.

Tests were also made to see if the effective Reynolds number could be increased artificially with a turbulent boundary layer, obtained in the usual way by roughening the leading edge of the airfoil surface. No change in unsteady normal-force characteristics was observed. Assurance that the entire boundary layer up to the point of separation was turbulent was provided by liquid film tests, coupled with schlieren observations of the shock-wave pattern. The same technique disclosed that without roughness the flow remained laminar to the point of separation.

#### Statistical Aspects of the Data

A principal result of this investigation is the conclusion that the unsteady normal force on a two-dimensional airfoil is a stationary random function of time, and can be defined by measurement of the chief variables pertaining to this type of function.

Stationary character of the unsteady normal force.- A stationary random function of time is, by definition, one for which all the probability densities are invariant with time. Although the evidence available is insufficient to demonstrate conclusively that the densities are invariant, it is enough to allay reasonable doubts.

Equations (5) and (6) express the mean value and the mean-square value of a random function in terms of the first probability density. It is an experimentally observed fact that both of these quantities are time-invariant. Accordingly, although it is still mathematically possible for the first probability density,  $W_1(y)$ , to be a function of time, the contingency is remote. More direct evidence is furnished by the probability-density measurements described below.

A similar line of reasoning may be applied to the second probability density, which in equation (3b) is used to define the autocorrelation function and, indirectly, via equation (9), the spectral density. The repeatability of this latter function under test conditions is well illustrated in figure 44, in which two spectra observed at widely different times are compared. The agreement is very good, and leaves little doubt that the spectral density and, hence, the autocorrelation function are

both time-invariant. It therefore seems quite probable that the second probability density is time-invariant.

No evidence was obtained concerning the nature of the third and higher probability densities. These quantities, however, do not enter into any aspect of this investigation and their characteristics are not of direct interest.

Form of the first probability density.- The first probability density was directly measured for a typical case by constructing a histogram of the unsteady normal-force coefficient from a high-speed film record of an oscilloscope trace. The result, based on 10,013 points abstracted from a 1.70-second film record, is shown in figure 45, fitted to a normal probability curve. The apparent good agreement is substantiated by the more objective measures commonly employed, that is, skewness (3rd moment), and kurtosis (4th moment) which are itemized in the upper left-hand corner of the figure. The agreement is extraordinary and, if this one case is representative, demonstrates conclusively that the first probability density is normally distributed. The spectral density corresponding to this histogram appears in figure 47(c).

An indication of the extent to which the results of figure 45 are representative is provided by comparing the ratio of the mean of the absolute value of section unsteady normal-force coefficient (i.e., the mean value of the fully rectified unsteady normal-force signal) to the root-mean-square value. For a normally distributed probability density this ratio is  $\sqrt{\pi/2} = 1.253$ . A summary of 887 simultaneous comparisons for nine airfoils is presented in the histogram of figure 46, which typifies histograms for each of the airfoils individually. The mean values were experimentally obtained with an average reading meter, and the mean-square values with a thermocouple meter, as previously described. As the figure shows, the ratios are heavily concentrated in the neighborhood of the 1.253 value, the small displacement of the median from 1.253 being within the accuracy of calibration. This result strongly suggests that the unsteady normal force of the 10,013-point distribution is typical, and that the first probability densities of the unsteady normal force of the airfoil sections are, in general, normally distributed.

The implication of this result has many ramifications, not the least of which is the conclusion pointed out in the discussion of the theory of stationary random functions of time, that, if the spectral density (or the autocorrelation function) is known, the function is completely defined; that is to say, all of the probability densities are determinable. The spectral density therefore furnishes virtually complete information concerning the unsteady normal-force characteristics of an airfoil section. This result also is the reason for reporting values of  $\Delta c_{n,rms}$  calculated from the mean-value readings with the 1.253 ratio, as previously described.

The data of figure 45 were also examined to see if the first probability density were stationary. This was done by subdividing the original record into ten parts, and comparing the defining parameters of the corresponding histograms with each other and with those of the original. No significant deviations or trends were found, a result which shows directly that the first probability density of this portion of the data is stationary.

Spectral densities of unsteady normal-force coefficient.- Several spectral densities of the unsteady normal-force coefficient, calculated from the strain-gage spectrum as previously described, are shown in figure 47 at the Mach number and lift coefficient loci noted on the accompanying contour plots,<sup>3</sup> which are based on strain-gage data. Included with each curve is the unsteady normal-force coefficient measured by integrating the area under the curve. When available, the corresponding value measured with the resonance compensating amplifier and thermocouple meter is shown for comparison. The resonant frequencies of the airfoil,  $f_A$ , and of the wind tunnel,  $f_T$ , are also shown.

Inspection of the 16 spectral densities contained in the figure indicates that the majority of the curves have the common characteristics of peaking in the low-frequency range, below 200 cycles per second, and dropping to a low value above this range. The exceptions to this generalization (NACA 23013 airfoil at  $M = 0.707$  and  $0.760$ , and the 65-213,  $\alpha = 0.5$ , airfoil at  $M = 0.705$ ) display spectrums having many random peaks of roughly equal amplitude, rather than a single, prominent spike. None of the 16 spectra can be adequately represented by the "white noise" spectrum sometimes assumed for calculations.

It is to be observed that the three spectral densities having multiple peaks differ from the others in that they correspond both to high Mach numbers and large unsteady normal-force coefficients. For this reason it may tentatively be suggested that spectrums at high Mach numbers and high unsteady normal-force coefficients are of a different nature from those at low Mach numbers or at small unsteady normal-force coefficients. Under the last named circumstances, unsteady normal force as a function of time approaches a harmonic variation much more closely than it does for the former.

The precipitous drop sometimes observed in the vicinity of the tunnel resonant frequency (NACA 65-110 airfoil at  $M = 0.655$ ,  $\alpha_0 = 8.27^\circ$ , and at  $M = 0.704$ ; 23013 airfoil at  $M = 0.563$ , and  $0.608$ , etc.) is considered to be a combination of aerodynamic characteristics and a tunnel

<sup>3</sup>The disagreement between the value of  $\left[ \int G_{\Delta C_n}(f) df \right]^{1/2}$  tabulated on the spectral-density curve of figure 47(a) for 0.603 Mach number and the corresponding value indicated by the contour plot results from measuring the spectral density at an angle of attack above that of maximum lift.

~~CONFIDENTIAL~~

resonance phenomenon discussed in Appendix B, the conjecture being that in the absence of tunnel resonance (or in the event of its occurring at a higher frequency) the decrease would be more gradual, resembling that for the NACA 65-213,  $a = 0.5$  profile at 0.555 Mach number, for example.

A cursory inspection is sufficient to demonstrate that the airfoil resonant frequency,  $f_A$ , is irrelevant to the results.

Tabulated below is a comparison (cf. eq. (13)) of the unsteady normal-force coefficients obtained by integration of the area under the spectral density curves with those measured with the thermocouple meter in conjunction with the resonance compensating amplifier:

NACA profile	Chord, in.	$\alpha_0$ , deg	M	Thermocouple meter, $[\overline{(\Delta c_n)^2}]^{1/2}$	Integration of spectral density, $[\int G_{\Delta c_n}(f) df]^{1/2}$
23013	6	6	0.707	0.0355	0.0369
23013	6	6	.707	.0355	.0379
23013	6	10	.655	.0416	.0422
23013	6	10	.655	.0400	.0433
23013	12	4.7	.711	.0280	.0307
23013	12	10.7	.556	.0450	.0476
65-213, $a = 0.5$	6	8	.705	.0317	.0310
65-213, $a = 0.5$	12	10	.557	.0368	.0351
65-110	6	6	.655	.0160	.0158
65-110	6	8.27	.655	.0495	.0505
0006-64	6	8.5	.556	.0465	.0454

Similar comparisons for six additional observations are also shown in figure 47.

Inspection of these data shows that, for unsteady normal-force coefficients greater than 0.02, discrepancies between corresponding values in the last two columns are generally of the order of 5 percent. This agreement, obtained for 17 observations at greatly different times, and over a wide range of geometric and aerodynamic variables, provides very persuasive evidence of the accuracy not only of the root-mean-square unsteady normal-force measurements made with the resonance compensating amplifier, but of the spectral densities as well.

It would be an omission to end the discussion of the spectral densities without pointing out some important limitations to these data. First, because of the rapidity with which the wind tunnel overheated above 0.75 Mach number, it was impractical to obtain spectral densities above this speed. Second, as has already been mentioned, the Reynolds number available at the lower Mach numbers is too small to provide representative maximum lift data. Third, 6 of the 16 spectral densities pertain to the

~~CONFIDENTIAL~~

NACA 23013 profile, and there is reason to suspect that the characteristics of this section are not representative. The steep gradient across the contours typifying this profile has already been mentioned. In addition, figure 47(b) shows a tendency for large amounts of unsteady normal force to exist close to zero frequency and above 200 cycles per second. The entire picture concerning spectral densities therefore is suggestive rather than definitive, and much work remains to be done before well founded conclusions can be drawn.

#### Application to Aircraft Buffeting

A principal objective in the investigation of unsteady normal-force phenomena is to derive the means and obtain the data which will enable the designer to predict from wind-tunnel data for airfoil sections the buffeting of an airplane. To do this it is necessary:

1. To select the significant quantities which describe both the aircraft buffeting and the unsteady aerodynamic forces causing buffeting.
2. To measure these quantities for the unsteady forces in the wind tunnel.
3. To establish the relationship between these quantities for the wind-tunnel aerodynamic forces and the aircraft buffeting.

The theory of stationary random functions of time points out the significant quantities to be used. Measurements at low Reynolds numbers made of these quantities for a selected group of profiles have been described and discussed in preceding portions of this report. There remains the problem of establishing the relationship between unsteady normal forces and buffeting.

The solution of this problem requires the development of a means for accounting for both the filtering effect of the aircraft structure and the spanwise variation of the unsteady lift. Both of these difficulties were encountered in the development of the strain-gage technique; the procedure in fact represents a practical solution, under wind-tunnel conditions, of the inverse problem - given the buffeting of a two-dimensional airfoil, to determine the corresponding aerodynamic forces. For this reason, the methods applied to the wind-tunnel case, or similar methods also derived from the theory of stationary random processes, seem to offer considerable promise in the analysis of aircraft buffeting. This same suggestion is made in reference 15, where a theory based essentially on what corresponds to equations (15) and (19) of the present report is developed in some detail.

~~CONFIDENTIAL~~

The conclusion that the wind-tunnel models could be treated as linear, mechanical filters simplified the airfoil calculations considerably. A similar conclusion for the structure of aircraft is suggested by the following reasoning. Inertial and spring forces in aircraft structure are usually linear; investigations of structural damping force ordinarily show that, although it is nonlinear, it is small compared to the critical damping force and may be adequately represented by linear equations. The characteristics of the aerodynamic damping are more in doubt, but the reasoning used in reference 15 to conclude that it is linearly proportional to velocity is appealing.

The question of whether the structure is linear may also be approached from another point of view. A proposition exists in filter theory to the effect that, if the probability densities of both the input and output signals are normally distributed, the filter is linear. It has been concluded in this report that the unsteady normal force on an airfoil profile is normally distributed; hence it is possible for the force input to an aircraft structure also to be normally distributed. If the first probability density of the output force (buffeting) is normally distributed, as appears to be the case in some observed instances, it is more than likely that an aircraft structure may be dealt with as though it were a linear filter.

Even in the event that aircraft structure cannot be generally represented as a linear filter, however, the suggested procedure still offers promise. Methods are outlined in reference 7 for dealing with nonlinear filters; possibly they can be adapted to the flight problem in much the same fashion as those pertaining to a linear filter have been adapted to the wind-tunnel calculations.

### CONCLUSIONS

The principal conclusions obtained from this experimental investigation of the unsteady normal force characteristics of 27 representative NACA profiles at Mach numbers up to 0.9, and Reynolds numbers of 1 to 2 million, may be briefly summarized:

1. Unsteady normal force occurred for some range of lift coefficient and Mach number for all airfoil sections investigated.
2. The magnitude of unsteady normal force is a function of Reynolds number. While the Reynolds number range of the tests appears in general to be too low to provide quantitative results directly applicable to full-scale aircraft, the data are considered adequate for evaluation of trends.
3. Of the four geometric parameters investigated, maximum thickness, camber, position of minimum pressure, and leading-edge radius, the first

~~CONFIDENTIAL~~

has the greatest effect upon unsteady normal force, decreased thickness providing noticeable reductions in magnitude. There is a maximum thickness-chord ratio, however, below which in general little reduction takes place, this thickness being 8 percent for the symmetrical NACA 65-series sections of the investigation.

4. Camber up to 0.4 design lift coefficient had little effect on the magnitude of unsteady normal force. An increase to 0.6 design lift coefficient applied to the 12-percent-thick NACA 65-series sections reduced the unsteady normal force somewhat, even at Mach numbers as high as 0.88.

5. Variations of unsteady normal force with position of minimum pressure from 30 to 60 percent of the chord, and with leading-edge radius below 0.15 chord were unimportant.

6. Abnormally large leading-edge radii increased to some extent the magnitude of unsteady normal force at high subsonic Mach numbers.

7. Unsteady normal force was a stationary random function of time, for which the first and higher probability densities were normally distributed. The spectral density is therefore sufficient to define the function.

8. At low Mach numbers and high lift coefficients the principal frequency components of unsteady normal force were largely confined to values below 200 cycles per second for the 6-inch-chord airfoils examined. Above 0.7 Mach number for high unsteady normal forces there appears to be a wider spread in the range of frequencies represented. None of the spectral densities was adequately represented by a "white noise" distribution.

9. Comparisons of unsteady normal-force section data with buffet boundaries measured for four straight-wing aircraft indicate there is a direct relationship, and provide evidence that unsteady normal force on the wing is one source of buffeting.

10. The methods derived to account for the influence of airfoil structure and spanwise variation of loading, which make use of linear-filter theory, frequency response functions, and the theory of stationary random time processes, may be useful in analyzing aircraft buffeting.

Ames Aeronautical Laboratory  
National Advisory Committee for Aeronautics  
Moffett Field, Calif., Mar. 2, 1955

## APPENDIX A

## PRESSURE-CELL RESULTS COMPARED WITH STRAIN GAGE

To appraise the results obtained with the pressure cells, simultaneous measurements of the root-mean-square unsteady normal forces were made for four profiles with the pressure cells and with the strain-gage equipment, using a common group of indicating instruments. The results are compared in figures 48 to 51. The forces in both cases were measured with the thermocouple meter to eliminate all discrepancies due to differences in wave form (i.e., differences in the first probability densities). The data have been adjusted in the manner described in Appendix C.

An examination first of the contour plots shows that, while discrepancies exist, the agreement on the whole is remarkably good. However, comparison of the root-mean-square unsteady normal-force coefficient versus lift-coefficient curves (part (b) of the figures) discloses variances somewhat larger than are apparent in the contour plots, the biggest differences usually occurring in the low Mach number and high-lift-coefficient region. The masking of this effect by the contour curves is due largely to the very sharp increases of unsteady normal force with small changes in lift coefficient.

These differences are attributed largely to errors in the pressure-cell results. The cells were not only somewhat removed from the airfoil surface, but also were submerged in the tunnel-wall boundary layer. In addition they were oriented to measure pressure in the spanwise direction instead of perpendicular to the model surface. For streamline steady-state flow closely approximating potential conditions, of course, orientation would have no influence on the results. Unsteady normal force, however, is generally accompanied by large regions of separated flow over the rear portion of the airfoil; and the turbulence in such a flow field is quite probably nonisotropic (ref. 16). Consequently, it would be expected, as already noted, that the largest discrepancies would occur at moderate Mach numbers and high angles of attack, where regions of separated flow are greatest.

Further information suggesting that most of the error is attributable to the pressure cells appears in figure 52, which compares the unsteady normal-force coefficients measured both by the straight-line and by the curvilinear pressure-cell installations (fig. 3), for the NACA 65-010 airfoil section. The data,<sup>1</sup> which are typical of those obtained for several other profiles, indicate that the unsteady normal forces measured are

---

<sup>1</sup>The curvilinear pressure-cell data were obtained from tests at constant  $\alpha_0$  and have been cross-plotted in figure 52 at constant M.

---

dependent upon cell location. Inasmuch as no detailed investigation was made to determine the best location, the arrangements chosen being a compromise between mechanical convenience and the desire to locate the cells as close to the model surface as possible, there is little reason to expect either combination to provide optimum results.

Not all the differences, however, can be charged to pressure-cell errors. Because the strain gage responds to area loading, the forces measured can, in accordance with the calculations described below and summarized in figure 53, be independent of span only if the instantaneous magnitude of the fluctuating load at each spanwise station is at every instant identical to that at all other spanwise stations. This condition requires that the correlation coefficient between all chordwise loadings be unity. In all other cases the forces will be less. No correlation measurements between spanwise stations were made, but the correlation coefficient between the instantaneous pressures at two spanwise points in the region of separated flow was determined in one instance and found to be low. It is therefore quite unlikely that the correlation coefficient between spanwise stations is one. Judging from the results of the calculations summarized in figure 53, however, and schlieren observations during the tests of the shock-wave motion and the coincidence of shock-wave location with the point of separation, it is felt that the correlation was sufficient to obtain upwards of 80 percent of the chordwise normal force per unit span from uncorrected strain-gage measurements.

Further comparisons of pressure-cell and strain-gage results are provided by the spectral-density curves of figure 54 obtained in the low Mach number and high lift coefficient region where the differences between results from the two sets of instrumentation are large. In each of these figures it is clear that the significant differences are not confined to a narrow range of frequencies, but are distributed over the entire spectrum. There is proportionately as much variance in the higher frequencies as in the low, although the absolute differences are of course larger in the latter region.

On the basis of all these considerations it is concluded that, while differences exist and neither method of measurement is free of defects, the agreement is sufficiently good to provide assurance that the unsteady normal force occurring in the wind tunnel was measured with reasonable accuracy.

The calculations relating the total unsteady load measured by the strain gage to the unsteady normal load per unit span, were carried out by (a) replacing the instantaneous load across the span with an equivalent load at midspan giving the same deflection, (b) computing the mean-square value of this equivalent load as a function of  $\lambda/b$ , and (c) determining the limiting value of (b) for  $\lambda/b \rightarrow \infty$  and dividing by this

quantity to determine the proportion of normal force indicated by the strain gage for any scale of correlation  $\lambda/b$ .

By application of the principle of virtual displacements to a simply supported beam loaded at any point a distance  $x$  from the end:

$$dN_1(x,t) = \frac{\delta(x)}{\delta_1} g(x,t) dx$$

where  $\delta_1$  is the displacement at midspan resulting from the load  $g(x,t) dx$  at point  $x$ . Also, from the equation for deflection of such a beam loaded in the manner described

$$\frac{\delta(x)}{\delta_1} = \frac{3xb^2 - 4x^3}{b^3}; \quad 0 \leq x \leq \frac{b}{2}$$

therefore

$$dN_1(x,t) = \frac{3xb^2 - 4x^3}{b^3} g(x,t) dx$$

and

$$N_1(t) = 2 \int_0^{b/2} \frac{3xb^2 - 4x^3}{b^3} g(x,t) dx$$

The mean-square value of  $N_1(t)$  is obtained in the following fashion, which is the same as that used in reference 17:

$$\overline{N_i^2} = \lim_{T \rightarrow \infty} \frac{1}{T} \int_0^T [N_i(t)]^2 dt$$

$$\begin{aligned} [N_i(t)]^2 &= 4 \left[ \int_0^{b/2} \frac{3xb^2 - 4x^3}{b^3} g(x,t) dx \right]^2 \\ &= \frac{4}{b^6} \int_0^{b/2} \int_0^{b/2} (3xb^2 - 4x^3)(3yb^2 - 4y^3) g(x,t) g(y,t) dy dx \end{aligned}$$

$$\overline{N_i^2} = \frac{4}{b^6} \lim_{T \rightarrow \infty} \frac{1}{T} \int_0^T dt \int_0^{b/2} \int_0^{b/2} (3xb^2 - 4x^3)(3yb^2 - 4y^3) g(x,t) g(y,t) dy dx$$

$$= \frac{4}{b^6} \int_0^{b/2} \int_0^{b/2} (3xb^2 - 4x^3)(3yb^2 - 4y^3) dy dx \lim_{T \rightarrow \infty} \frac{1}{T} \int_0^T g(x,t) g(y,t) dt$$

$$\lim_{T \rightarrow \infty} \frac{1}{T} \int_0^T g(x,t) g(y,t) dt = \overline{g(x)g(y)} = \sqrt{[\overline{g(x)}]^2} \sqrt{[\overline{g(y)}]^2} r(x,y)$$

where  $r(x,y)$  is the correlation coefficient between  $g(x)$  and  $g(y)$ .

No data are available for determining  $r(x,y)$ ; but, for want of a better assumption, a function sometimes used to approximate the correlation coefficient between the pressures at two points in a turbulent flow field (ref. 17) may be assumed:

$$r(x,y) = \left( 1 - \frac{|y-x|}{2\lambda} \right) e^{-\frac{|y-x|}{\lambda}}$$

Also,

$$\overline{[g(x)]^2} = \overline{[g(y)]^2} = \overline{g^2}$$

Substitution of these values in the expression for  $\overline{N_1^2}$  yields

$$\overline{[N_1(\lambda/b)]^2} = \frac{4}{b^6} \int_0^{b/2} \int_0^{b/2} (3xb^2 - 4x^3)(3yb^2 - 4y^3) \overline{g^2} \left(1 - \frac{|y-x|}{2\lambda}\right) e^{-\frac{|y-x|}{\lambda}} dy dx$$

$$\overline{[N_1(\lambda/b)]^2} = 4 \frac{\overline{g^2}}{b^6} \int_0^{b/2} (3xb^2 - 4x^3) dx \int_x^{b/2} (3yb^2 - 4y^3) \left(1 - \frac{y-x}{2\lambda}\right) e^{-\frac{y-x}{\lambda}} dy +$$

$$4 \frac{\overline{g^2}}{b^6} \int_0^{b/2} (3xb^2 - 4x^3) dx \int_0^x (3yb^2 - 4y^3) \left(1 - \frac{x-y}{2\lambda}\right) e^{-\frac{x-y}{\lambda}} dy$$

The second of these two integrals may be shown to be equal to the first, by substituting

$$u = y$$

$$v = x$$

for which

$$\frac{\partial(x,y)}{\partial(u,v)} = -1$$

Hence, finally

$$\overline{[N_1(\lambda/b)]^2} = 8 \frac{\overline{g^2}}{b^6} \int_0^{b/2} (3xb^2 - 4x^3) dx \int_x^{b/2} (3yb^2 - 4y^3) \left(1 - \frac{y-x}{2\lambda}\right) e^{-\frac{y-x}{\lambda}} dy$$

The evaluation of this integral, although tedious, is straightforward. Only the result is stated here:

$$\begin{aligned} \frac{[N_1(\lambda/b)]^2}{b^2 \bar{g}^2} = & \left[ \frac{17}{35} \left(\frac{2\lambda}{b}\right) + \frac{6}{5} \left(\frac{2\lambda}{b}\right)^3 - \frac{33}{4} \left(\frac{2\lambda}{b}\right)^4 + 36 \left(\frac{2\lambda}{b}\right)^5 - 54 \left(\frac{2\lambda}{b}\right)^6 \right] + \\ & e^{-\frac{b}{2\lambda}} \left[ \frac{3}{2} \left(\frac{2\lambda}{b}\right)^2 + \frac{3}{2} \left(\frac{2\lambda}{b}\right)^3 - \frac{15}{2} \left(\frac{2\lambda}{b}\right)^4 - 27 \left(\frac{2\lambda}{b}\right)^5 - 9 \left(\frac{2\lambda}{b}\right)^6 + \right. \\ & \left. 54 \left(\frac{2\lambda}{b}\right)^7 + 54 \left(\frac{2\lambda}{b}\right)^8 \right] \end{aligned} \quad (A1)$$

For large values of  $\lambda/b$  this equation may be more compactly expressed as a power series in terms of its reciprocal,

$$\begin{aligned} \frac{[N_1(\lambda/b)]^2}{b^2 \bar{g}^2} = & \frac{1}{2} \sum_{n=0}^{n=\infty} \left[ \frac{3}{(n+2)!} - \frac{3}{(n+3)!} - \frac{15}{(n+4)!} + \frac{54}{(n+5)!} - \frac{18}{(n+6)!} - \right. \\ & \left. \frac{108}{(n+7)!} + \frac{108}{(n+8)!} \right] \frac{(-1)^n}{(2\lambda/b)^n} \\ = & \frac{25}{64} - \frac{0.1595}{2\lambda/b} + \frac{0.04458}{(2\lambda/b)^2} - \frac{0.009560}{(2\lambda/b)^3} + \frac{0.001670}{(2\lambda/b)^4} - \frac{0.0002469}{(2\lambda/b)^5} + \dots \end{aligned}$$

The ratio of mean-square unsteady normal force indicated by the strain gage for a scale of correlation,  $\lambda$ , to that for infinite scale of correlation is therefore

$$\frac{[N_1(\lambda/b)]^2}{[N_1(\infty)]^2} = \frac{64}{25} f(\lambda/b)$$

where  $f(\lambda/b)$  is the right-hand side of equation (A1).

Numerical results are plotted against semilogarithmic coordinates in figure 53. It is apparent that the strain-gage results are dependent upon the scale of correlation for values of  $\lambda/b$  less than 1; and, since the results were not corrected to account for the scale of correlation, they understate the true unsteady normal force per unit span. This error is, of course, directly opposite to that introduced by the pressure cells, which overestimate the force per unit span.

## APPENDIX B

## WIND-TUNNEL EFFECTS

## Tunnel Resonance

The experimental and theoretical work reported in references 18, 19, and 20 indicates that the oscillating lift measured for an airfoil mounted in a wind tunnel is affected by the presence of the tunnel walls. This interference is greatest when the frequency of oscillation coincides with the acoustic frequency corresponding to a wave length twice the tunnel height, or any odd divisor of this length, and is evidenced by a large loss in measured lift at that frequency. Lift forces at frequencies other than resonance (or odd multiples thereof) are also affected, the amount of distortion depending primarily upon free-stream Mach number and airfoil-chord to tunnel-height ratio. The pulsating lift upon which the theory of these references is based was obtained by assuming the existence of oscillating pressure doublets. The results therefore, should be applicable to this investigation as well as to the measurement of the lift of an oscillating airfoil, for which they are primarily intended.

The resonant frequency at which unsteady normal force should vanish (with no damping present) is noted on the 16 spectral-density plots of figure 47. In every case loss of unsteady normal force at the indicated frequency is apparent. There is no evidence of loss at odd multiples of the resonant frequency, but the measured forces are too small to conclude whether the effect is present or not. The magnitude of the loss of unsteady normal force at the fundamental resonant frequency is generally somewhat less than would have been expected. For some spectral densities, however, resonance appears to occur within the frequency range of the large peak (e.g., fig. 47(a),  $M = 0.655$  ( $\alpha_0 = 8.27^\circ$ ),  $M = 0.704$ ; fig. 45(b),  $M = 0.563, 0.608, 0.655, 0.707, 0.760$ ; and fig. 47(c),  $M = 0.705$ ) and provides a plausible explanation for the precipitous loss of unsteady normal force with increased frequency which is so noticeable.

Some additional information concerning this phenomenon is presented in figure 55, which is a plot of the spectral density of the output of the cells installed in the floor and ceiling of the tunnel obtained for the same airfoil and test conditions as the spectral density of figure 47(d) for Mach number 0.556. The fundamental resonant frequencies indicated by both sets of data are identical. In addition, the 3rd, 5th, 7th, and 9th harmonics were detected by the pressure cells, although nothing is shown by the airfoil spectral density.

For the test point just discussed, the amount of unsteady normal force in the immediate vicinity of  $f_T$  is small. A larger proportion

of unsteady normal force at  $f_{\pi}$  would result in increased pressures at the floor and ceiling cells. The output of these cells can therefore be used to detect the coincidence of tunnel resonant frequency with predominant normal-force frequency. This condition was actually encountered in a few isolated instances, but only for airfoils not included in this report.

In summary, there is ample evidence that the resonant condition investigated in references 18 to 20 was present during the tests and that it affected the data in measurable degree. The effects for the most part, however, are unimportant, appearing small even in the vicinity of resonance. As an estimate, the area under the spectral-density curves (i.e.,  $(\Delta c_n')^2$ ) is distorted by not more than 10 percent, corresponding to 5 percent of the root-mean-square unsteady normal-force coefficient.

#### Airfoil Resonance

Although the spectral densities indicate that airfoil resonance was of little consequence in unsteady normal-force measurements, it is interesting to note that the pressure pulsations created by the model vibration, while weak, were nevertheless picked up by the floor and ceiling cells during measurements of the spectral density of figure 55. (The small discrepancy between the airfoil frequency noted here and in figure 47(d) is attributed to difference of wind-tunnel conditions existing during the two observations.) The conditions which would result should the model frequency coincide with either the tunnel resonant frequency or with one of the predominant unsteady normal-force frequencies furnish an interesting topic for speculation. Such a combination of events, however, was never encountered during this investigation.

## APPENDIX C

## UNSTEADY NORMAL-FORCE CORRECTIONS

The unsteady normal-force coefficients measured by the strain gage were corrected by use of the following equation:

$$\sqrt{(\Delta c_n)^2} = \sqrt{(\Delta c_n')^2 - v^2}$$

where  $v$ , the noise factor, is the unsteady normal-force coefficient measured at zero lift coefficient and approximately 0.5 Mach number (values at lower Mach numbers were substantially the same). This equation was derived by assuming that the correlation coefficient,  $r_S$ , between the noise factor and the corrected unsteady normal-force coefficient was zero:

$$\Delta c_n'(t) = \Delta c_n(t) + v(t)$$

$$\overline{(\Delta c_n')^2} = \overline{(\Delta c_n)^2} + \overline{v^2} + 2v(\Delta c_n)$$

Solving for  $\overline{(\Delta c_n)^2}$

$$\overline{(\Delta c_n)^2} = \overline{(\Delta c_n')^2} - \overline{v^2} - 2v(\Delta c_n)$$

$$v(\Delta c_n) = r_S \sqrt{\overline{v^2}} \sqrt{\overline{(\Delta c_n)^2}}$$

$$r_S = 0$$

$$v(\Delta c_n) = 0$$

$$\sqrt{(\Delta c_n)^2} = \sqrt{(\Delta c_n')^2 - v^2}$$

While it probably is not true that the unsteady normal force and noise factor are totally uncorrelated, it is certain that the correlation is of

a very low order; and in the absence of more precise knowledge this assumption is considered reasonable. It is further to be observed that, since  $\sqrt{v^2}$  was always less than 0.004, the corrections would be small even in the extreme case of  $r_g = 1$ .

The pressure-cell data were corrected on the assumption that the correlation coefficient  $r_p = \frac{v\Delta c_n}{\sqrt{v^2} \sqrt{(\Delta c_n)^2}}$  was unity, leading to the equation

$$\Delta c_{n_{rms}} = \Delta c_{n'_{rms}} - \sqrt{v^2}$$

The values of  $\sqrt{v^2}$  were determined in the same manner as for the strain-gage data; in the case of the pressure cells, however, they were somewhat larger, ranging from 0.006 to 0.009.

The use of  $r_p = 1$  is not intended to imply that the correlation between signal and noise is higher for pressure-cell than for strain-gage data. The value was chosen for the strictly pragmatic reason that it minimizes the discrepancies between the two sets of data, particularly at high angles of attack, and applies the larger corrections to the pressure-cell data, which are considered the less reliable.

## REFERENCES

1. Baker, Thomas F.: Results of Measurements of Maximum Lift and Buffeting Intensities Obtained During Flight Investigation of the Northrop X-4 Research Airplane. NACA RM L53G06, 1953.
2. Green, Milton: Notes on the Buffet Problem. Chance Vought Aircraft, Dallas Division of United Aircraft Corp. March 18, 1953.
3. Humphreys, Milton D.: Pressure Pulsations on Rigid Airfoils at Transonic Speeds. NACA RM L51112, 1952.
4. Humphreys, Milton D., and Kent, John D.: The Effects of Camber and Leading-Edge-Flap Deflection on the Pressure Pulsations on Thin Rigid Airfoils at Transonic Speeds. NACA RM L52G22, 1952.
5. Coe, Charles F., and Mellenthin, Jack A.: Buffeting Forces on Two-Dimensional Airfoils as Affected by Thickness and Thickness Distribution. NACA RM A53K24, 1954.
6. Rice, S. O.: Mathematical Analysis of Random Noise. Bell System Technical Journal, vol. 23, no. 3, 1944, pp. 282-332, and vol. 24, no. 1, 1945, pp. 46-156.
7. Lawson, James L., and Uhlenbeck, George E., eds.: Threshold Signals. Vol. 24, Radiation Laboratory Series. McGraw-Hill Book Company, Inc., 1950.
8. James, Hubert M., Nichols, Nathaniel B., and Phillips, Ralph S., eds.: Theory of Servomechanisms. Vol. 25, Radiation Laboratory Series, McGraw-Hill Book Company, Inc., 1950.
9. Abbott, Ira H., von Doenhoff, Albert E., and Stivers, Louis S., Jr.: Summary of Airfoil Data. NACA Rep. 824, 1945.
10. Wrathall, Taft: Miniature Pressure Cells. Paper No. 52-S-4, Proc. of Instr. Soc. of America, vol. 7, 1952.
11. Daley, Bernard N., and Hanna, Lillian E.: Subsonic Two-Dimensional-Flow Conditions Near an Airfoil Determined by Static Pressures Measured at the Tunnel Wall. NACA TN 1873, 1949.
12. Timoshenko, S.: Vibration Problems in Engineering. Second ed., D. Van Nostrand Company, Inc., 1937.
13. Allen, H. Julian, and Vincenti, Walter G.: Wall Interference in a Two-Dimensional-Flow Wind Tunnel with Consideration of the Effects of Compressibility. NACA Rep. 782, 1944.

14. Gadeberg, Burnett L., and Ziff, Howard A.: Flight-Determined Buffet Boundaries of Ten Airplanes and Comparison With Five Buffeting Criteria. NACA RM A50I27, 1951.
15. Huston, Wilber B., and Skopinski, T. H.: Measurements and Analysis of Wing and Tail Buffeting Loads on a Fighter-Type Airplane. NACA TN 3080, 1954.
16. Schubauer, Galen Brandt, and Klebanoff, P. S.: Investigation of Separation of the Turbulent Boundary Layer. NACA Rep. 1030, 1951.
17. Liepmann, Hans Wolfgang: An Approach to the Buffeting Problem From Turbulence Considerations. Douglas Aircraft Co., Inc., Santa Monica. Rep. No. SM-13940, 1951.
18. Runyan, Harry L., and Watkins, Charles E.: Considerations on the Effect of Wind-Tunnel Walls on Oscillating Air Forces for Two-Dimensional Subsonic Compressible Flow. NACA Rep. 1150, 1953.
19. Runyan, Harry L., Woolston, Donald S., and Rainey, Gerald A.: A Theoretical and Experimental Study of Wind-Tunnel-Wall Effects on Oscillating Air Forces for Two-Dimensional Subsonic Compressible Flow. NACA RM L52I17a, 1953.
20. Woolston, Donald S., and Runyan, Harry L.: Some Considerations on the Air Forces on a Wing Oscillating Between Two Walls for Subsonic Compressible Flow. I.A.S. Preprint No. 446, 1954.

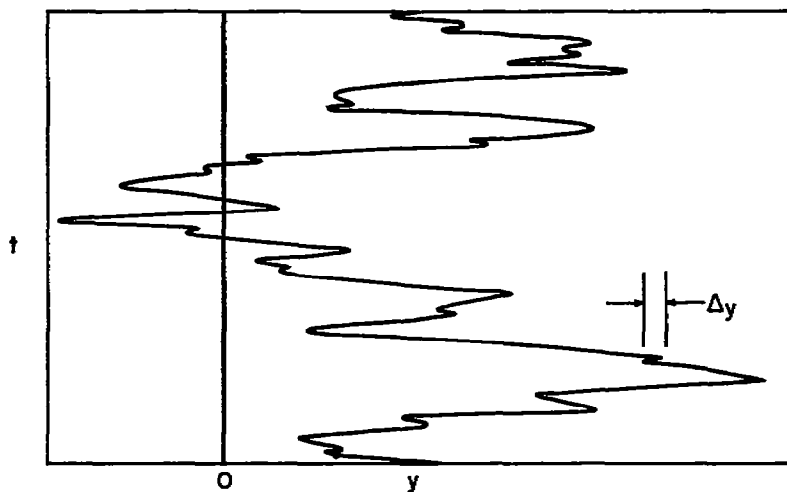
TABLE I.- LIST OF PROFILES TESTED GROUPED ACCORDING TO PURPOSE

Variation of geometric parameters			
Thickness	Camber	Position of minimum pressure	Leading-edge radius
<sup>1</sup> NACA 65-004	<sup>1</sup> NACA 65-012	NACA 63-010	NACA 0010-0.27-40/1.051
NACA 65-006	NACA 65-212	NACA 64-010	NACA 0010-0.70-40/1.051
NACA 65-008	NACA 65-412	<sup>1</sup> NACA 65-010	NACA 0010-1.10-40/1.051
<sup>1</sup> NACA 65-010	NACA 65-612	NACA 66-010	NACA 0010-1.50-40/1.051
<sup>1</sup> NACA 65-012			
NACA 2-004	<sup>1</sup> NACA 65-004		10-percent-thick circular arc } 0 0.27 0.70
NACA 2-006	NACA 65-204		
NACA 2-008	NACA 65-404		
Comparison with flight		Reynolds number	
NACA 23018		<sup>1</sup> NACA 23013 6- and 12-inch chord	
<sup>1</sup> NACA 65-213, $a = 0.5$		<sup>1</sup> NACA 65-213, $a = 0.5$ , 6- and 12-inch chord	
<sup>1</sup> NACA 65-110			
Statistical aspects of the data, instrumentation			
NACA 0006-64			
<sup>1</sup> NACA 65-110			
NACA 23013			
<sup>1</sup> NACA 65-213, $a = 0.5$			

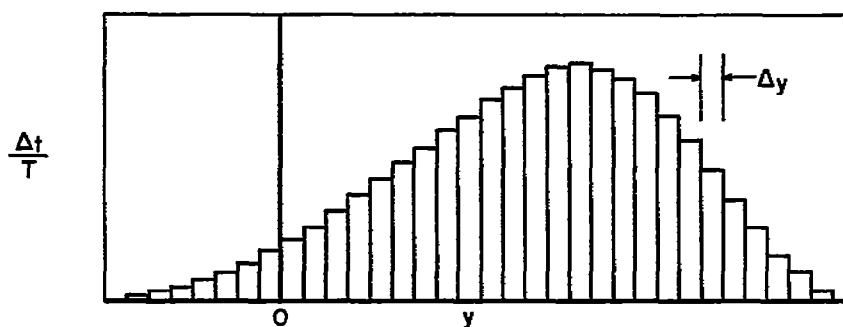
<sup>1</sup>Duplicate listing

~~CONFIDENTIAL~~

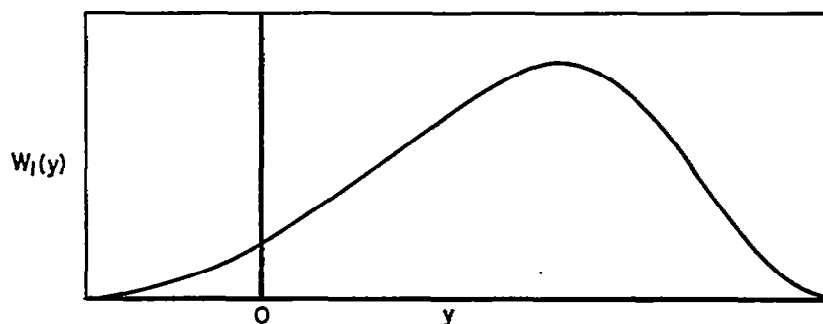
~~CONFIDENTIAL~~



(a) Stationary random function of time

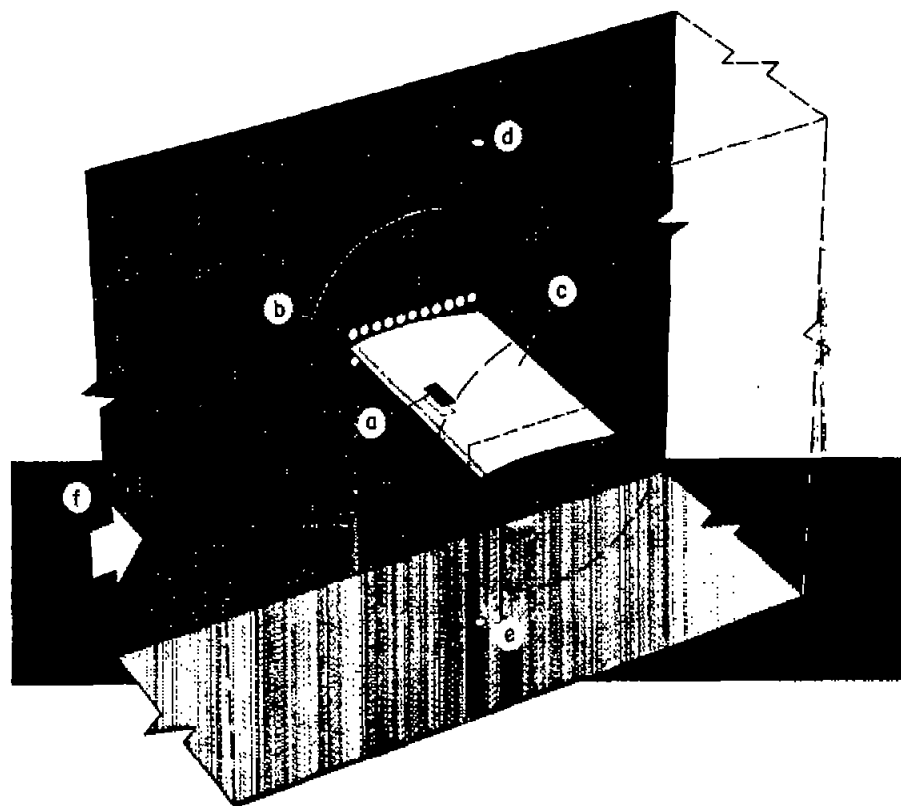


(b) Histogram



(c) First probability density

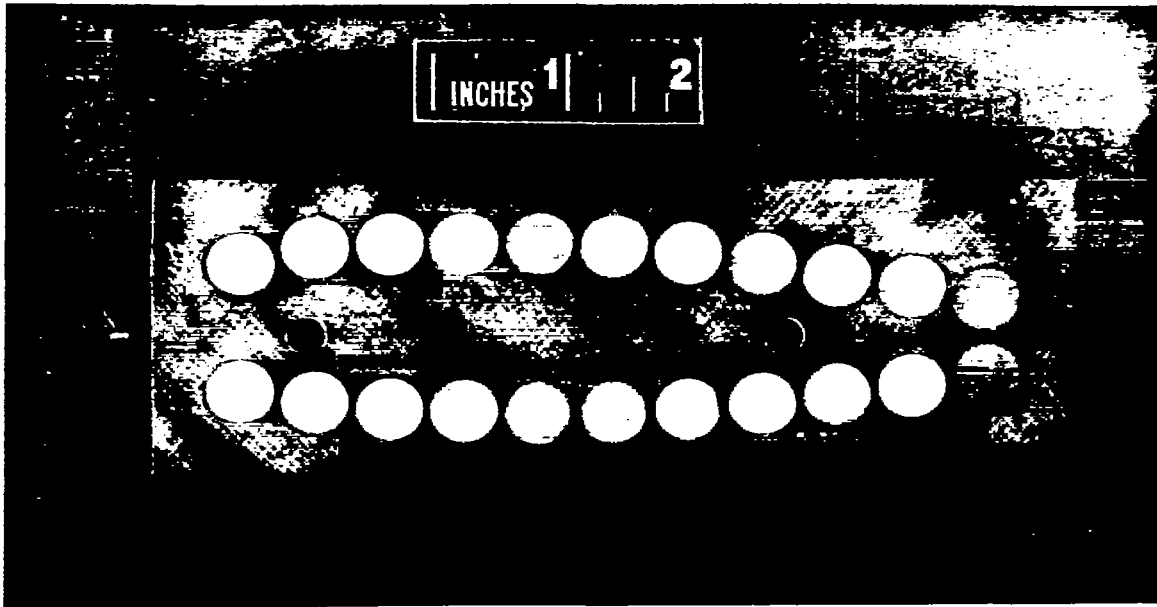
Figure 1.- Determination of the first probability density from a stationary random function of time.



- |                          |                           |
|--------------------------|---------------------------|
| (a) Strain gage pickup   | (d) Ceiling pressure cell |
| (b) Pressure cells       | (e) Floor pressure cell   |
| (c) Model (6 inch chord) | (f) Direction of airflow  |

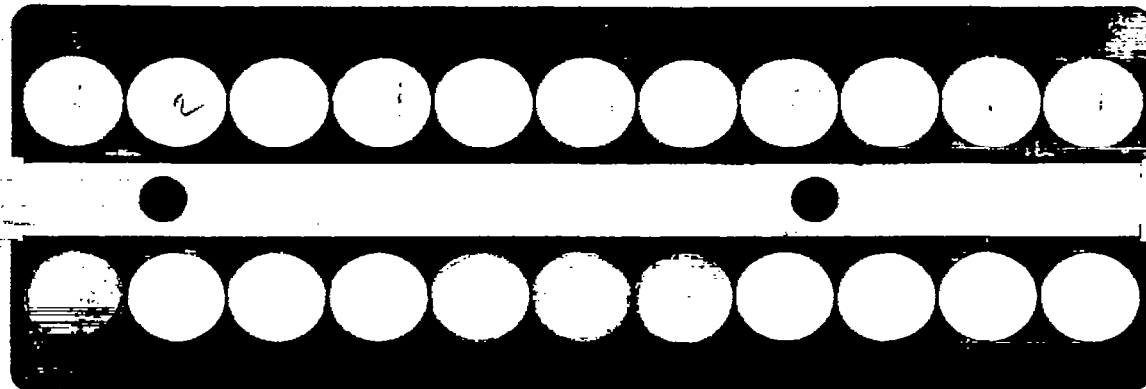
A-19153

Figure 2.- Arrangement of 6-inch-chord model and pickup devices in test section of Ames 1- by 3-1/2-foot wind tunnel.



A-17738

(a) Curvilinear cell installation.



A-19058.1

(b) Straight-line cell installation.

Figure 3.- Photograph of the pressure-cell installations in side wall of 1- by 3-1/2-foot wind tunnel.

CONFIDENTIAL

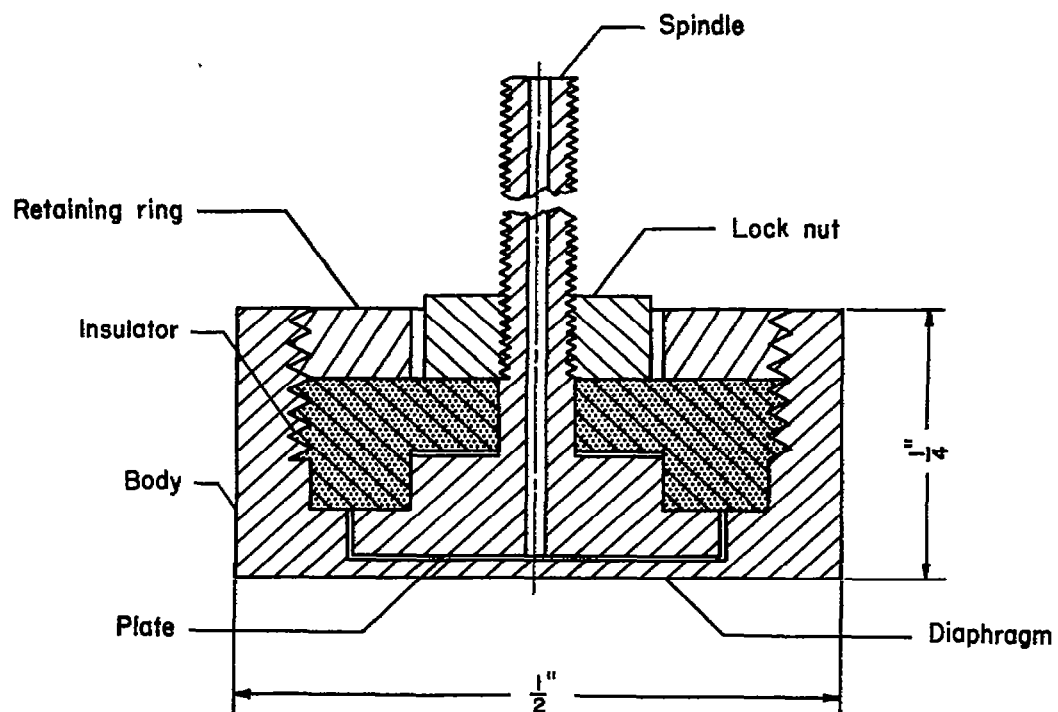


Figure 4.- Cross-sectional view of a pressure cell.

CONFIDENTIAL

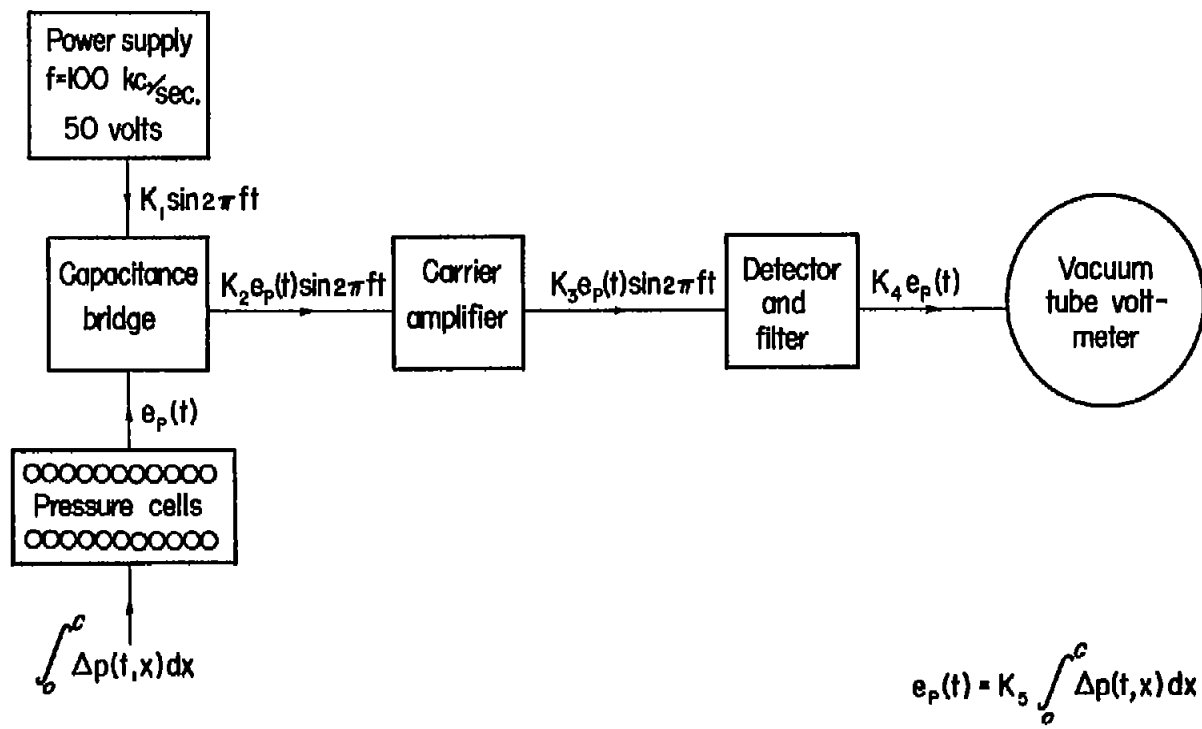


Figure 5.- Block diagram of the pressure-cell equipment.

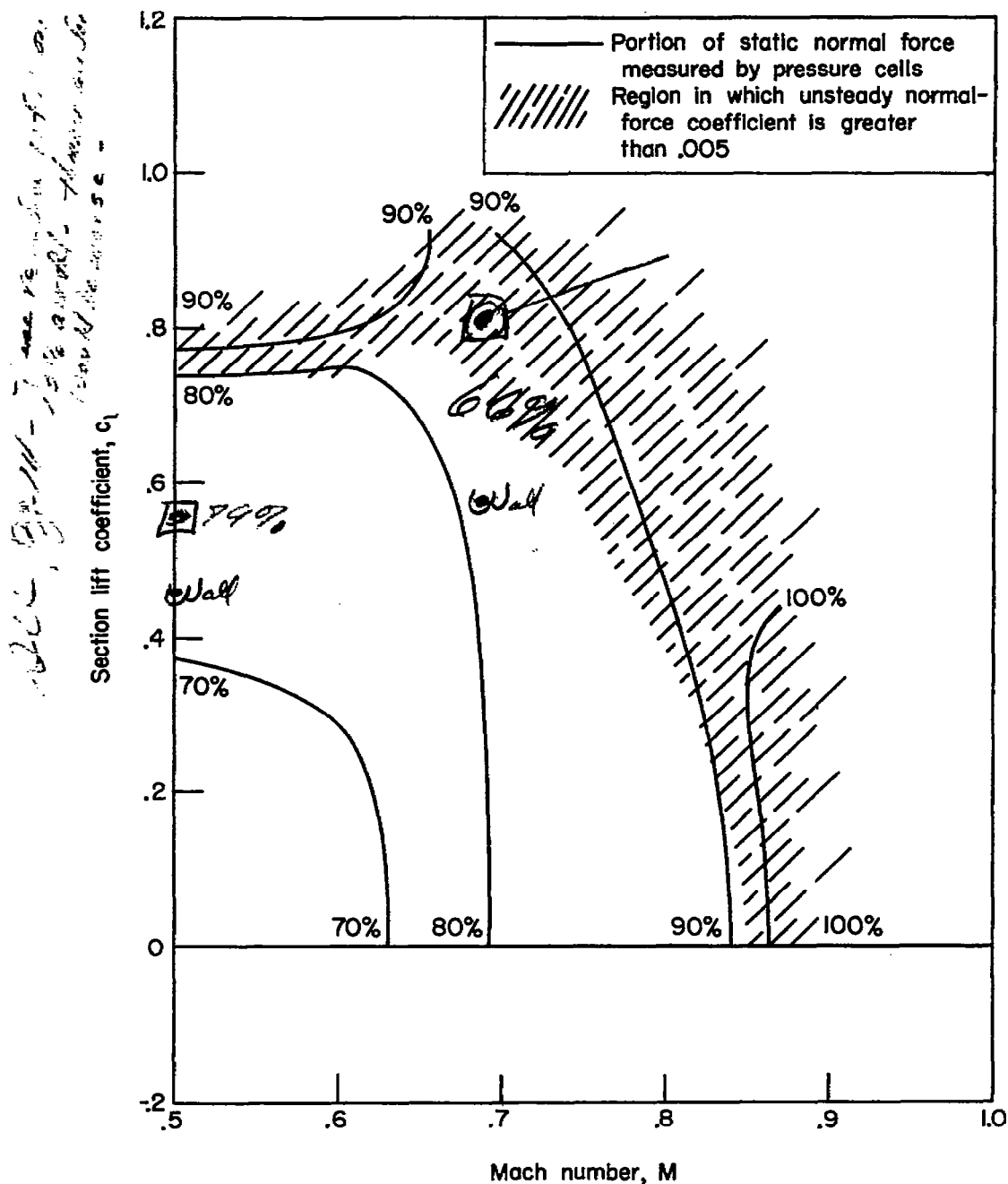


Figure 6.- Contours of proportion of static normal-force coefficient measured by the curvilinear pressure-cell installation, NACA 65-010 airfoil section.

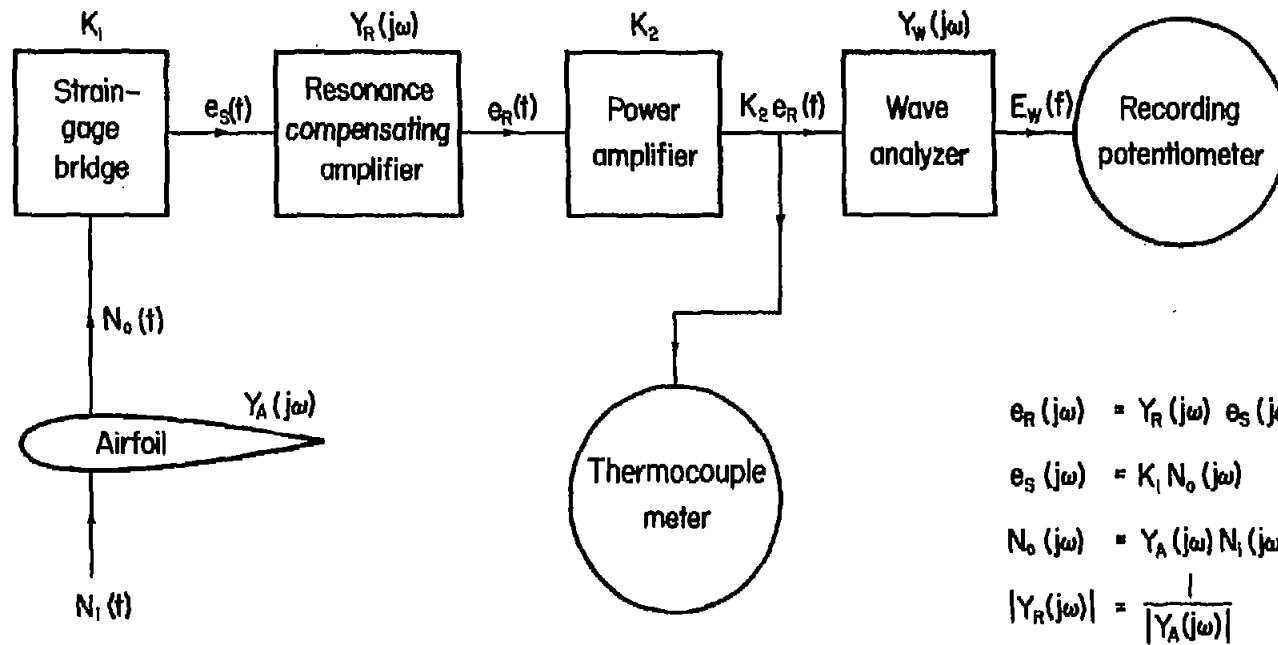


Figure 7.- Block diagram of the strain-gage equipment.

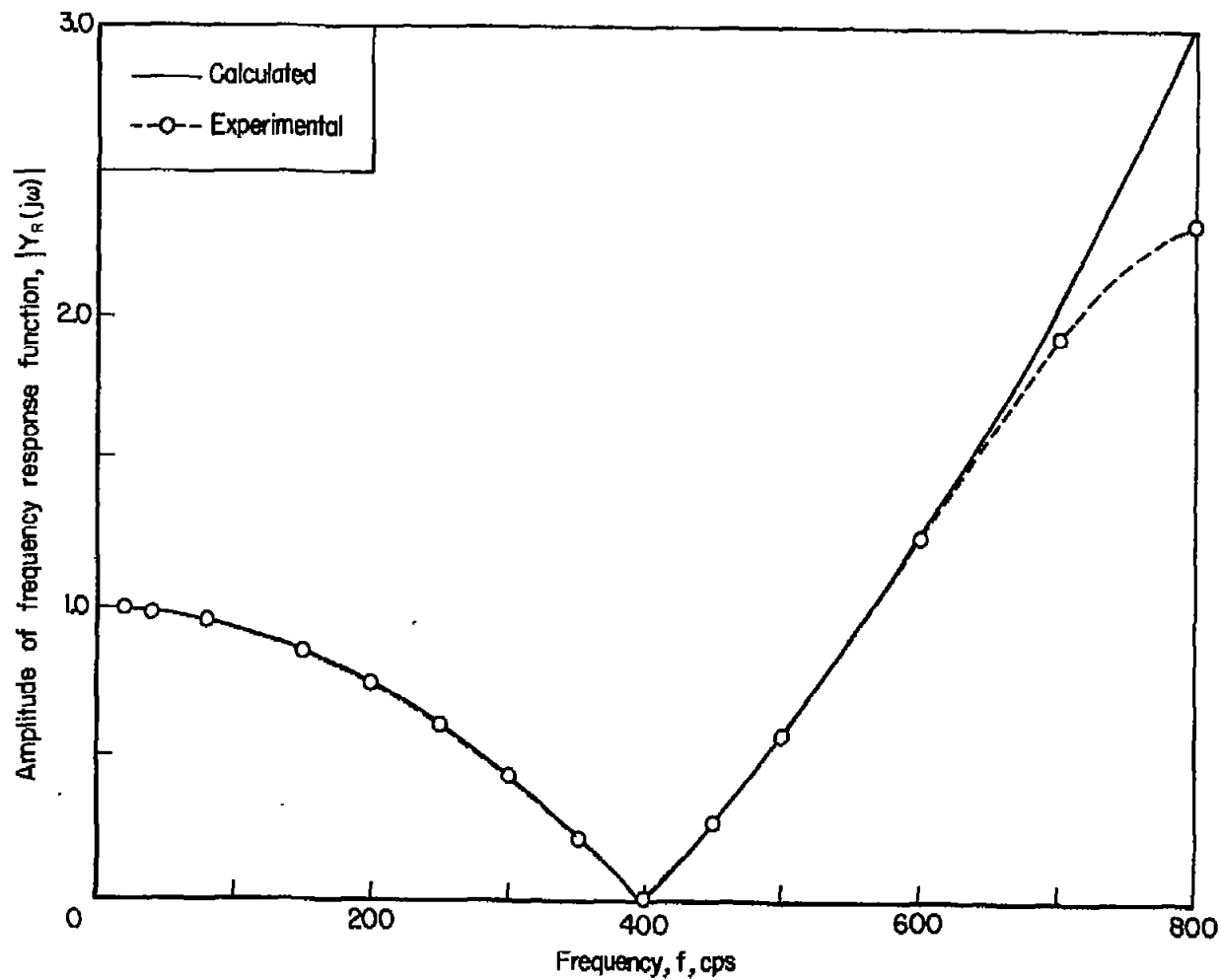


Figure 8.- Comparison with theory of the amplitude of the experimental frequency response function of the resonance compensating amplifier.

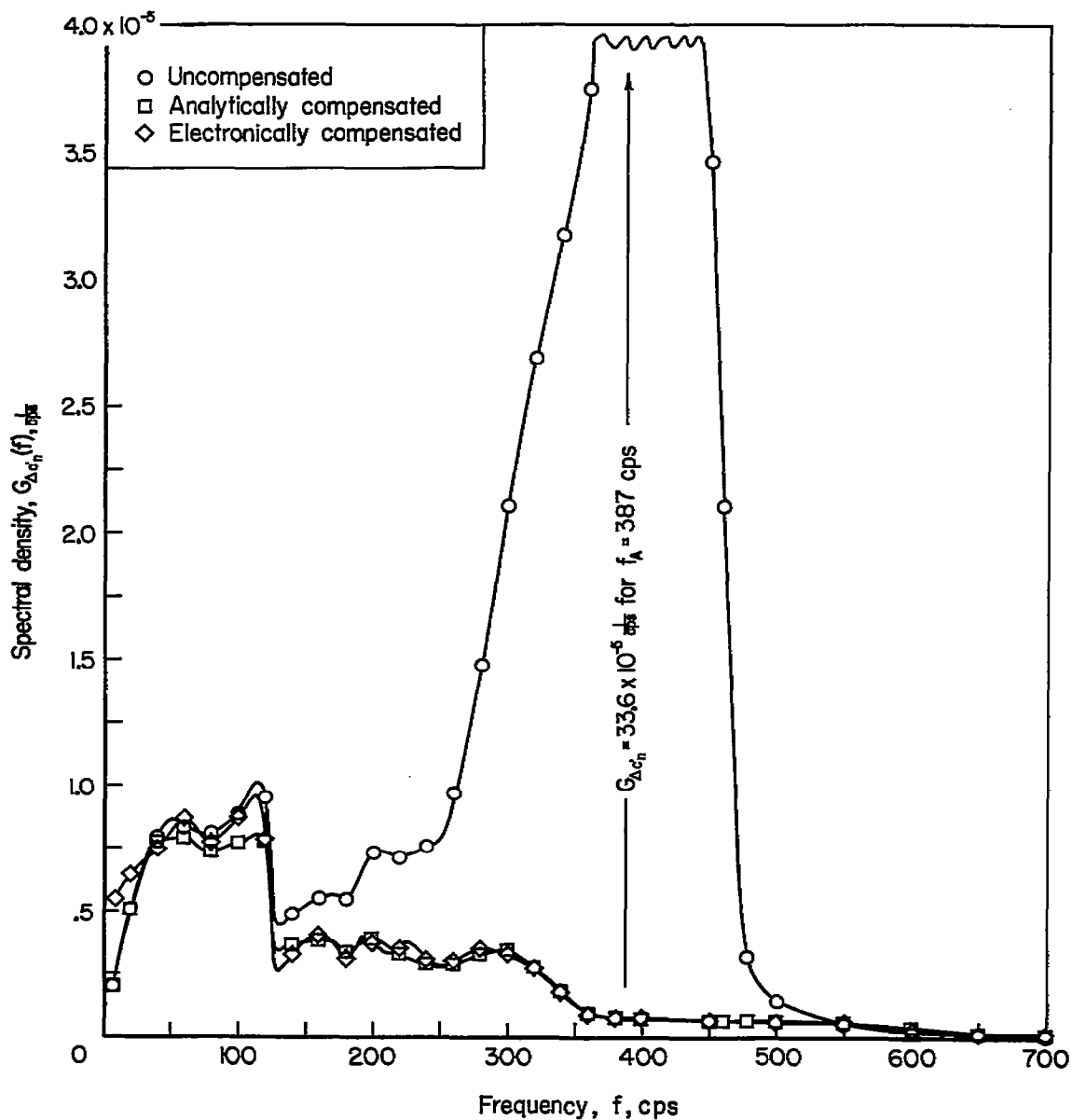


Figure 9.- Typical spectral densities of section unsteady normal-force coefficient, uncompensated, analytically compensated, and measured with the resonance compensating amplifier; NACA 23013 airfoil section,  $M = 0.655$ ,  $c_l = 0.73$ ,  $\alpha = 10^\circ$ .

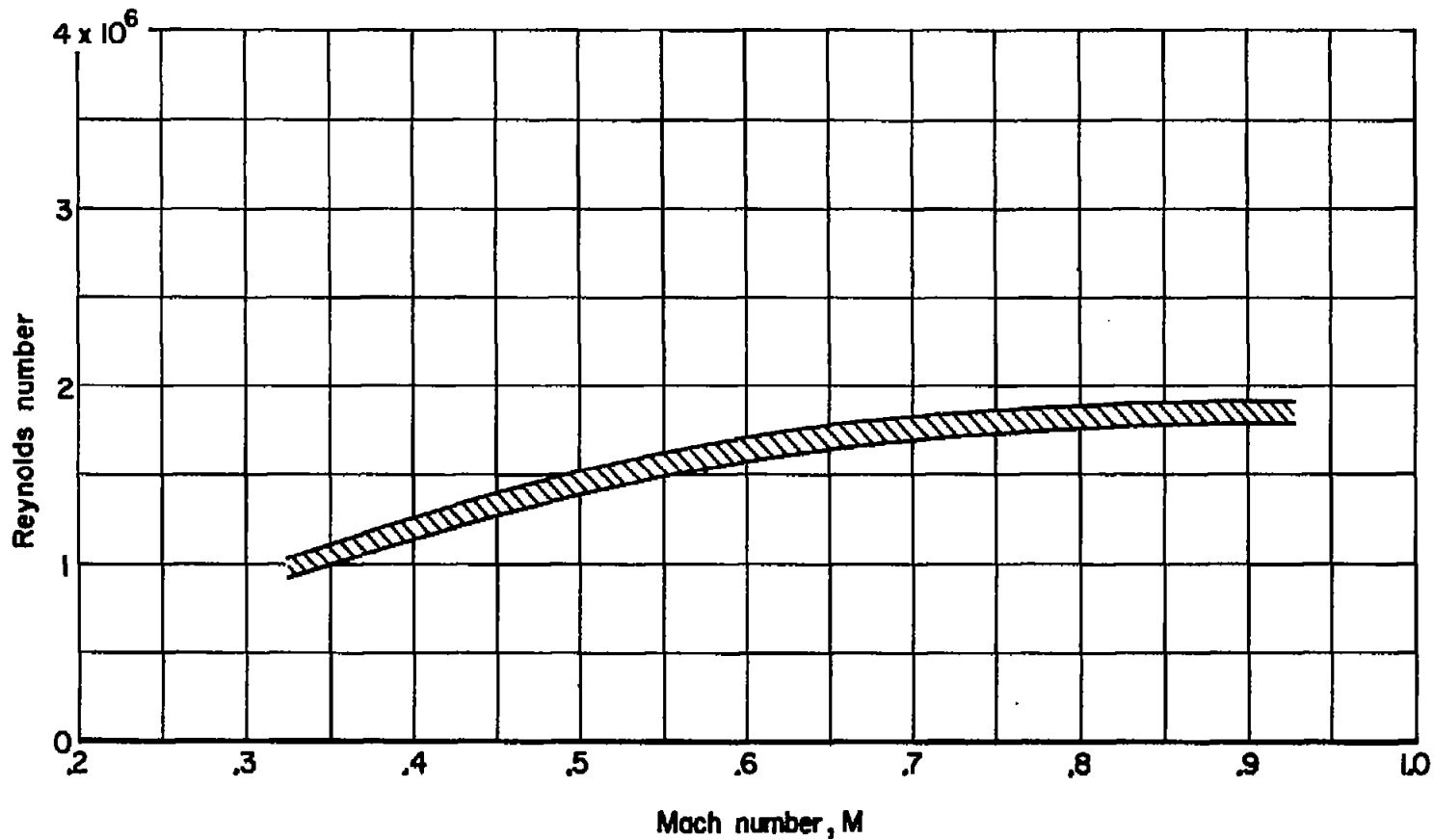
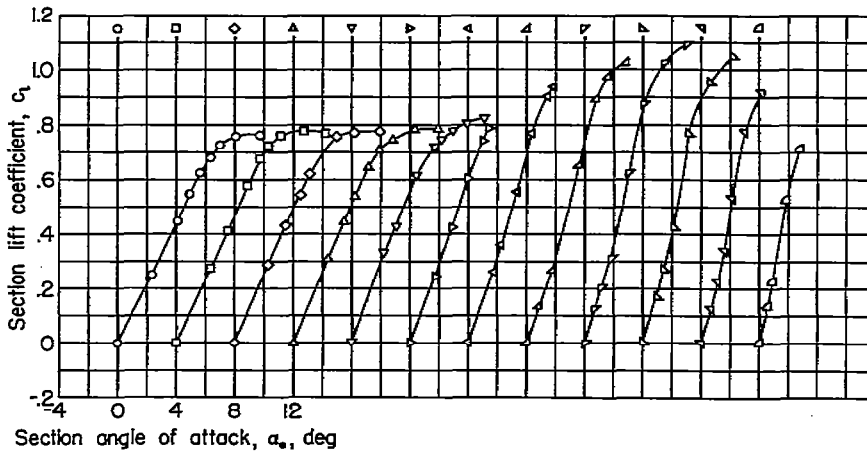
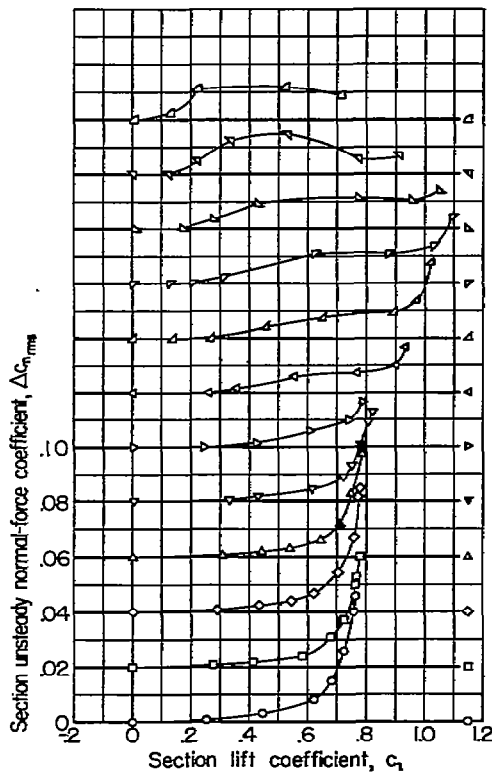


Figure 10.- Variation of Reynolds number with Mach number for 6-inch-chord models in the Ames 1- by 3-1/2-foot high-speed wind tunnel.

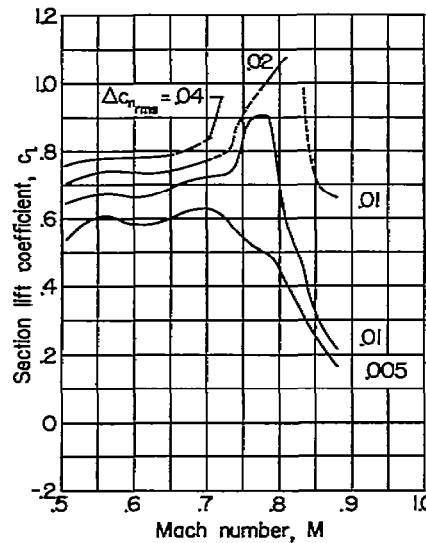


(a) Variation of section lift coefficient with section angle of attack for various Mach numbers.



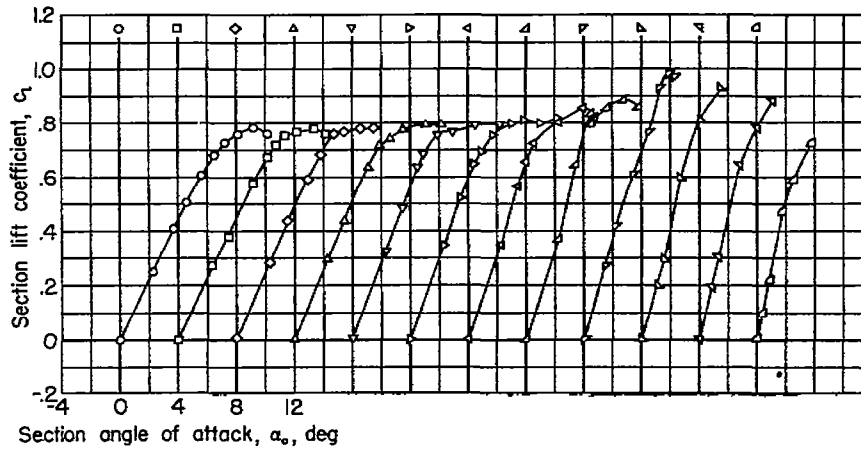
(b) Variation of section unsteady normal-force coefficient with section lift coefficient for various Mach numbers.

Mach number, M		
○ 506	▽ 707	▽ 808
□ 555	▷ 731	▷ 831
◇ 605	◀ 759	◀ 856
△ 654	◀ 784	△ 882

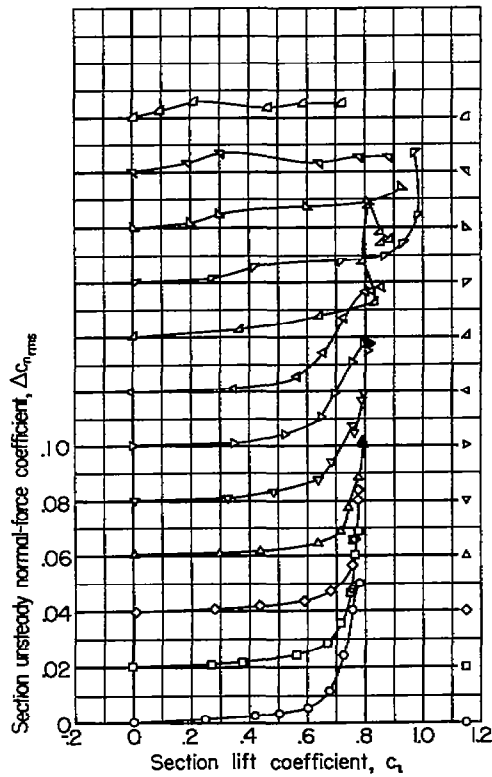


(c) Section unsteady normal-force coefficient contours.

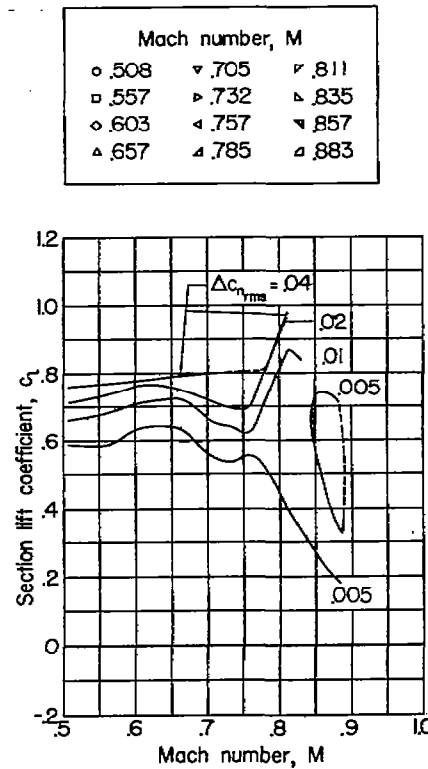
Figure 11.- Lift coefficient and unsteady normal-force characteristics of the NACA 65-004 profile.



(a) Variation of section lift coefficient with section angle of attack for various Mach numbers.

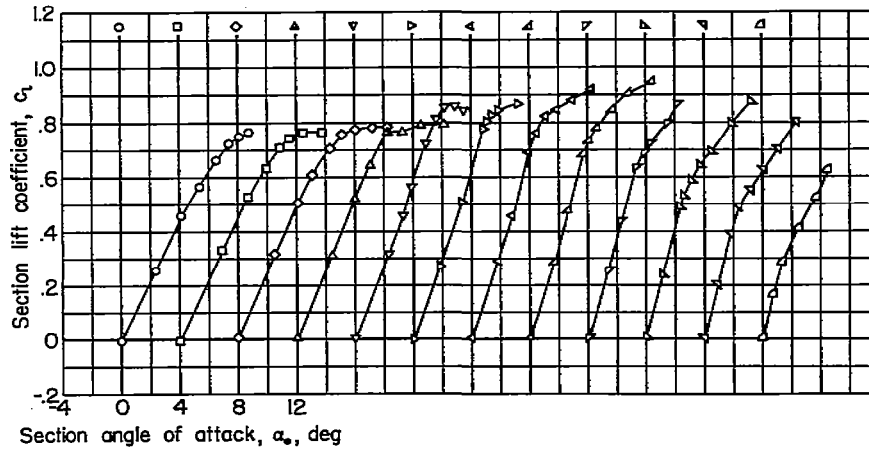


(b) Variation of section unsteady normal-force coefficient with section lift coefficient for various Mach numbers.

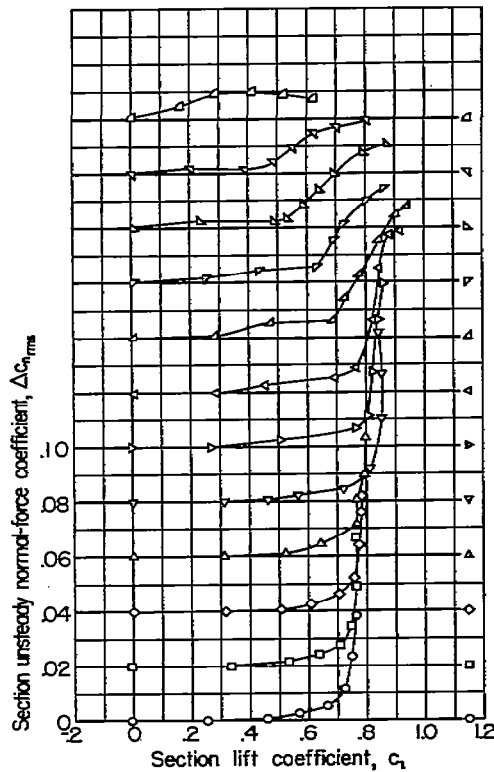


(c) Section unsteady normal-force coefficient contours.

Figure 12.- Lift coefficient and unsteady normal-force characteristics of the NACA 65-006 profile.

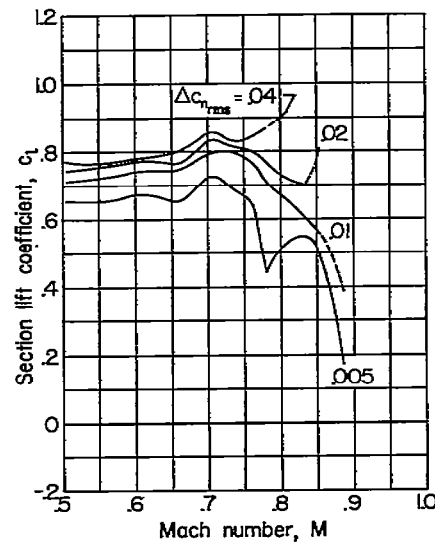


(a) Variation of section lift coefficient with section angle of attack for various Mach numbers.



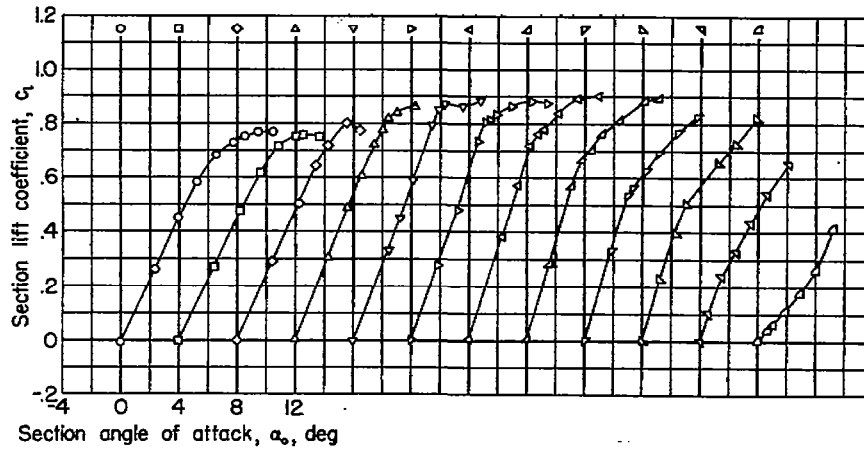
(b) Variation of section unsteady normal-force coefficient with section lift coefficient for various Mach numbers.

Mach number, M		
○ .505	▽ .705	▽ 807
□ .553	▷ .732	▷ 833
◇ .602	◁ .757	◁ 854
△ .652	▲ .781	▲ 886

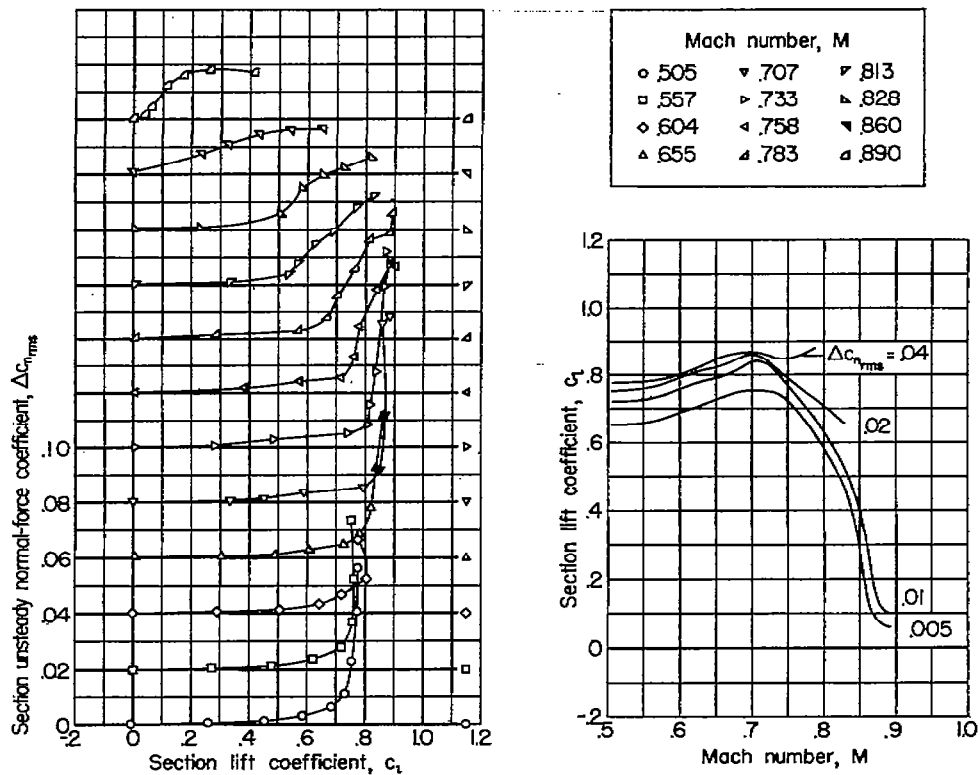


(c) Section unsteady normal-force coefficient contours.

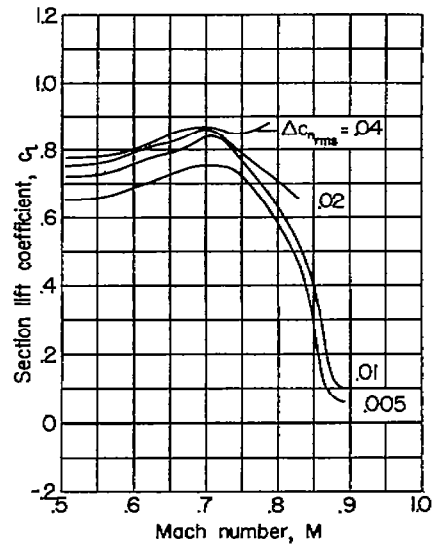
Figure 13.- Lift coefficient and unsteady normal-force characteristics of the NACA 65-008 profile.



(a) Variation of section lift coefficient with section angle of attack for various Mach numbers.

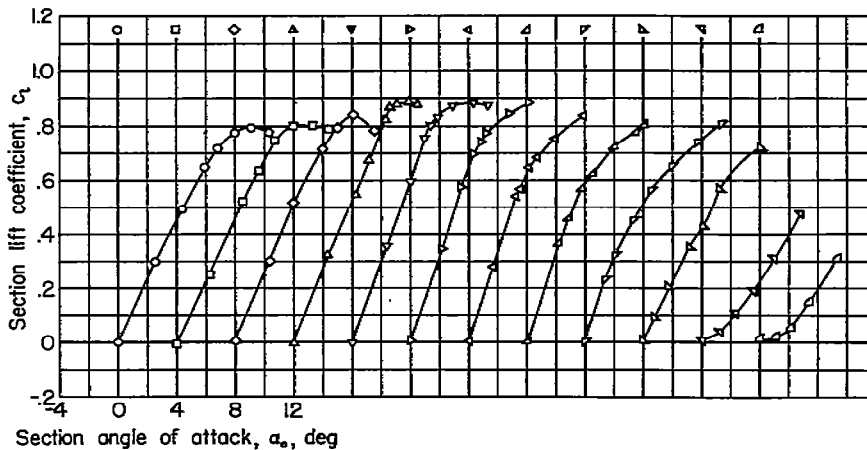


(b) Variation of section unsteady normal-force coefficient with section lift coefficient for various Mach numbers.

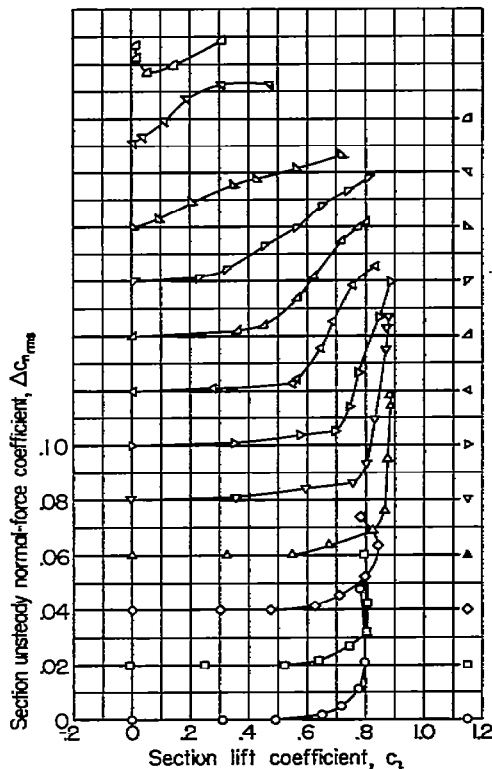


(c) Section unsteady normal-force coefficient contours.

Figure 14.- Lift coefficient and unsteady normal-force characteristics of the NACA 65-010 profile.

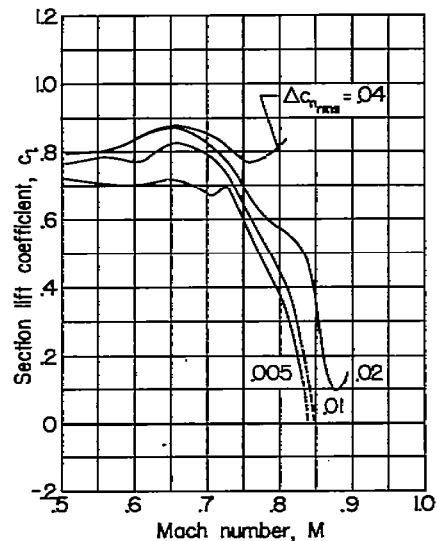


(a) Variation of section lift coefficient with section angle of attack for various Mach numbers.



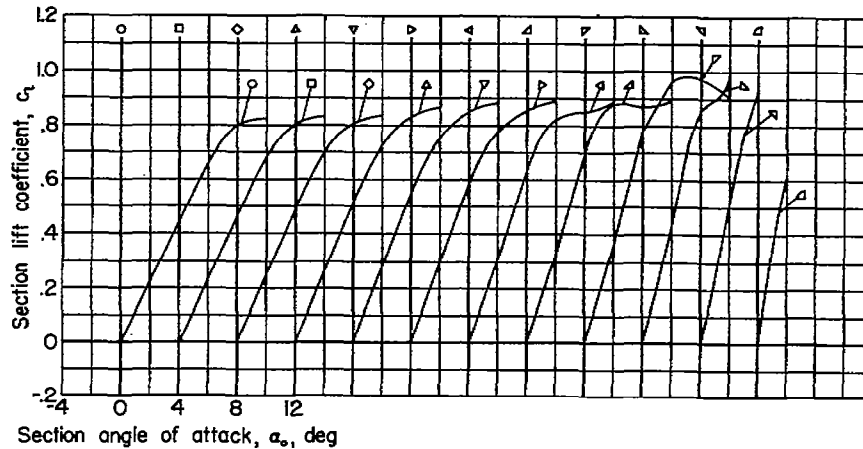
(b) Variation of section unsteady normal-force coefficient with section lift coefficient for various Mach numbers.

Mach number, M		
o .506	∇ .704	▽ .807
□ .554	▷ .729	△ .835
◇ .606	◀ .757	∇ .869
▲ .654	△ .779	△ .894

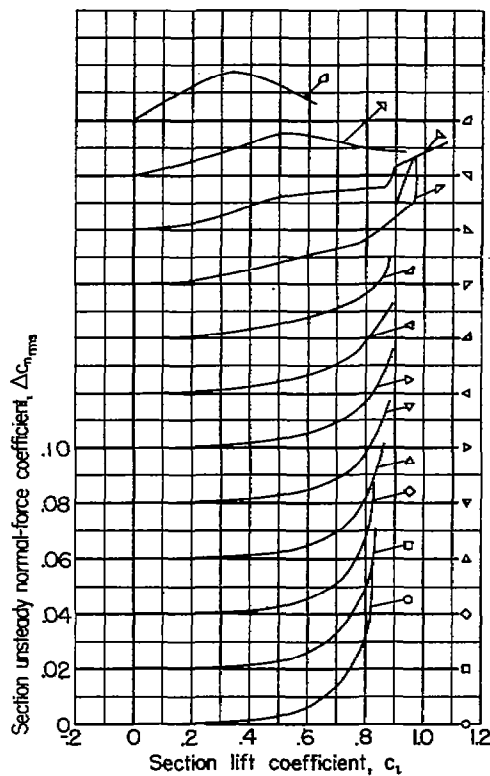


(c) Section unsteady normal-force coefficient contours.

Figure 15.- Lift coefficient and unsteady normal-force characteristics of the NACA 65-012 profile.

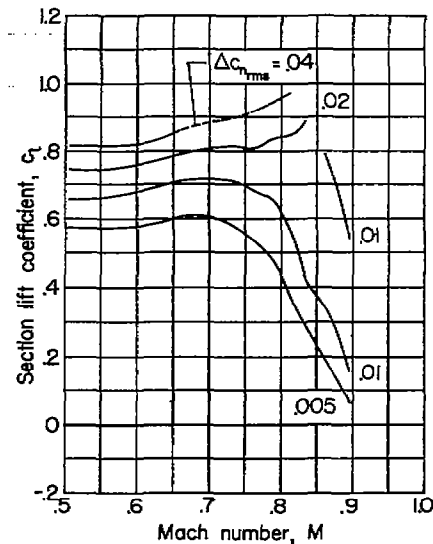


(a) Variation of section lift coefficient with section angle of attack for various Mach numbers.



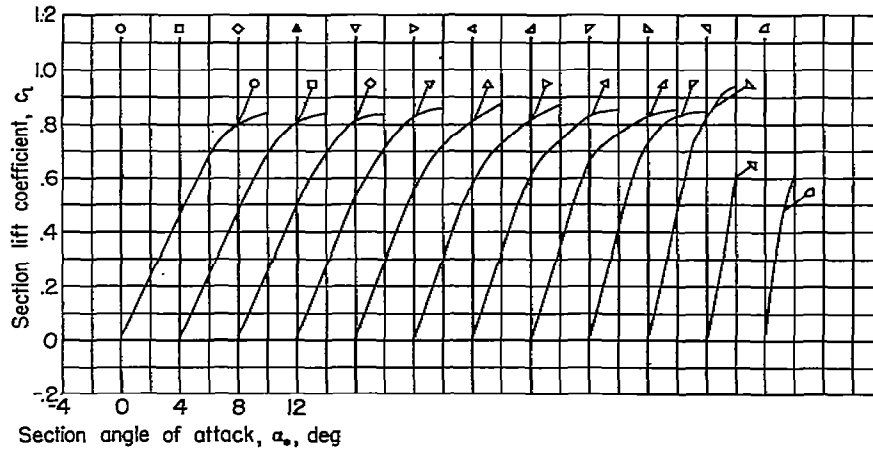
(b) Variation of section unsteady normal-force coefficient with section lift coefficient for various Mach numbers.

Mach number, M		
○ .505	▽ .707	▽ .810
□ .556	▷ .732	△ .834
◇ .607	◁ .758	▽ .860
△ .656	△ .782	△ .896

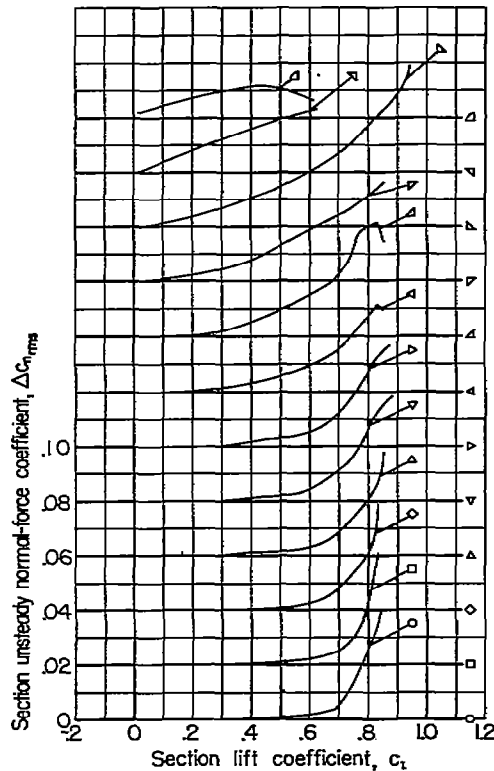


(c) Section unsteady normal-force coefficient contours.

Figure 16.- Lift coefficient and unsteady normal-force characteristics of the NACA 2-004 profile.

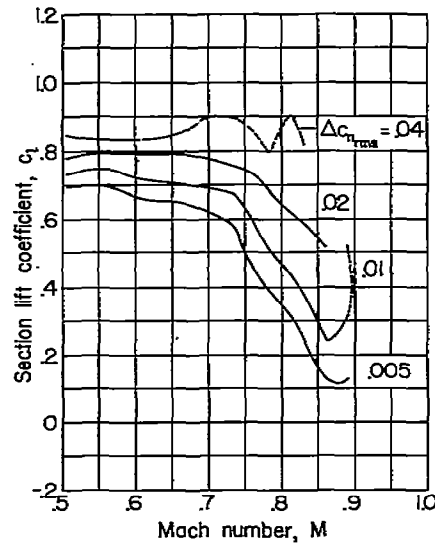


(a) Variation of section lift coefficient with section angle of attack for various Mach numbers.



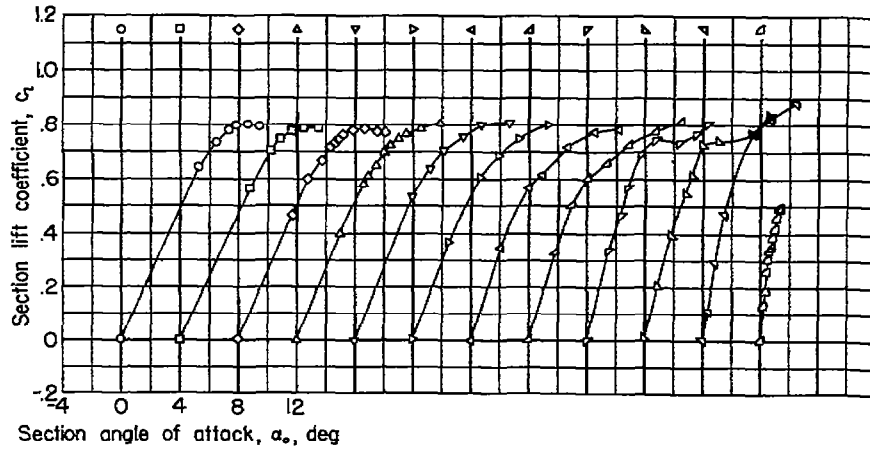
(b) Variation of section unsteady normal-force coefficient with section lift coefficient for various Mach numbers.

Mach number, M		
○ .505	▽ .707	▷ .812
□ .555	▷ .733	▷ .835
◇ .606	◁ .759	▽ .861
△ .656	△ .784	△ .890

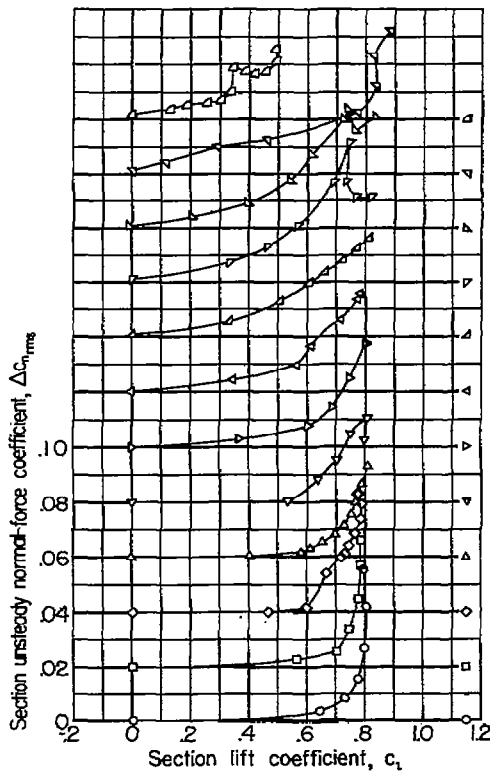


(c) Section unsteady normal-force coefficient contours.

Figure 17.- Lift coefficient and unsteady normal-force characteristics of the NACA 2-006 profile.

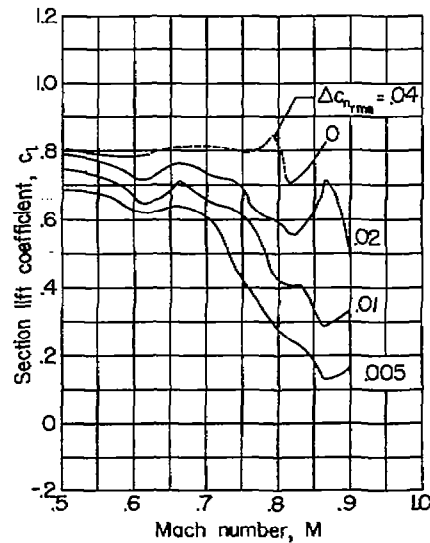


(a) Variation of section lift coefficient with section angle of attack for various Mach numbers.



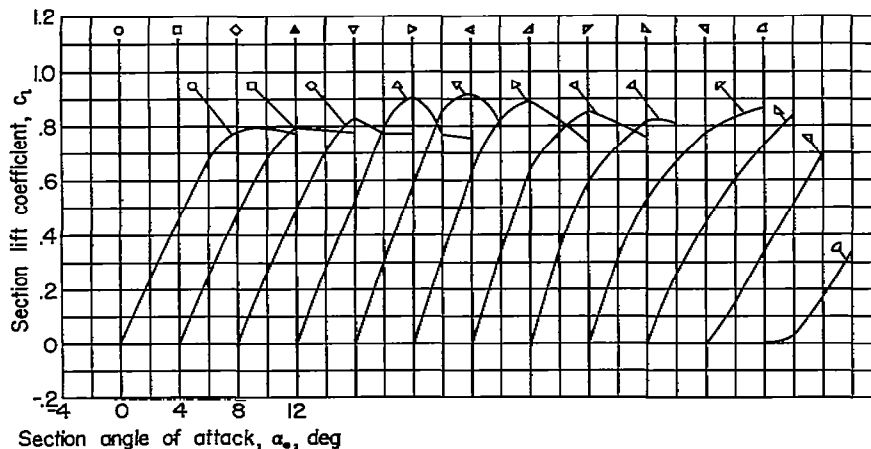
(b) Variation of section unsteady normal-force coefficient with section lift coefficient for various Mach numbers.

Mach number, M		
○ 502	▽ 708	▽ 820
□ 554	▷ 735	▷ 830
◇ 610	◁ 765	▽ 854
△ 662	△ 790	△ 900

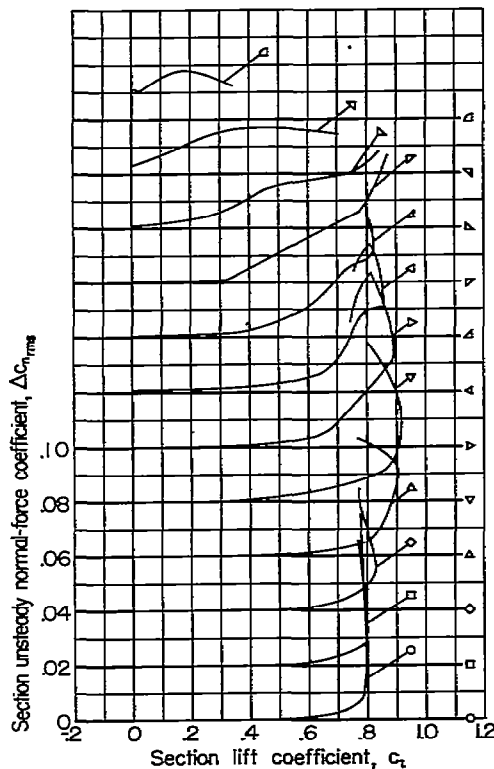


(c) Section unsteady normal-force coefficient contours.

Figure 18.- Lift coefficient and unsteady normal-force characteristics of the NACA 2-008 profile.

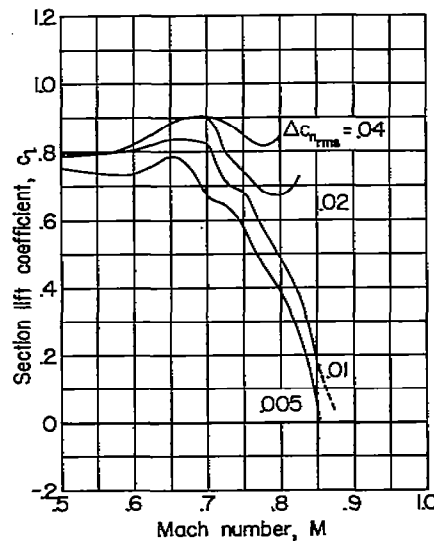


(a) Variation of section lift coefficient with section angle of attack for various Mach numbers.



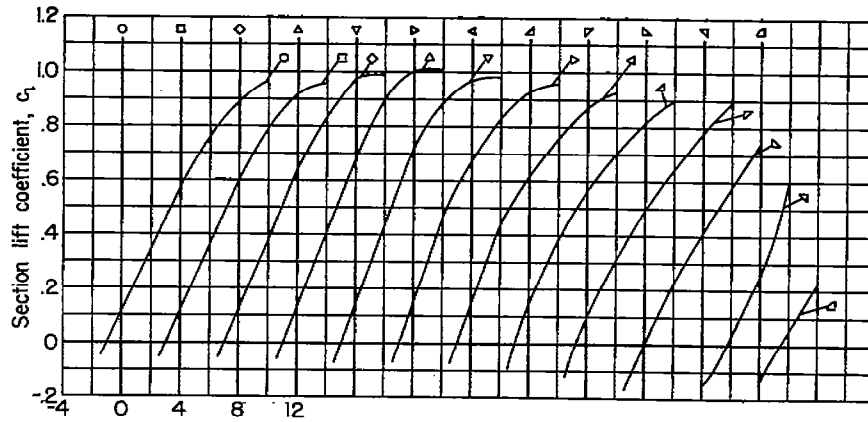
(b) Variation of section unsteady normal-force coefficient with section lift coefficient for various Mach numbers.

Mach number, M		
○ .500	▽ .700	▷ .800
□ .550	▷ .725	▷ .825
◇ .600	◁ .750	▷ .850
△ .650	△ .775	△ .875

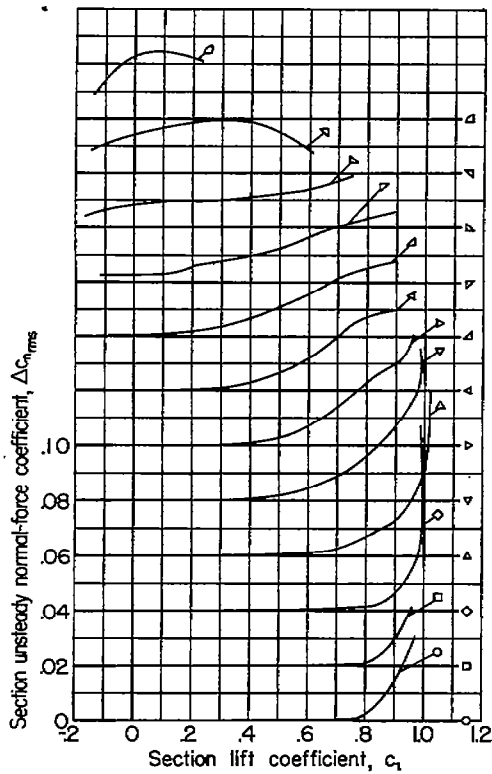


(c) Section unsteady normal-force coefficient contours.

Figure 19.- Lift coefficient and unsteady normal-force characteristics of the NACA 65-012 profile.

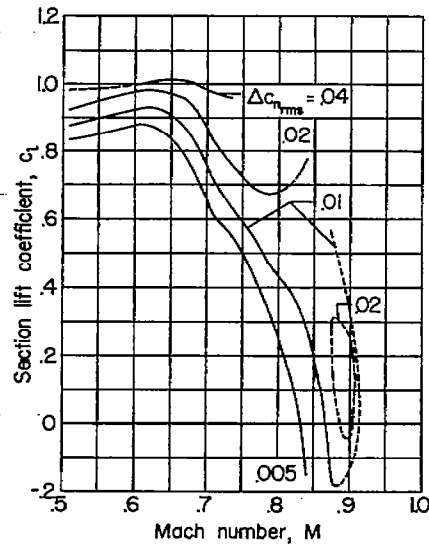


(a) Variation of section lift coefficient with section angle of attack for various Mach numbers.



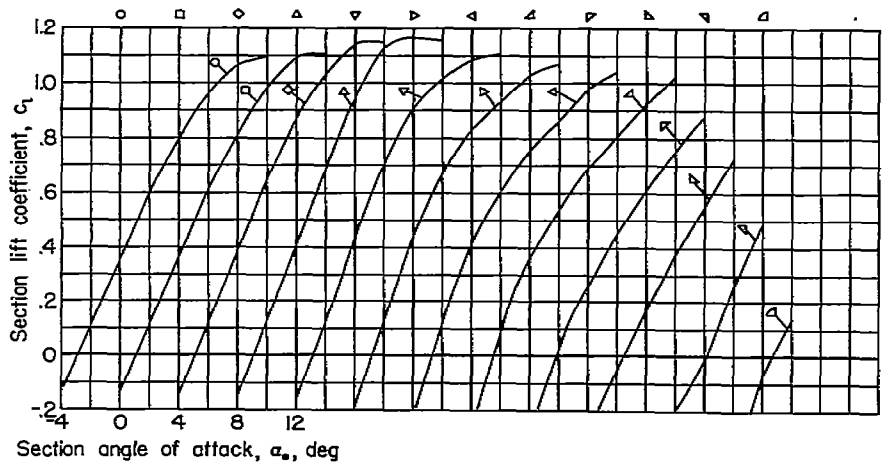
(b) Variation of section unsteady normal-force coefficient with section lift coefficient for various Mach numbers.

Mach number, M		
○ .508	▽ .707	▽ .812
□ .555	▷ .731	▷ .840
◇ .605	◁ .760	▽ .870
△ .657	△ .785	△ .900

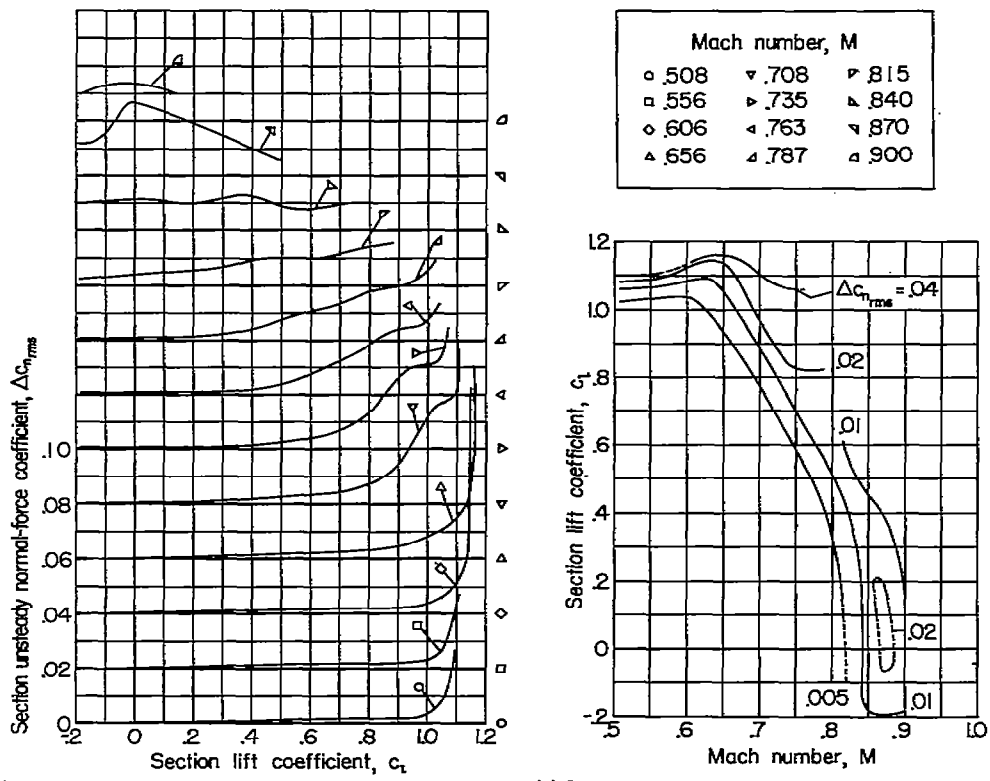


(c) Section unsteady normal-force coefficient contours.

Figure 20.- Lift coefficient and unsteady normal-force characteristics of the NACA 65-212 profile.



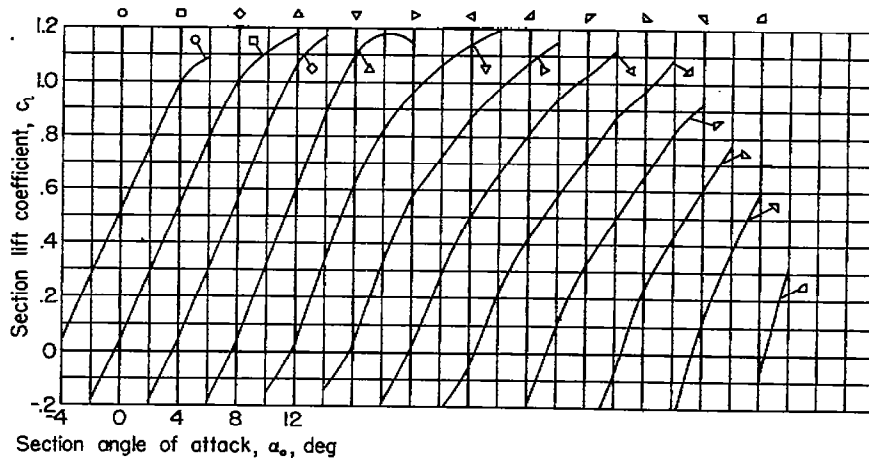
(a) Variation of section lift coefficient with section angle of attack for various Mach numbers.



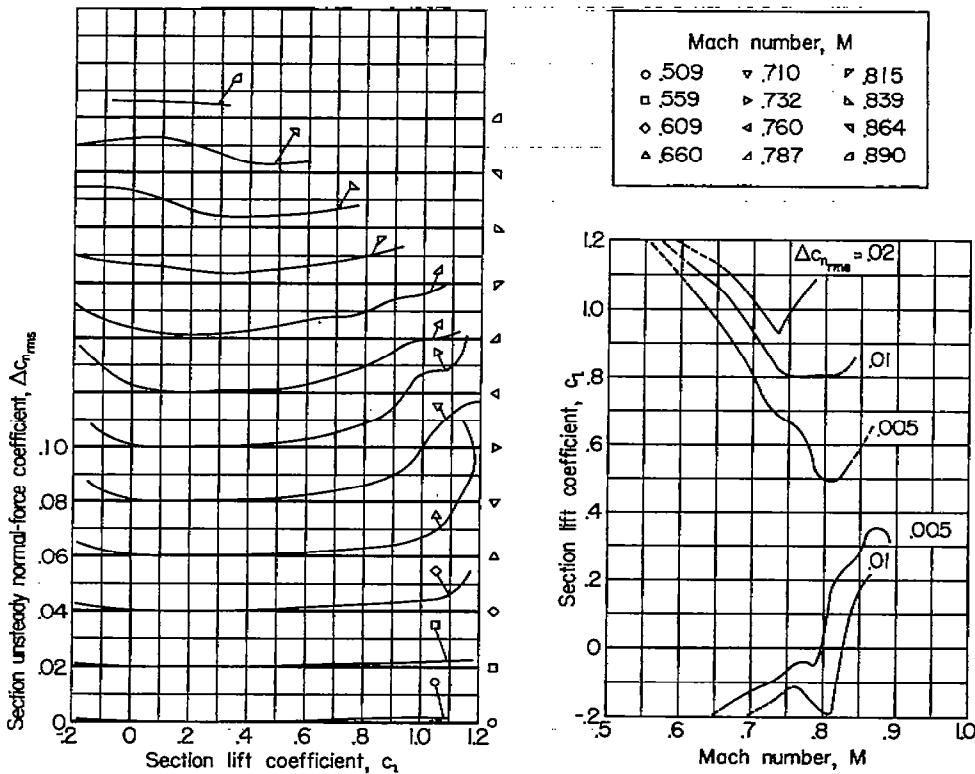
(b) Variation of section unsteady normal-force coefficient with section lift coefficient for various Mach numbers.

(c) Section unsteady normal-force coefficient contours.

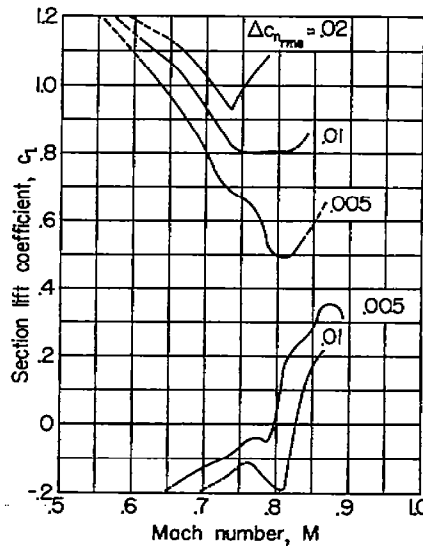
Figure 21.- Lift coefficient and unsteady normal-force characteristics of the NACA 65-412 profile.



(a) Variation of section lift coefficient with section angle of attack for various Mach numbers.

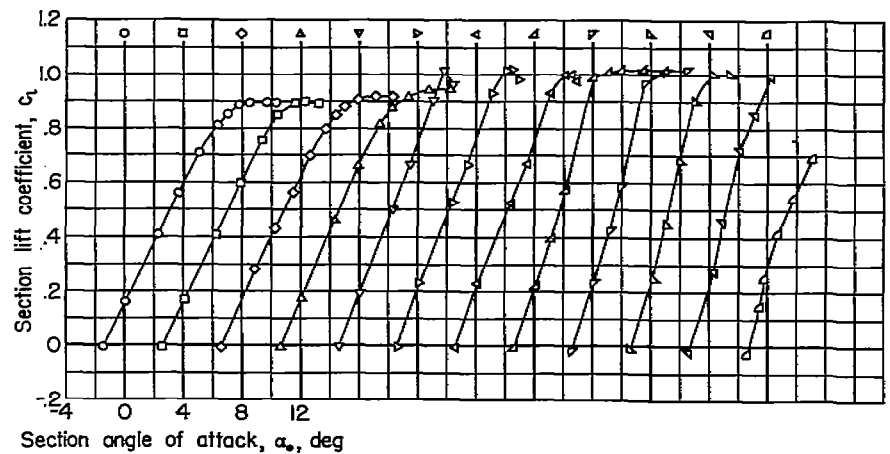


(b) Variation of section unsteady normal-force coefficient with section lift coefficient for various Mach numbers.

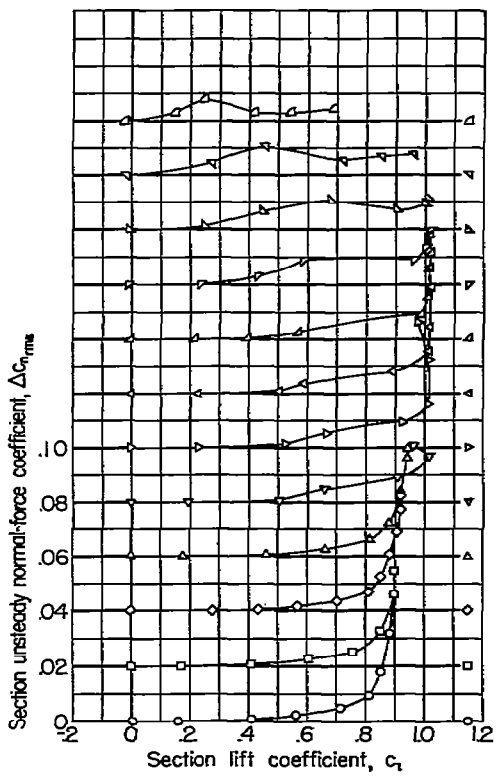


(c) Section unsteady normal-force coefficient contours.

Figure 22.- Lift coefficient and unsteady normal-force characteristics of the NACA 65-612 profile.

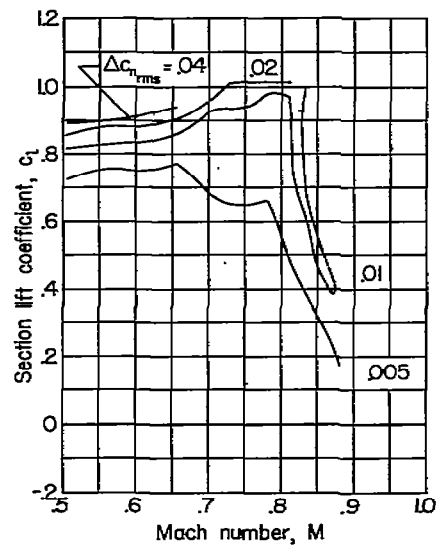


(a) Variation of section lift coefficient with section angle of attack for various Mach numbers.



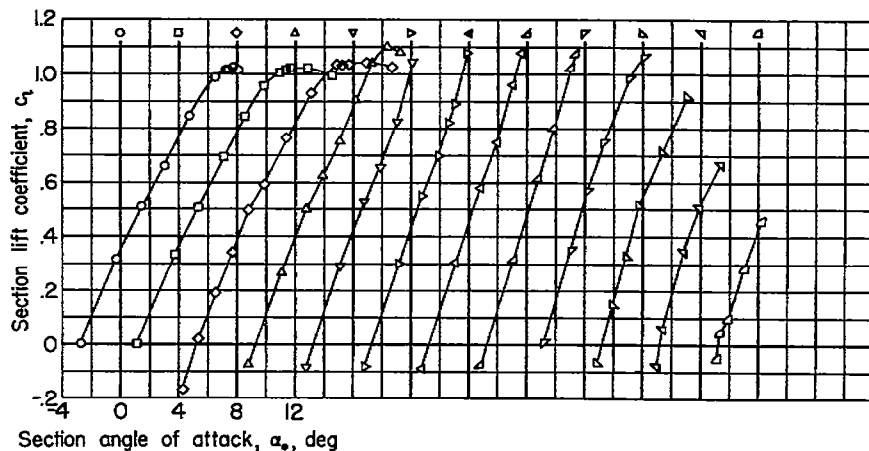
(b) Variation of section unsteady normal-force coefficient with section lift coefficient for various Mach numbers.

Mach number, M		
○ .505	▽ .703	▷ 810
□ .554	▷ .728	▷ 835
◇ .605	◀ .756	◀ 859
△ .655	△ .782	△ 879

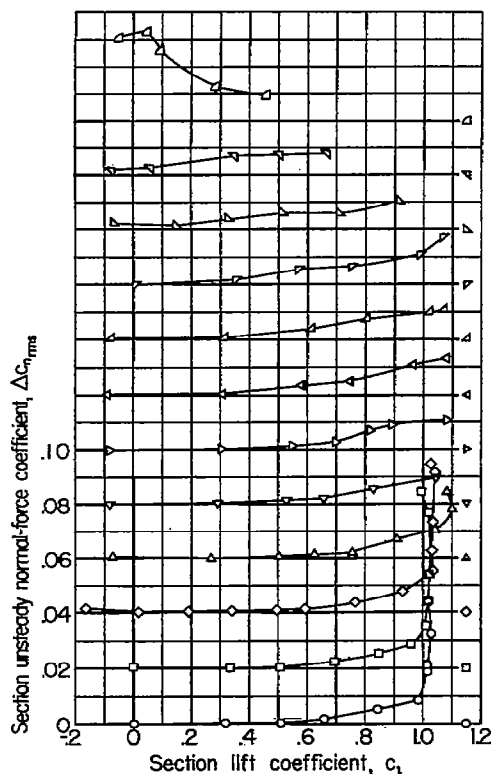


(c) Section unsteady normal-force coefficient contours.

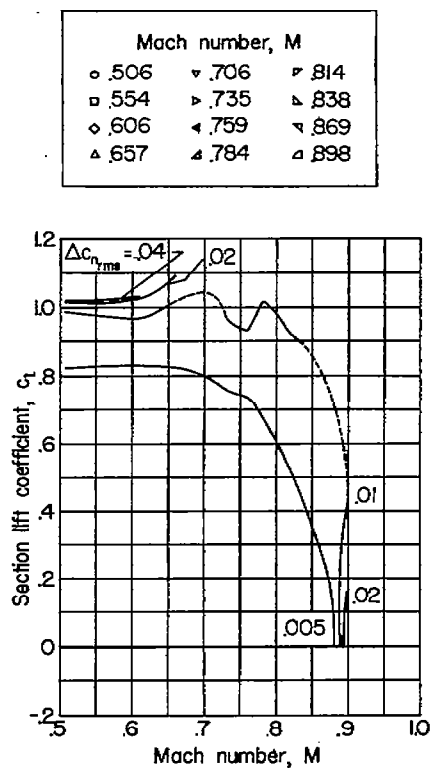
Figure 23.- Lift coefficient and unsteady normal-force characteristics of the NACA 65-204 profile.



(a) Variation of section lift coefficient with section angle of attack for various Mach numbers.

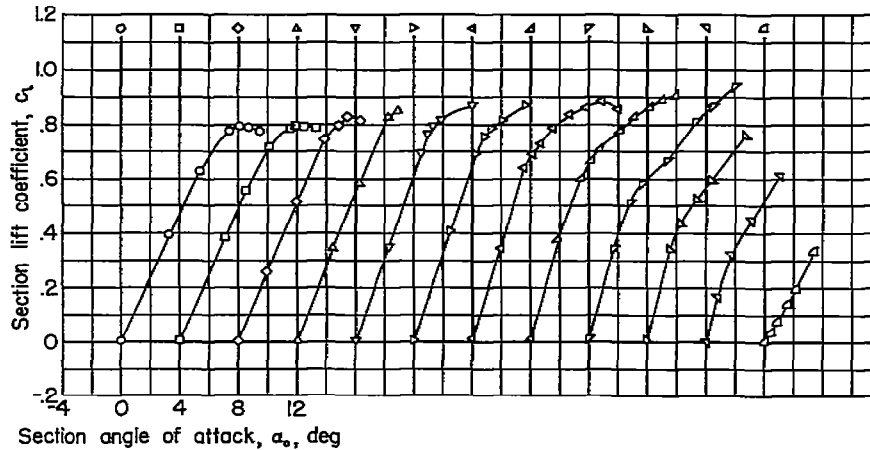


(b) Variation of section unsteady normal-force coefficient with section lift coefficient for various Mach numbers.

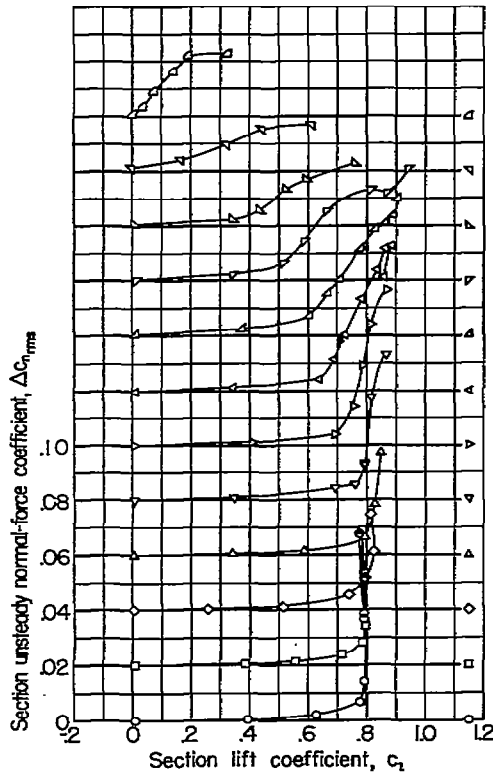


(c) Section unsteady normal-force coefficient contours.

Figure 24.- Lift coefficient and unsteady normal-force characteristics of the NACA 65-404 profile.

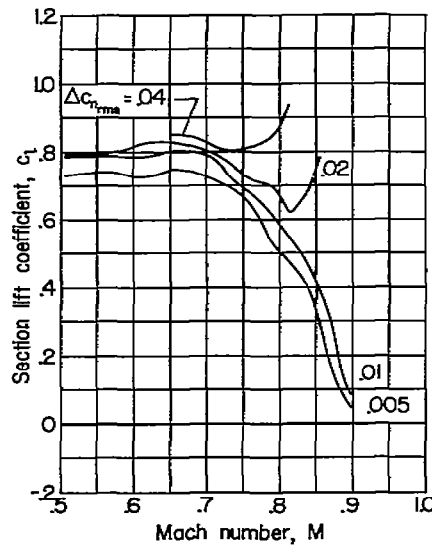


(a) Variation of section lift coefficient with section angle of attack for various Mach numbers.



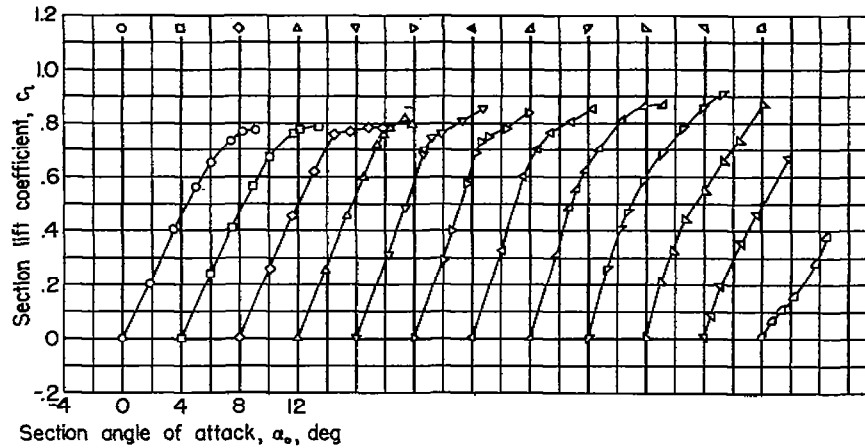
(b) Variation of section unsteady normal-force coefficient with section lift coefficient for various Mach numbers.

Mach number, M		
○ .505	▽ .705	▽ .814
□ .555	▷ .731	▷ .837
◇ .608	◁ .760	◁ .867
△ .656	△ .788	△ .899

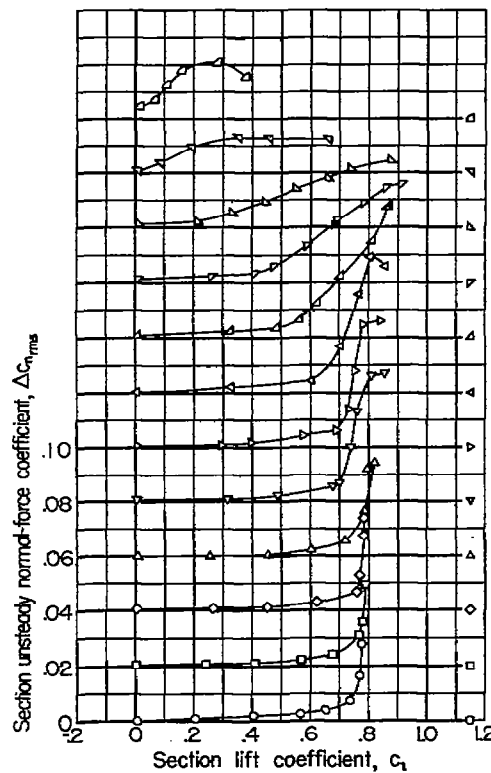


(c) Section unsteady normal-force coefficient contours.

Figure 25.- Lift coefficient and unsteady normal-force characteristics of the NACA 63-010 profile.

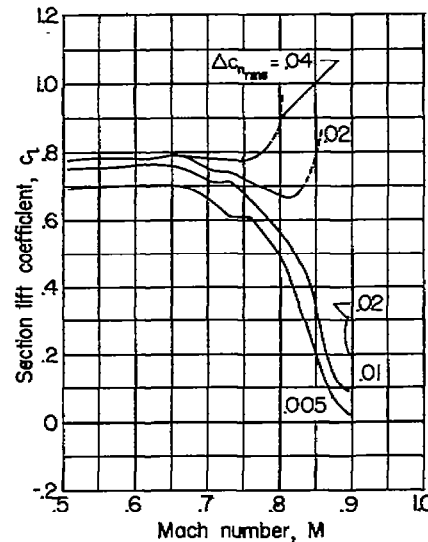


(a) Variation of section lift coefficient with section angle of attack for various Mach numbers.



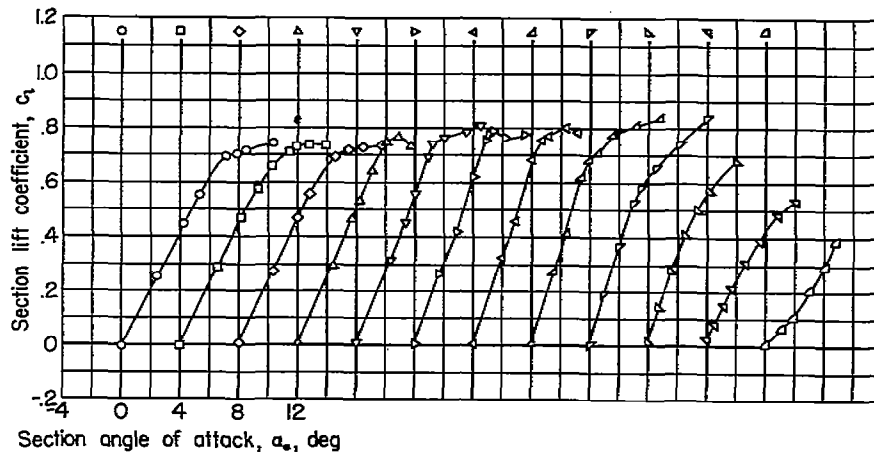
(b) Variation of section unsteady normal-force coefficient with section lift coefficient for various Mach numbers

Mach number, M		
○ .506	▽ .705	▽ .811
□ .555	▷ .733	▷ .837
◇ .604	◄ .759	◄ .866
△ .657	△ .788	△ .897

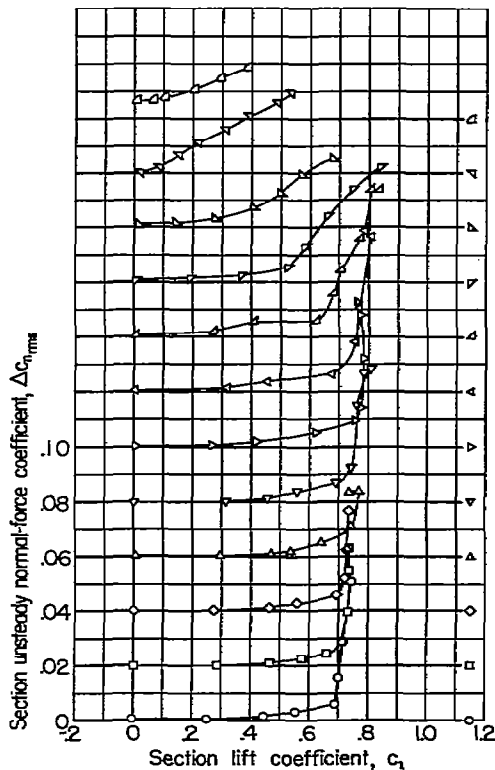


(c) Section unsteady normal-force coefficient contours.

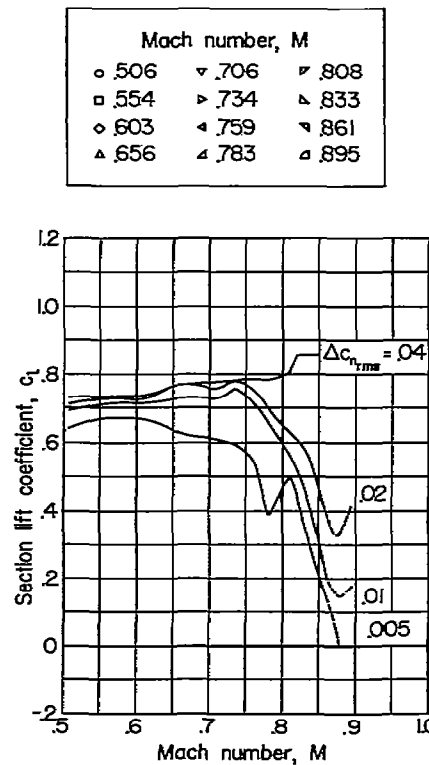
Figure 26.- Lift coefficient and unsteady normal-force characteristics of the NACA 64-010 profile.



(a) Variation of section lift coefficient with section angle of attack for various Mach numbers.

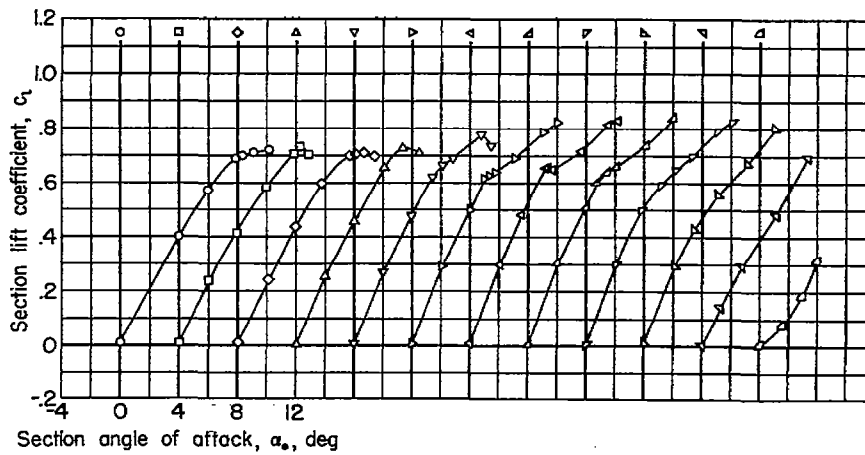


(b) Variation of section unsteady normal-force coefficient with section lift coefficient for various Mach numbers.

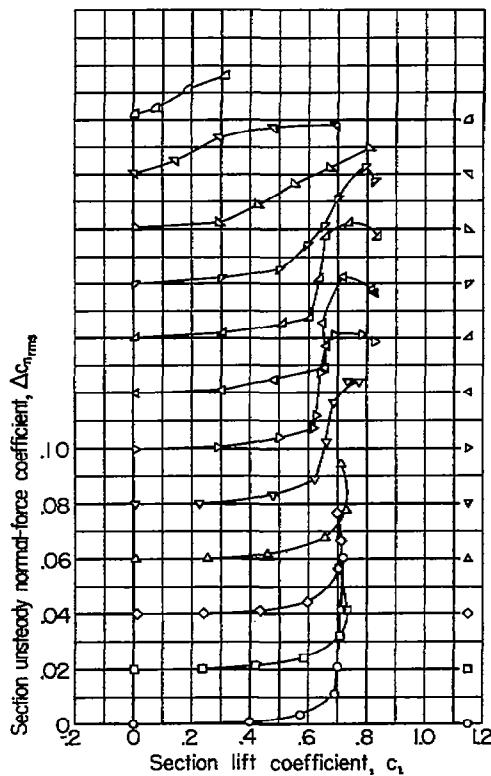


(c) Section unsteady normal-force coefficient contours.

Figure 27.- Lift coefficient and unsteady normal-force characteristics of the NACA 66-010 profile.

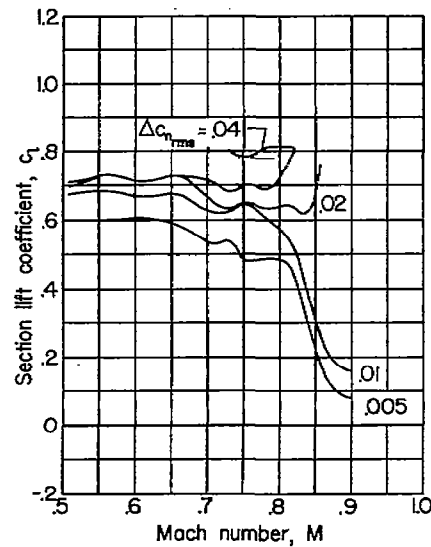


(a) Variation of section lift coefficient with section angle of attack for various Mach numbers.



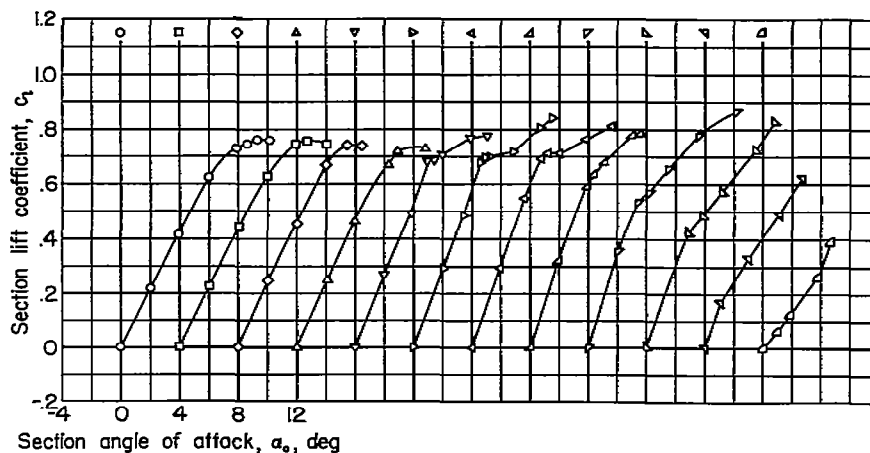
(b) Variation of section unsteady normal-force coefficient with section lift coefficient for various Mach numbers.

Mach number, M		
○ .508	▽ .704	▽ .810
□ .556	▷ .731	△ .832
◇ .605	◀ .750	▽ .862
△ .654	△ .779	△ .899

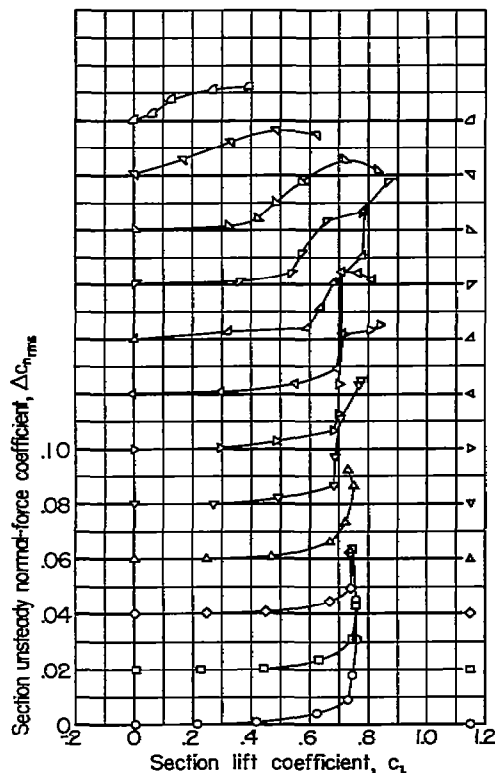


(c) Section unsteady normal-force coefficient contours.

Figure 28.- Lift coefficient and unsteady normal-force characteristics of the NACA 0010-0.27-40/1.051 profile.

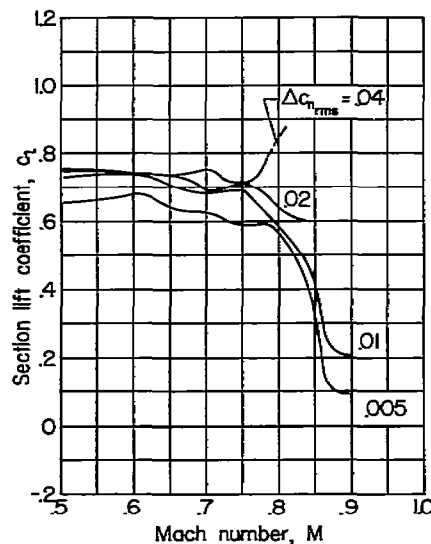


(a) Variation of section lift coefficient with section angle of attack for various Mach numbers.



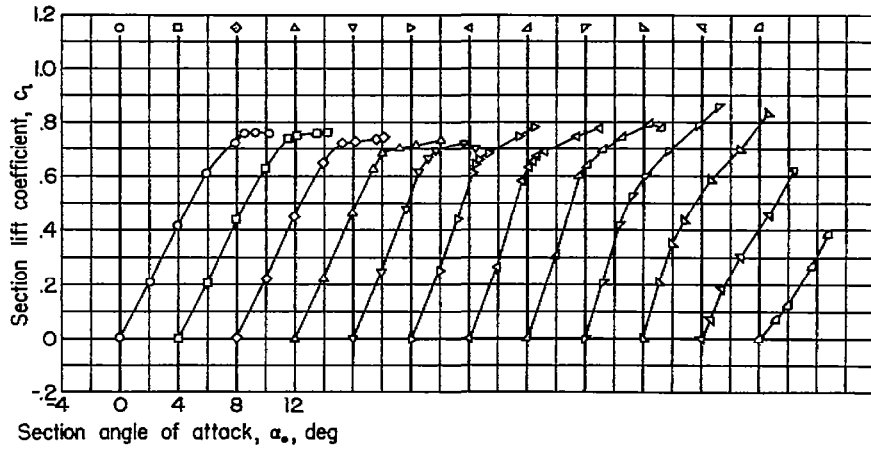
(b) Variation of section unsteady normal-force coefficient with section lift coefficient for various Mach numbers.

Mach number, M		
○ .503	▽ .704	▽ .810
□ .555	▷ .730	▷ .838
◇ .607	◁ .755	◁ .864
△ .655	△ .785	△ .896

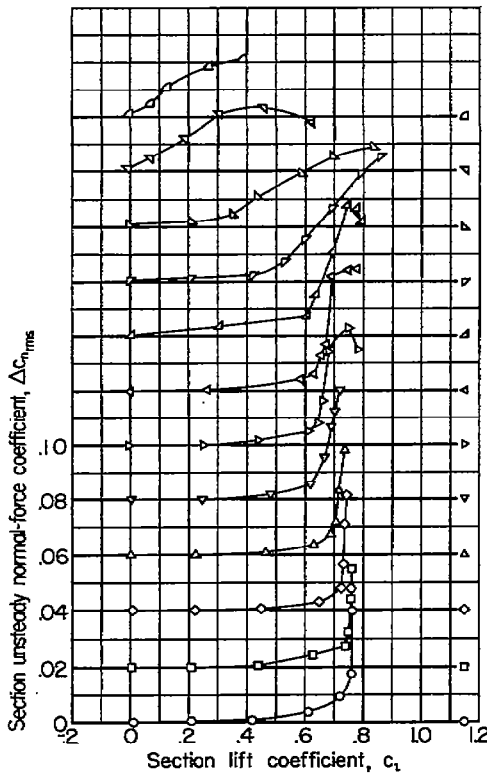


(c) Section unsteady normal-force coefficient contours.

Figure 29.- Lift coefficient and unsteady normal-force characteristics of the NACA 0010-0.70-40/1.051 profile.

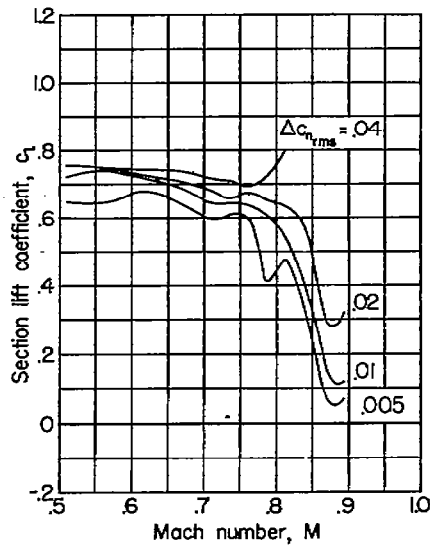


(a) Variation of section lift coefficient with section angle of attack for various Mach numbers.



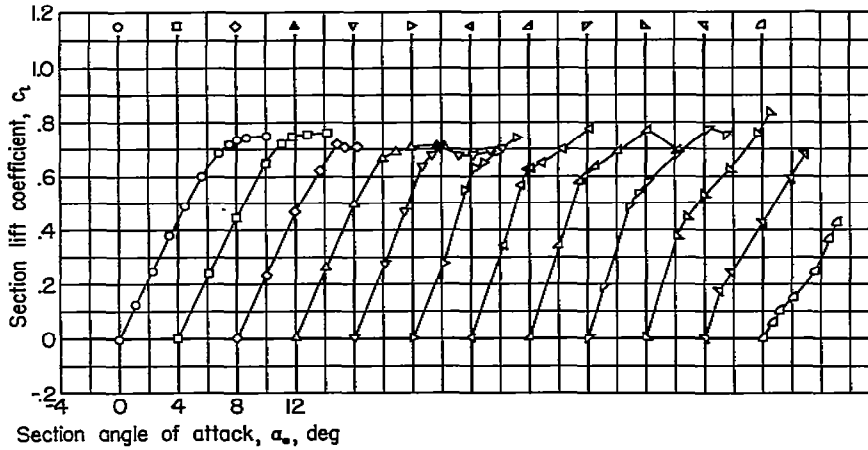
(b) Variation of section unsteady normal-force coefficient with section lift coefficient for various Mach numbers.

Mach number, M		
○ .510	▽ .707	▾ .812
□ .557	▷ .734	▴ .838
◇ .606	◁ .757	▽ .870
△ .657	▲ .785	▲ .896

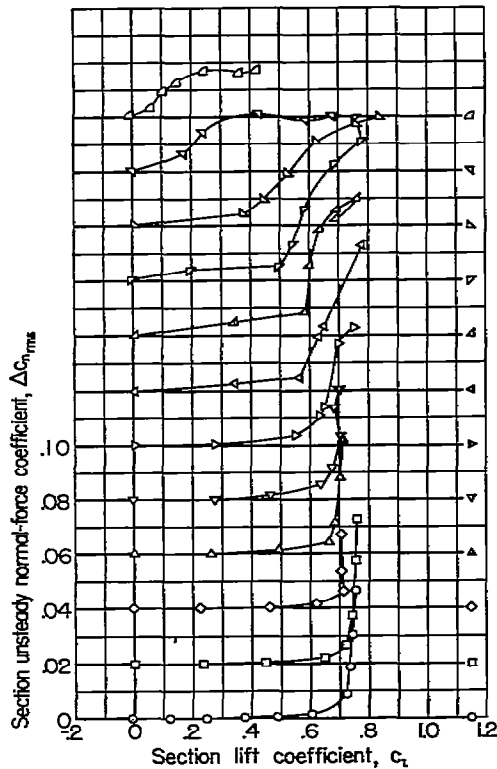


(c) Section unsteady normal-force coefficient contours.

Figure 30.- Lift coefficient and unsteady normal-force characteristics of the NACA 0010-1.10-40/1.051 profile.

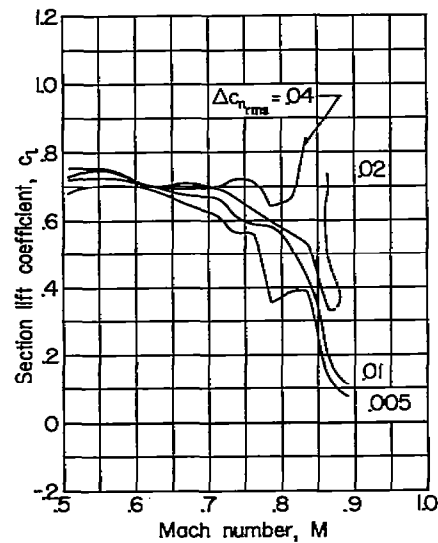


(a) Variation of section lift coefficient with section angle of attack for various Mach numbers.



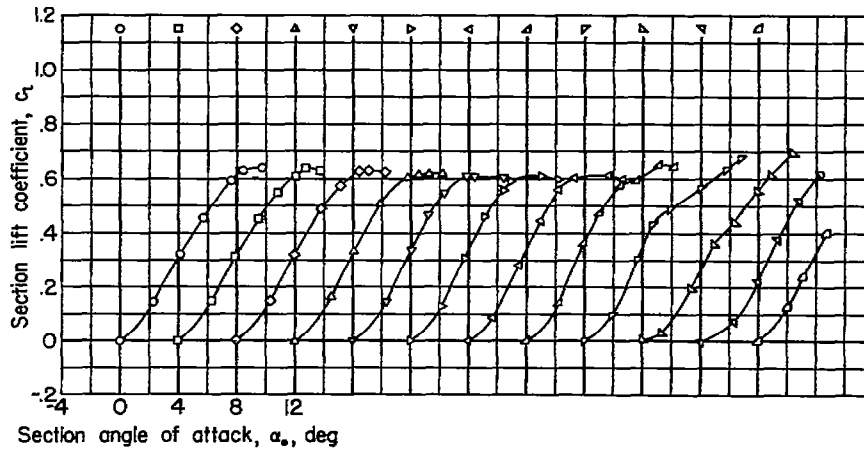
(b) Variation of section unsteady normal-force coefficient with section lift coefficient for various Mach numbers.

Mach number, M		
○ .507	▽ .708	▽ 812
□ .557	▷ .734	▷ 836
◇ .607	◁ .761	◁ 864
△ .658	△ .787	△ 891

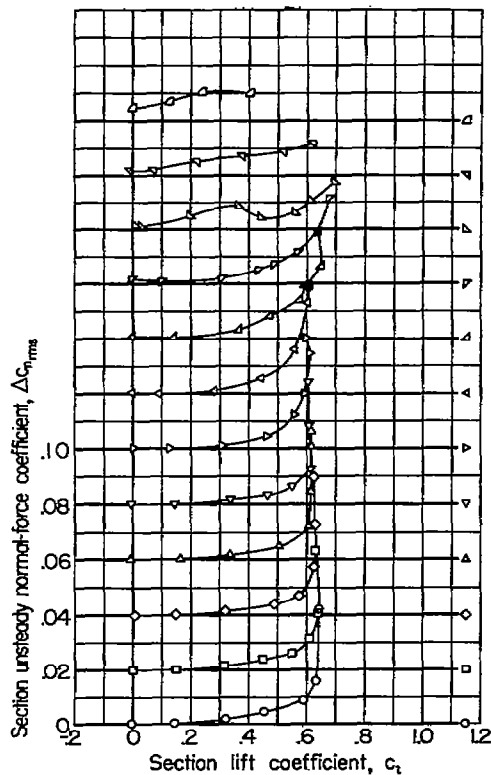


(c) Section unsteady normal-force coefficient contours.

Figure 31.- Lift coefficient and unsteady normal-force characteristics of the NACA 0010-1.50-40/1.051 profile.

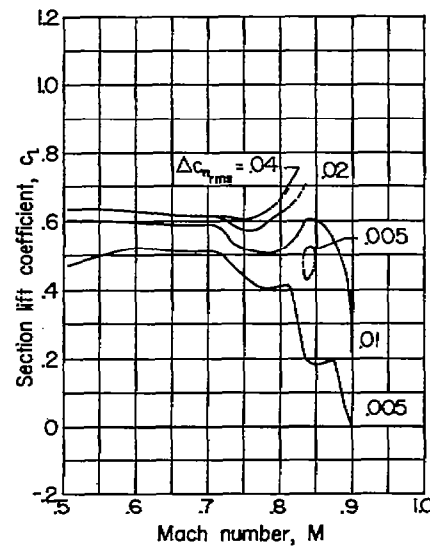


(a) Variation of section lift coefficient with section angle of attack for various Mach numbers.



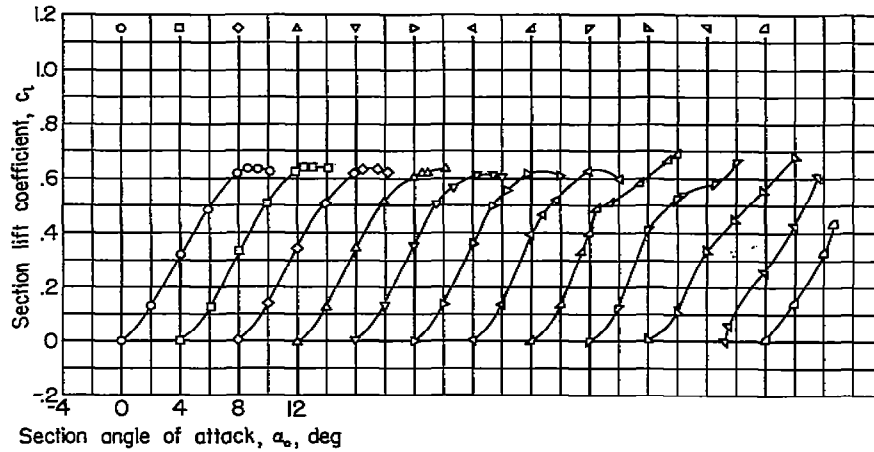
(b) Variation of section unsteady normal-force coefficient with section lift coefficient for various Mach numbers.

Mach number, M		
○ .509	▽ .708	◻ .812
□ .559	▷ .732	◂ .837
◇ .606	◄ .760	◃ .868
△ .658	◁ .785	▹ .899

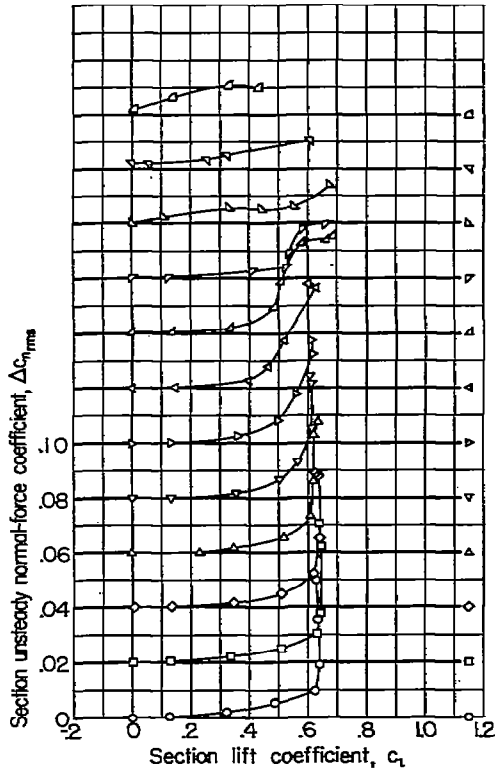


(c) Section unsteady normal-force coefficient contours.

Figure 32.- Lift coefficient and unsteady normal-force characteristics of the 10-percent circular-arc profile with zero leading-edge radius.

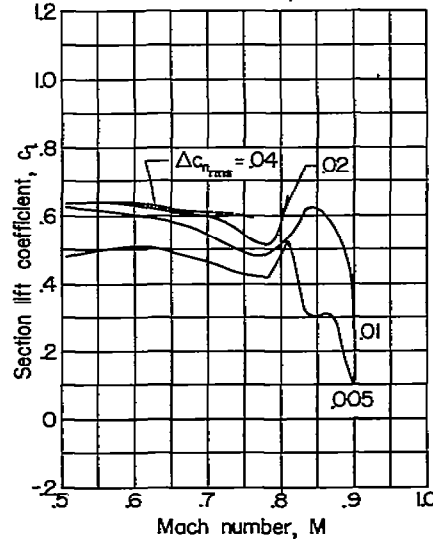


(a) Variation of section lift coefficient with section angle of attack for various Mach numbers.



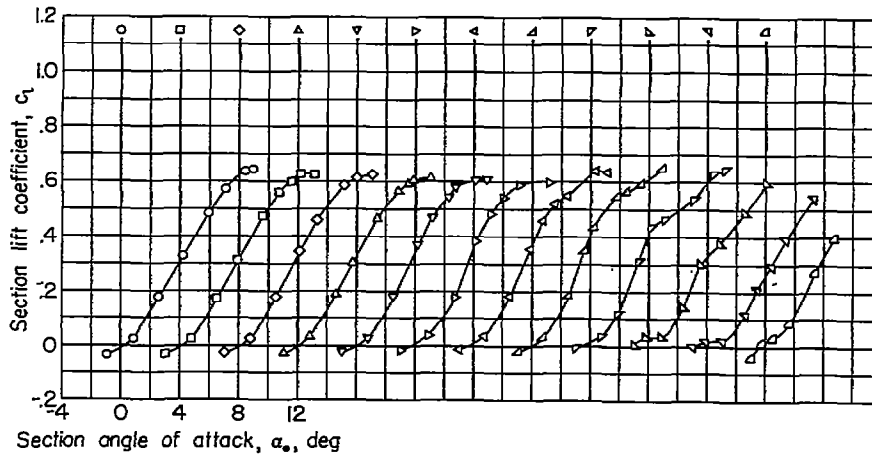
(b) Variation of section unsteady normal-force coefficient with section lift coefficient for various Mach numbers.

Mach number, M		
○ .509	▽ .706	▽ .811
□ .555	▷ .733	▷ .835
◇ .607	◁ .760	◁ .864
△ .657	▲ .783	▲ .898

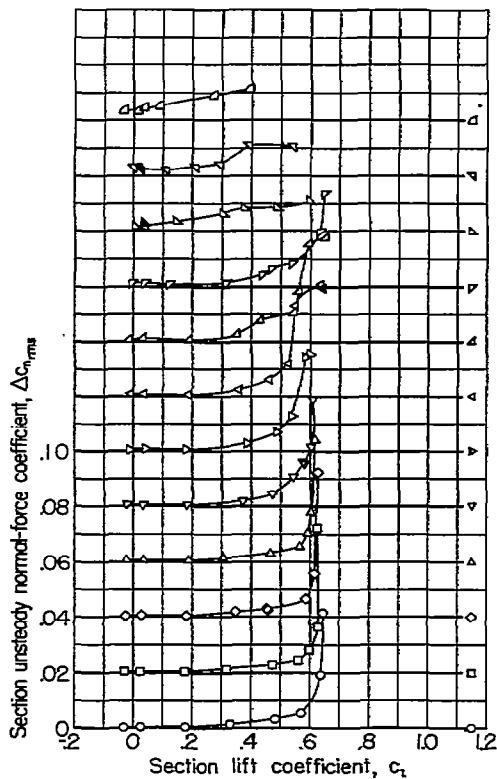


(c) Section unsteady normal-force coefficient contours.

Figure 33.- Lift coefficient and unsteady normal-force characteristics of the 10-percent circular-arc profile with 0.27 leading-edge radius.

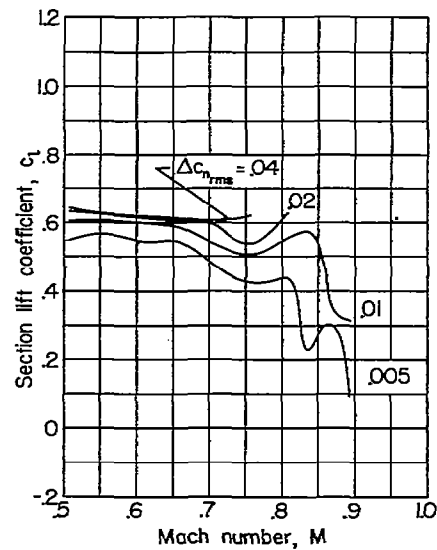


(b) Variation of section lift coefficient with section angle of attack for various Mach numbers.



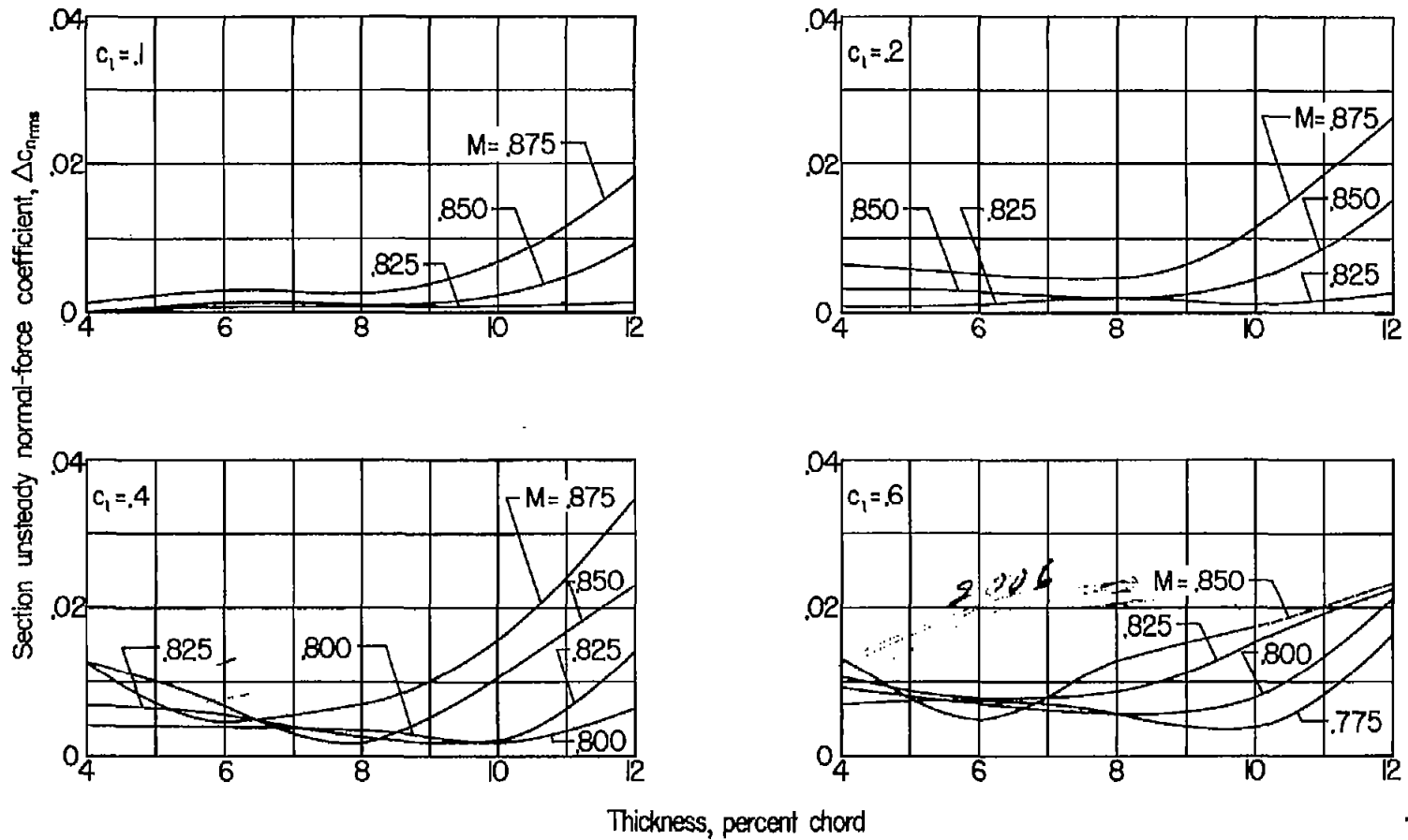
(b) Variation of section unsteady normal-force coefficient with section lift coefficient for various Mach numbers.

Mach number, M		
○ .508	▽ .704	▽ .808
□ .554	▷ .731	▷ .834
◇ .602	◁ .757	◁ .865
△ .655	△ .781	△ .893



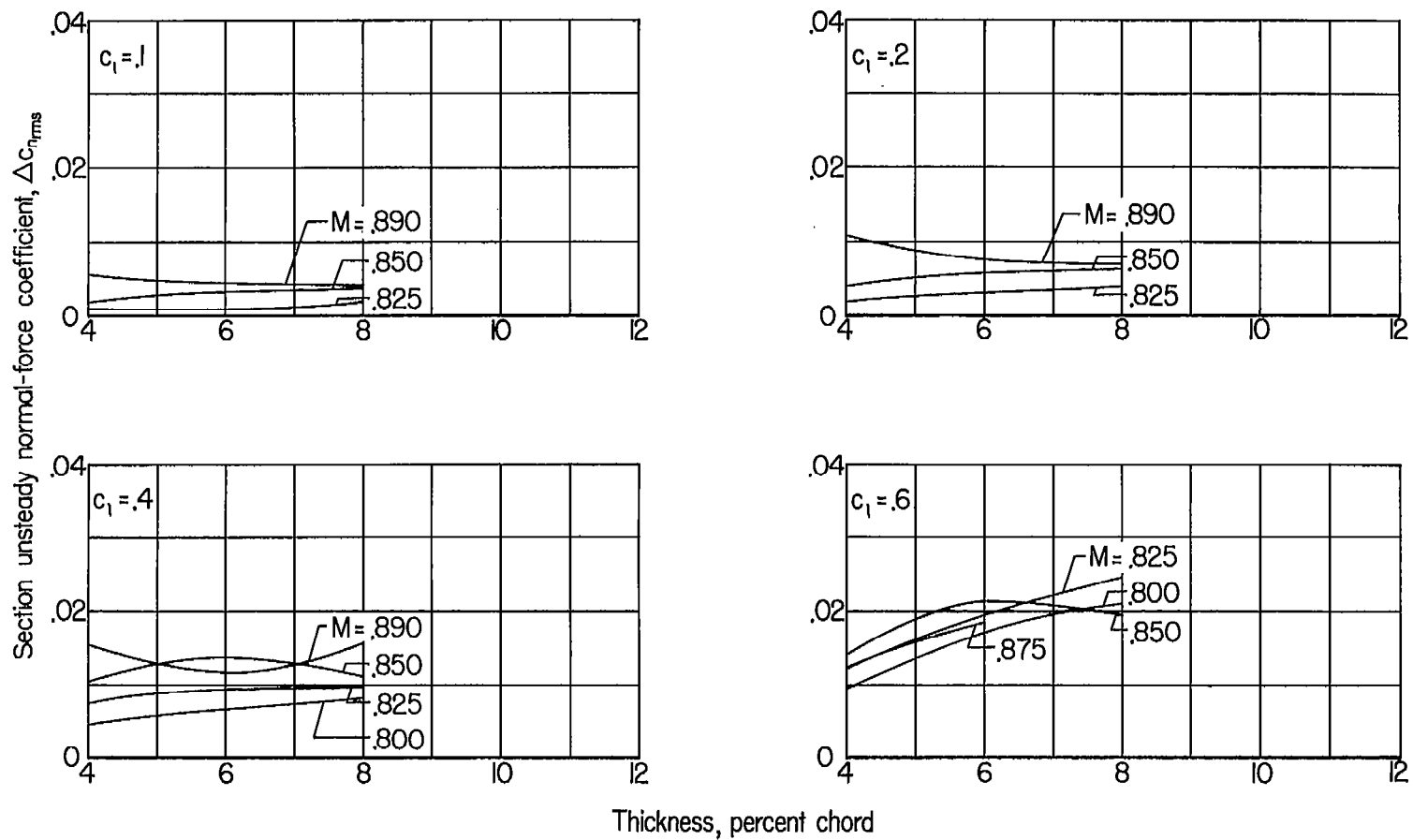
(c) Section unsteady normal-force coefficient contours.

Figure 34.- Lift coefficient and unsteady normal-force characteristics of the 10-percent circular-arc profile with 0.70 leading-edge radius.



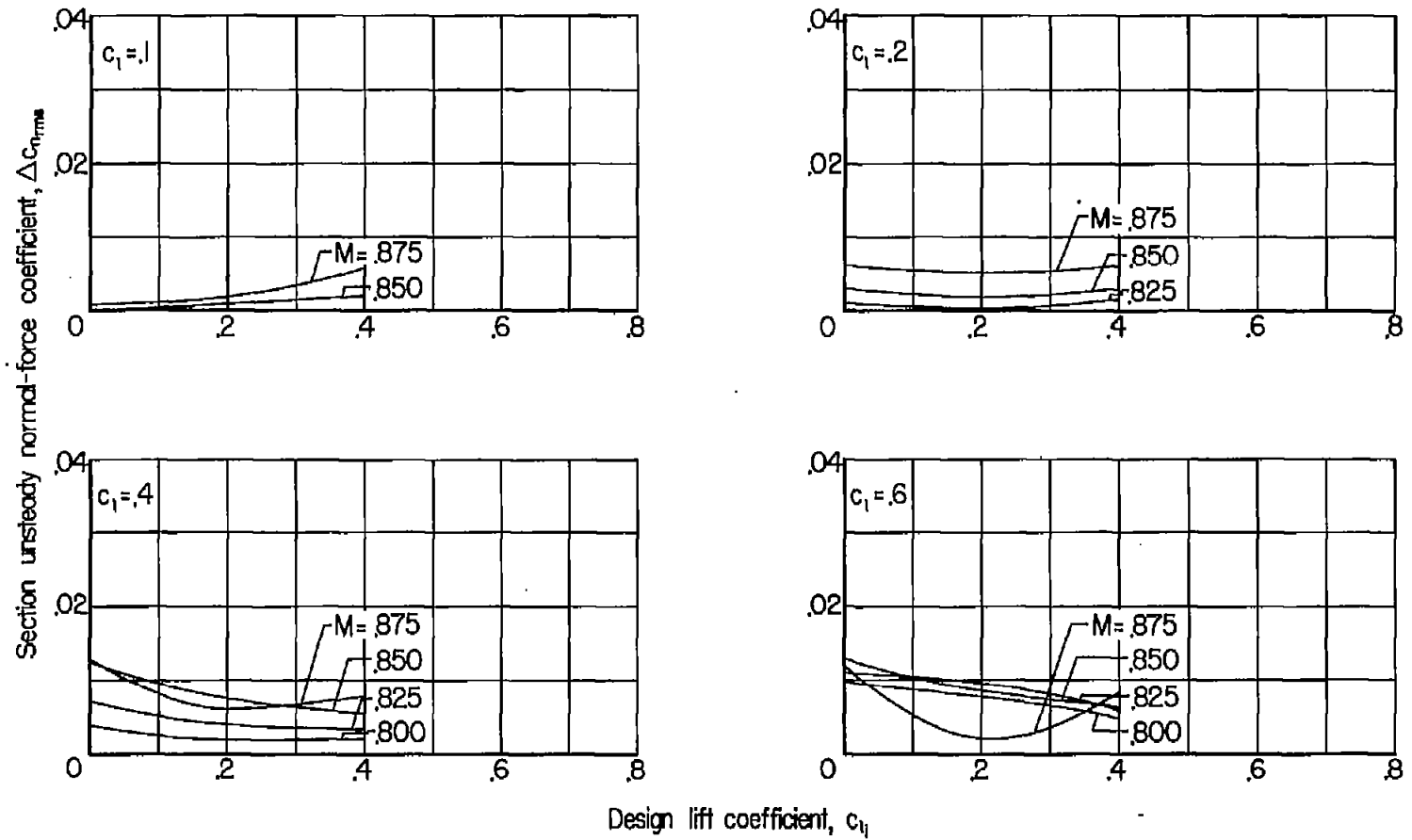
(a) NACA 65-series symmetrical profiles.

Figure 35.- Variation of unsteady normal-force coefficient with maximum thickness-chord ratio.



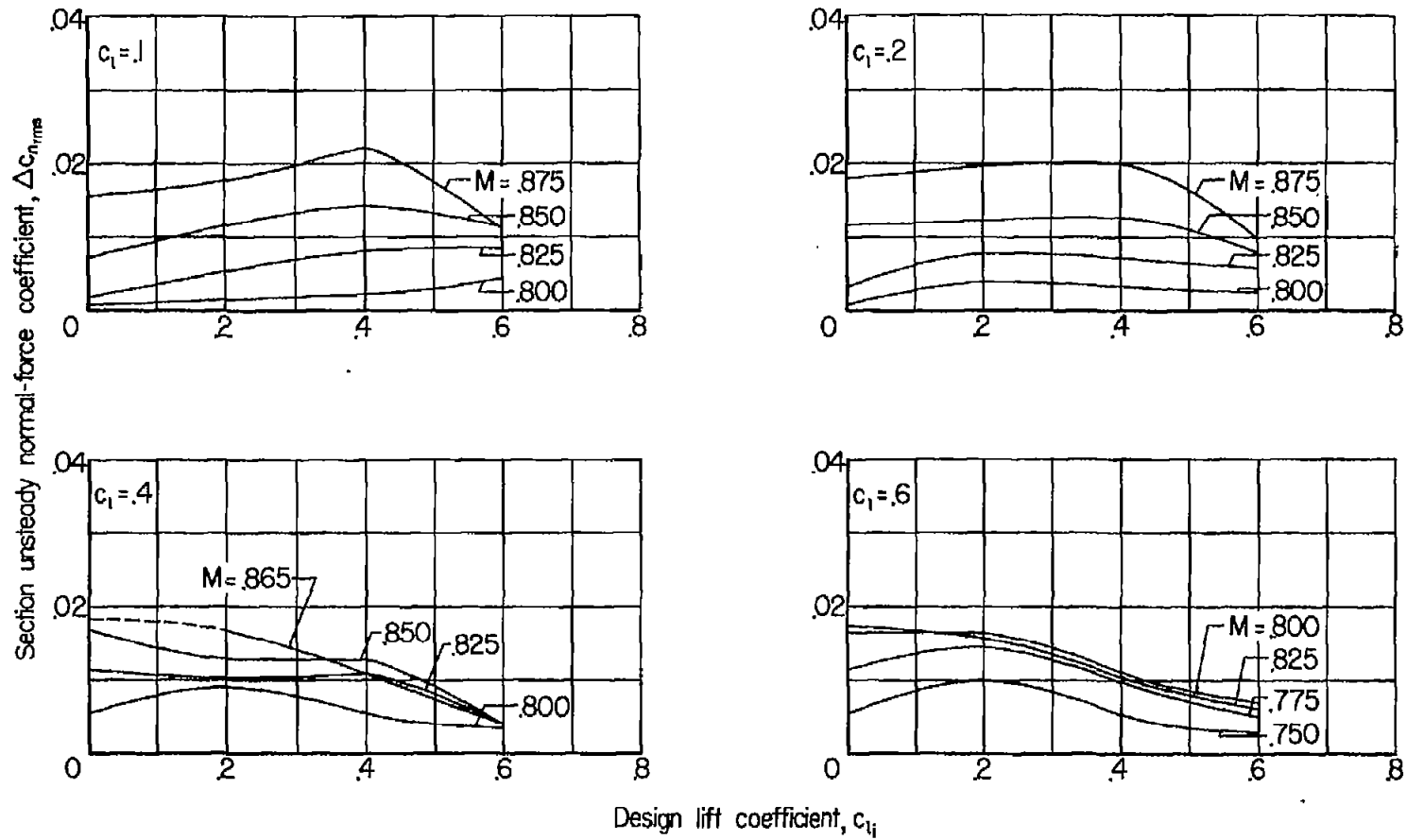
(b) NACA 2-series symmetrical profiles.

Figure 35.- Concluded.



(a) NACA 65-series, 12-percent-thick profiles.

Figure 36.- Variation of unsteady normal-force coefficient with design lift coefficient.



(b) NACA 65-series, 4-percent-thick profiles.

Figure 36.- Concluded.

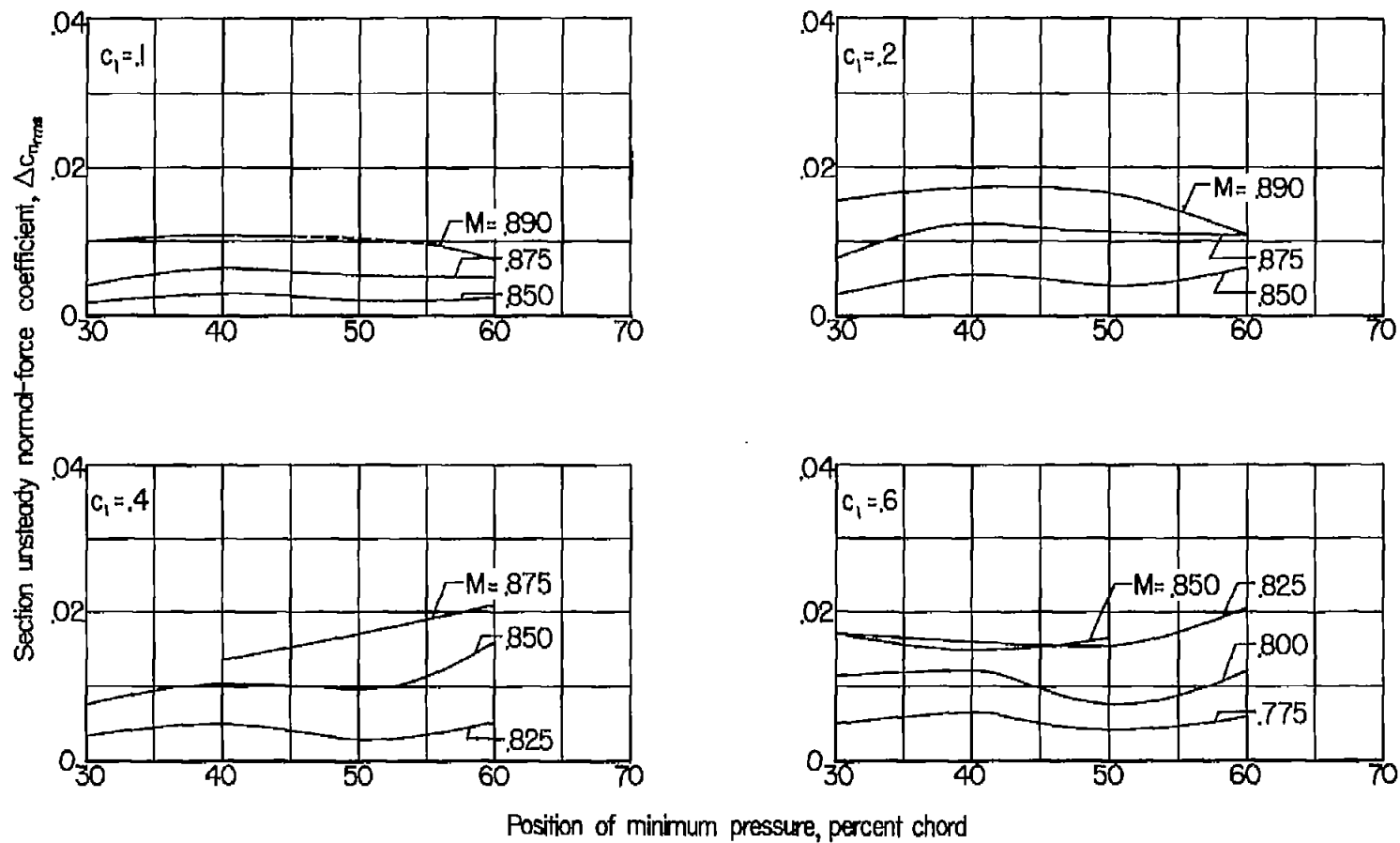
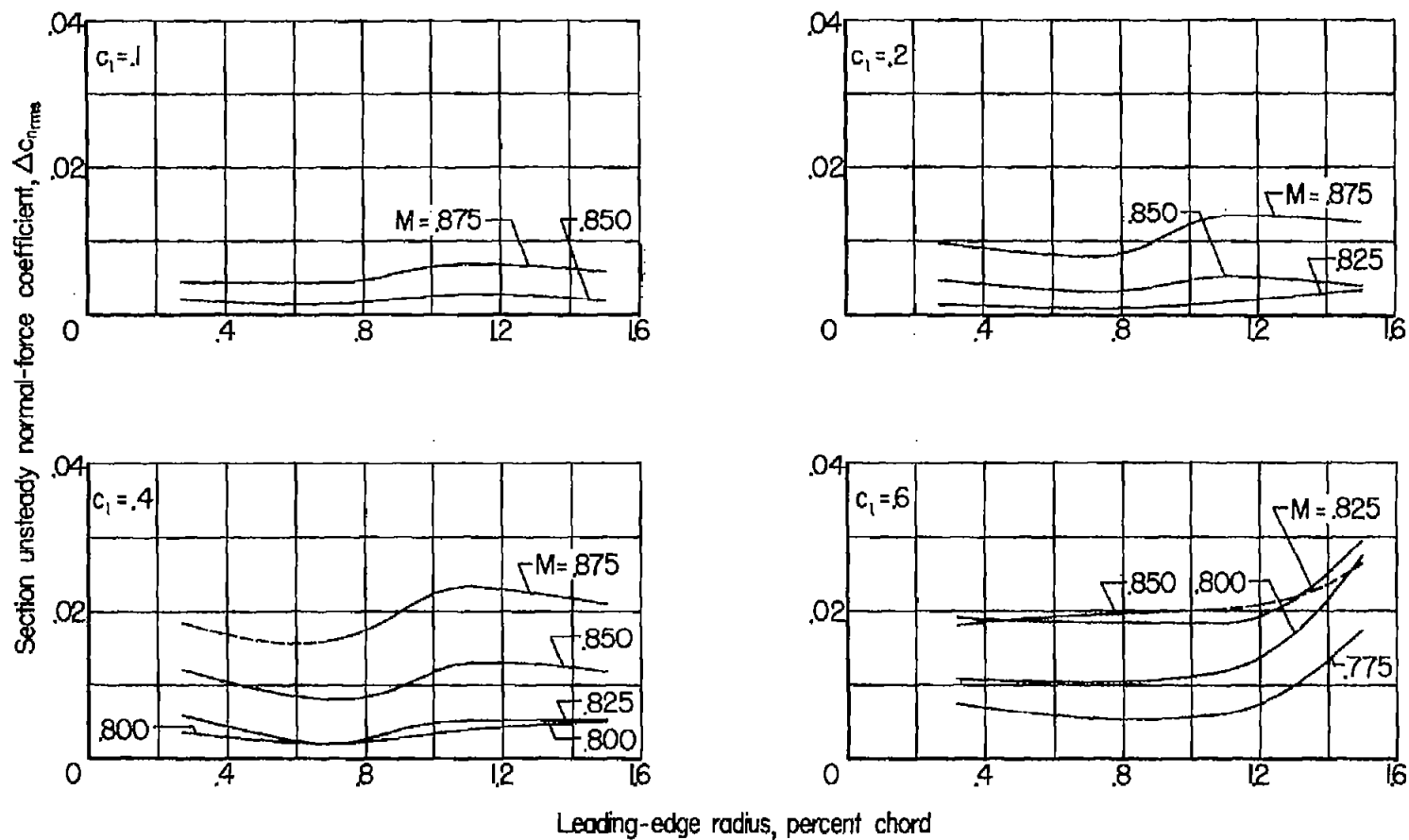
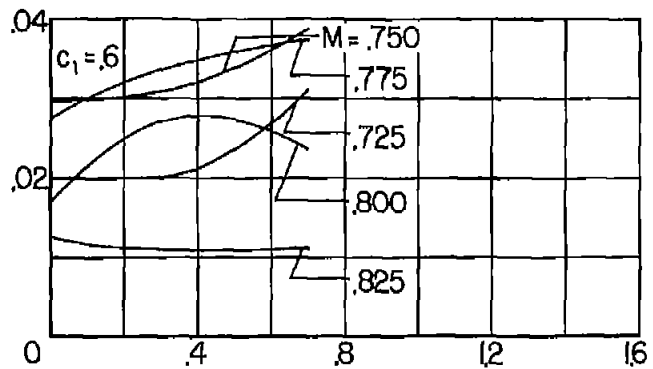
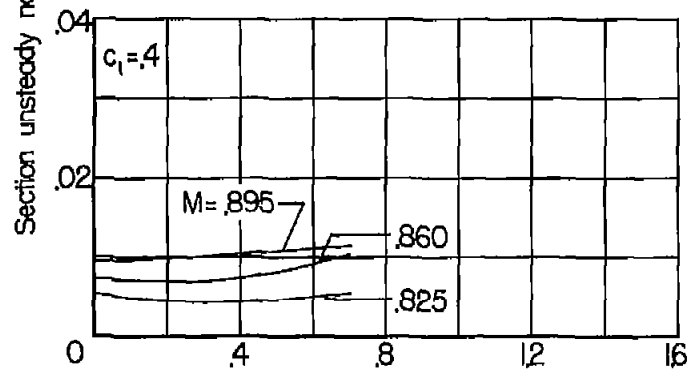
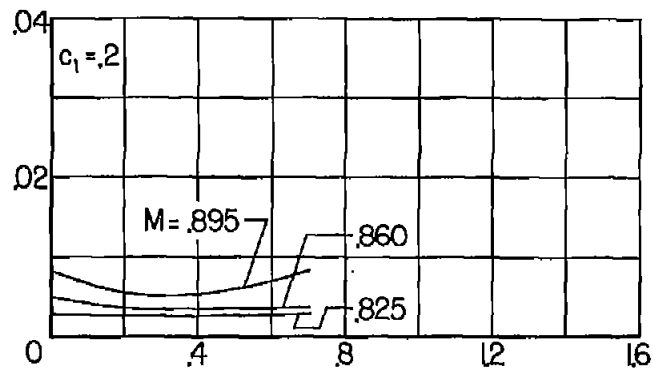
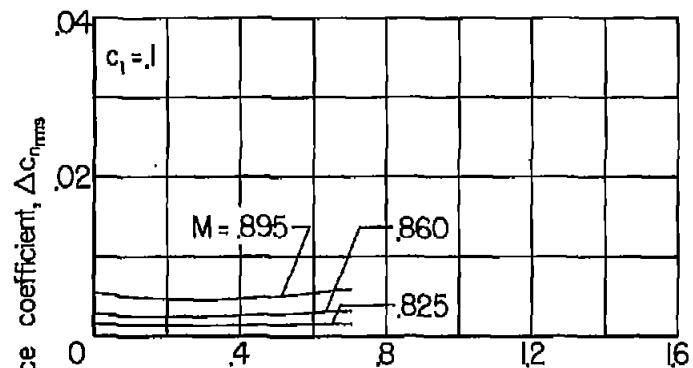


Figure 37.- Variation of unsteady normal-force coefficient with position of minimum pressure; NACA 6-series, 10-percent-thick symmetrical profiles.



(a) NACA 0010-series profiles.

Figure 38.- Variation of unsteady normal-force coefficient with leading-edge radius.



Leading-edge radius, percent chord

(b) 10-percent-thick circular-arc profile.

Figure 38.- Concluded.

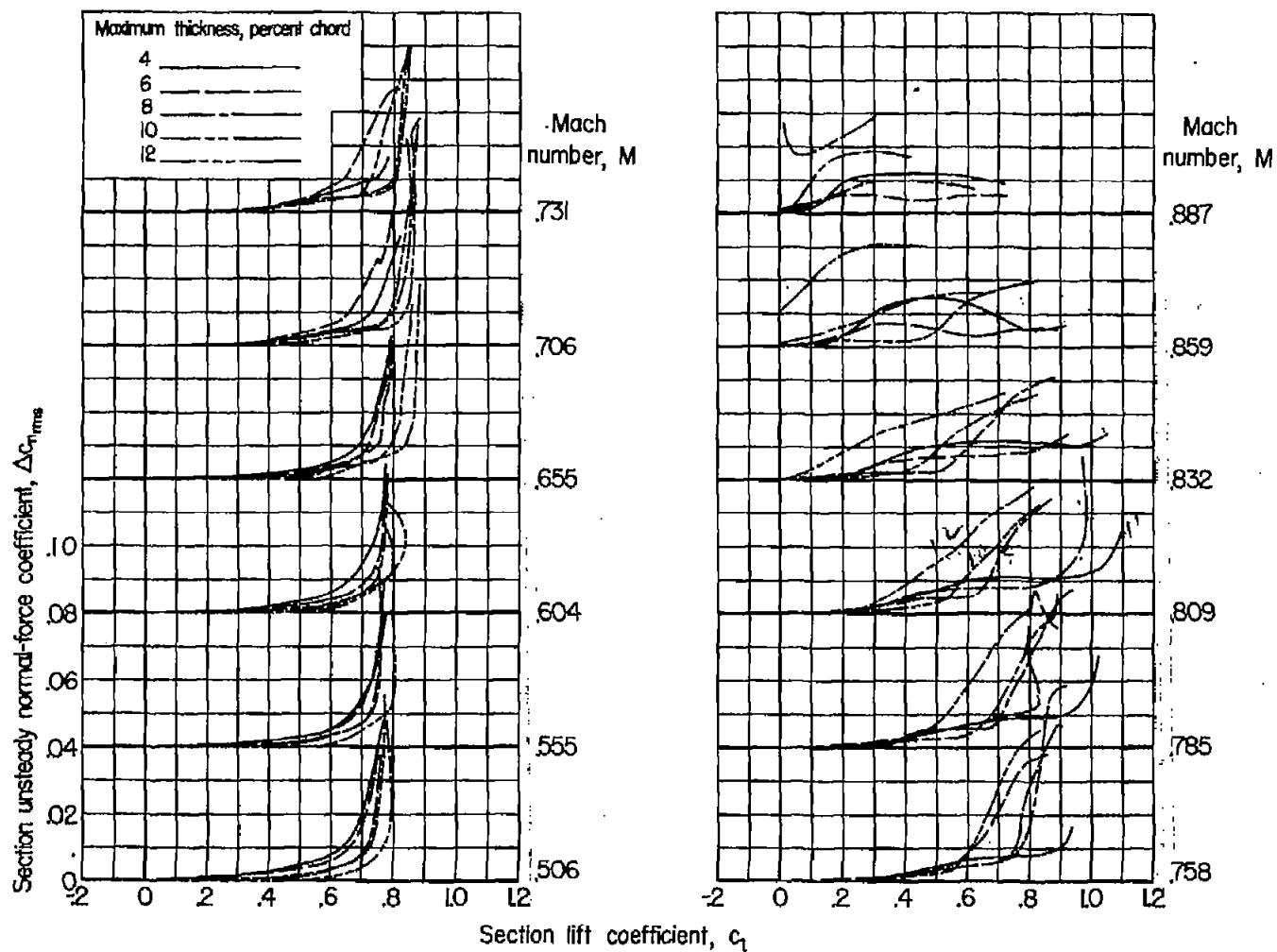


Figure 39.- Effect of maximum thickness on the variation of section unsteady normal-force coefficient with section lift coefficient; NACA 65-series profiles.

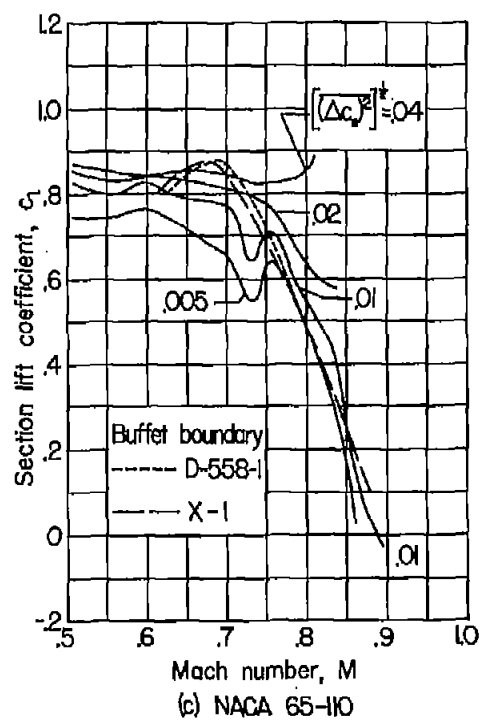
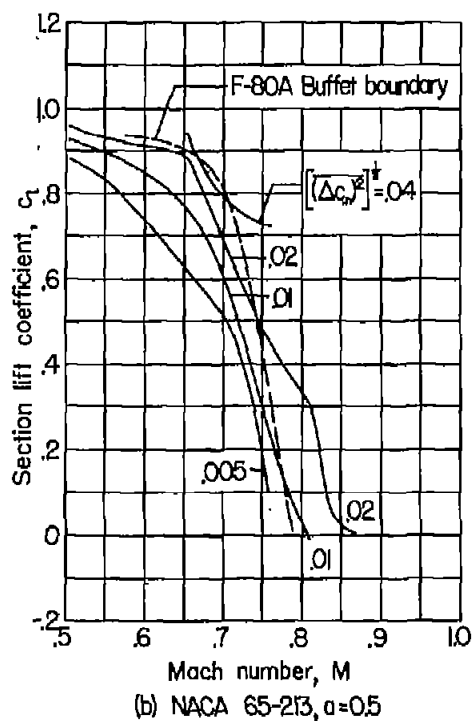
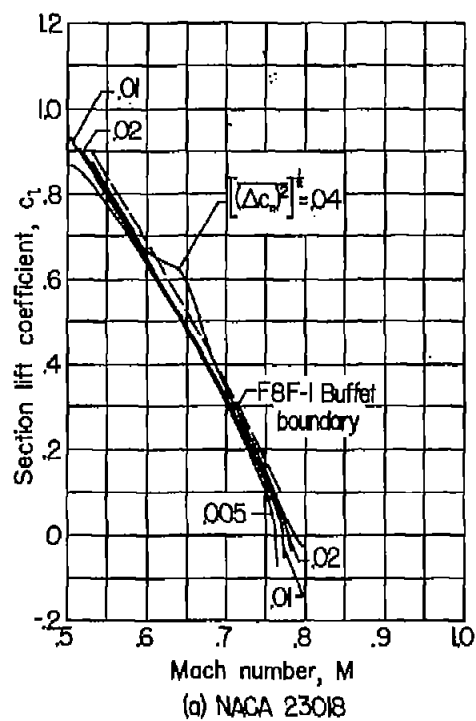
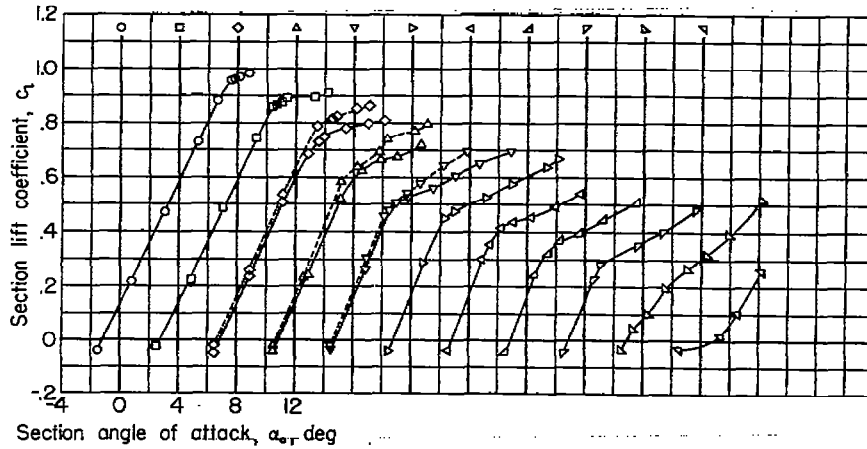
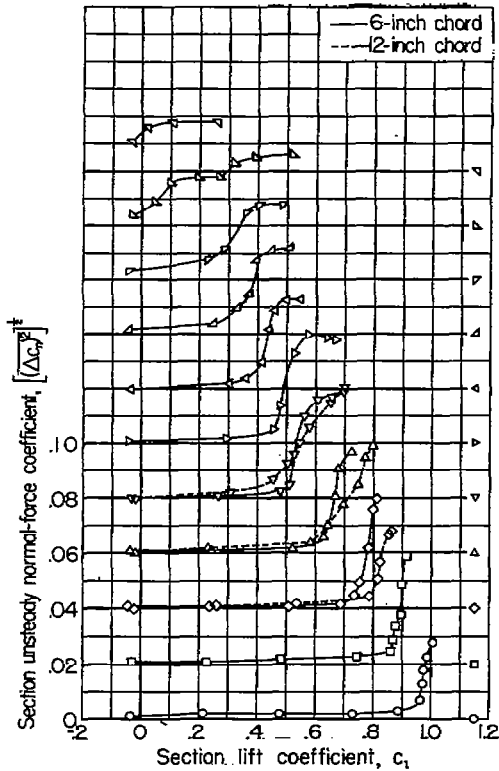


Figure 40.- Comparison of unsteady normal-force contours with flight-determined buffet boundaries.

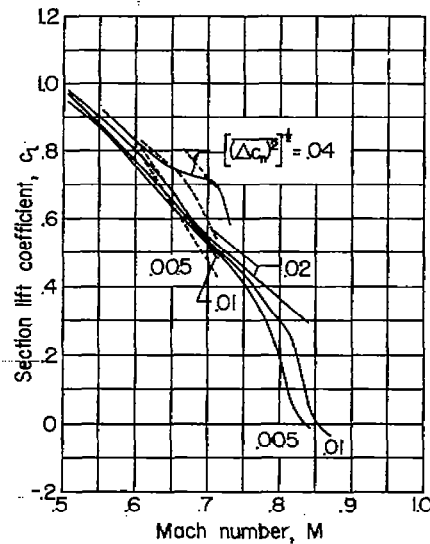


(a) Variation of section lift coefficient with section angle of attack for various Mach numbers.



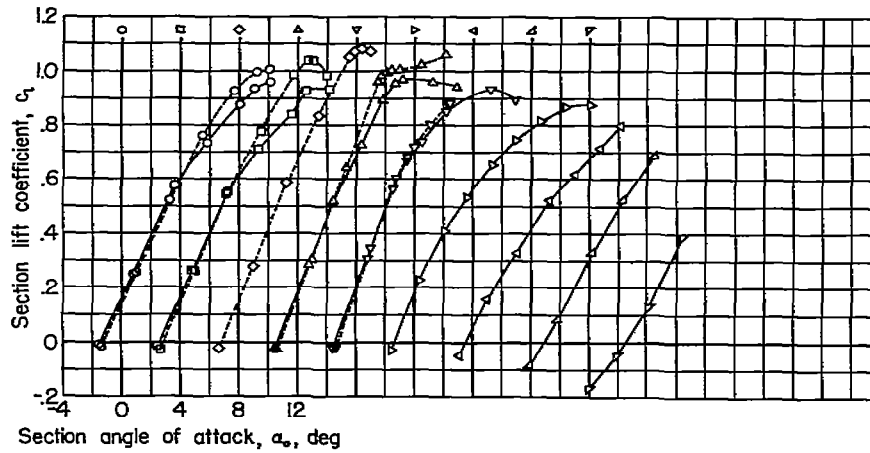
(b) Variation of section unsteady normal-force coefficient with section lift coefficient for various Mach numbers.

Mach number, M	
○ 507	▽ 707-711
□ 556	▷ 733
◇ 608-607	◁ 760
△ 655-662	▽ 871
	△ 785

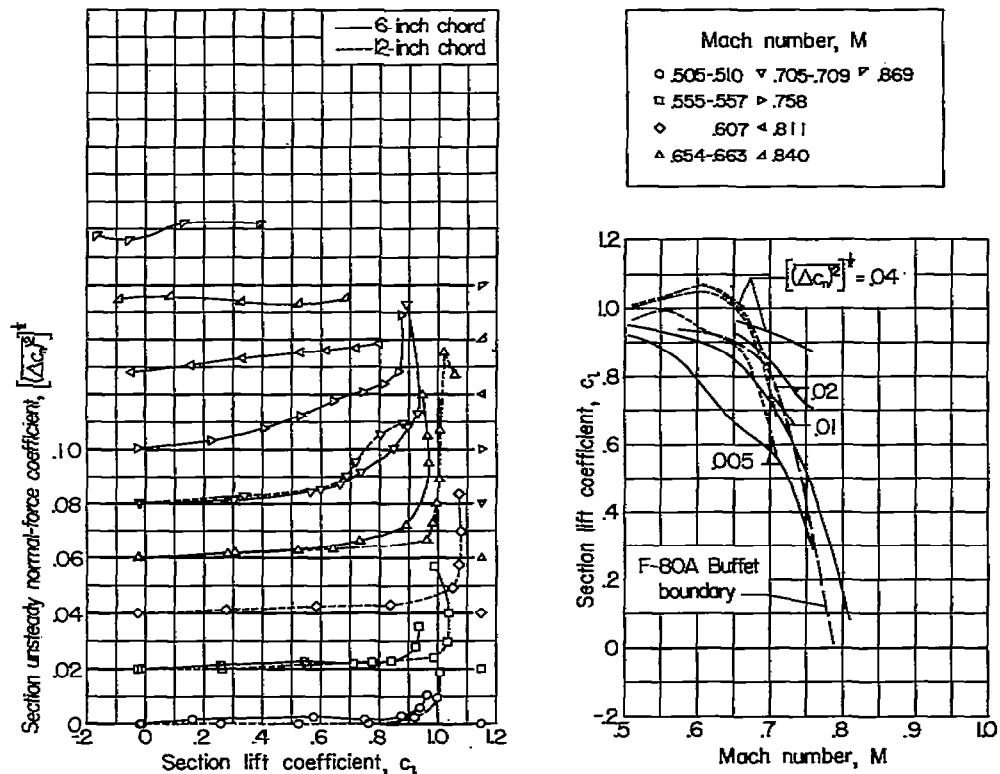


(c) Section unsteady normal-force coefficient contours.

Figure 41.- Comparison of the lift and unsteady normal-force characteristics of 6-inch- and 12-inch-chord NACA 23013 profile.



(a) Variation of section lift coefficient with section angle of attack for various Mach numbers.



(b) Variation of section unsteady normal-force coefficient with section lift coefficient for various Mach numbers.

(c) Section unsteady normal-force coefficient contours.

Figure 42.- Comparison of the lift and unsteady normal-force characteristics of 6-inch- and 12-inch-chord NACA 65-213,  $\alpha = 0.5$  profile.

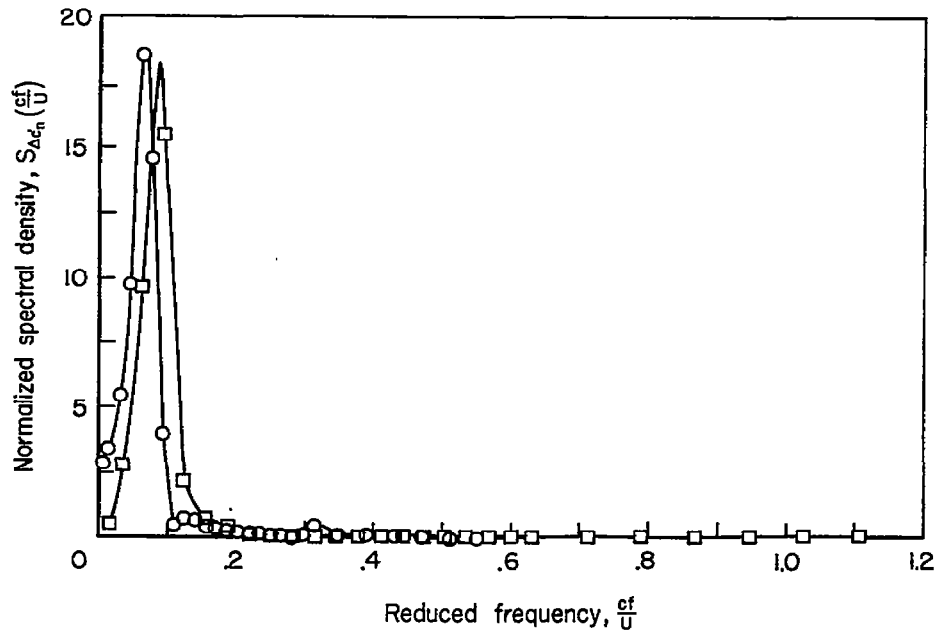
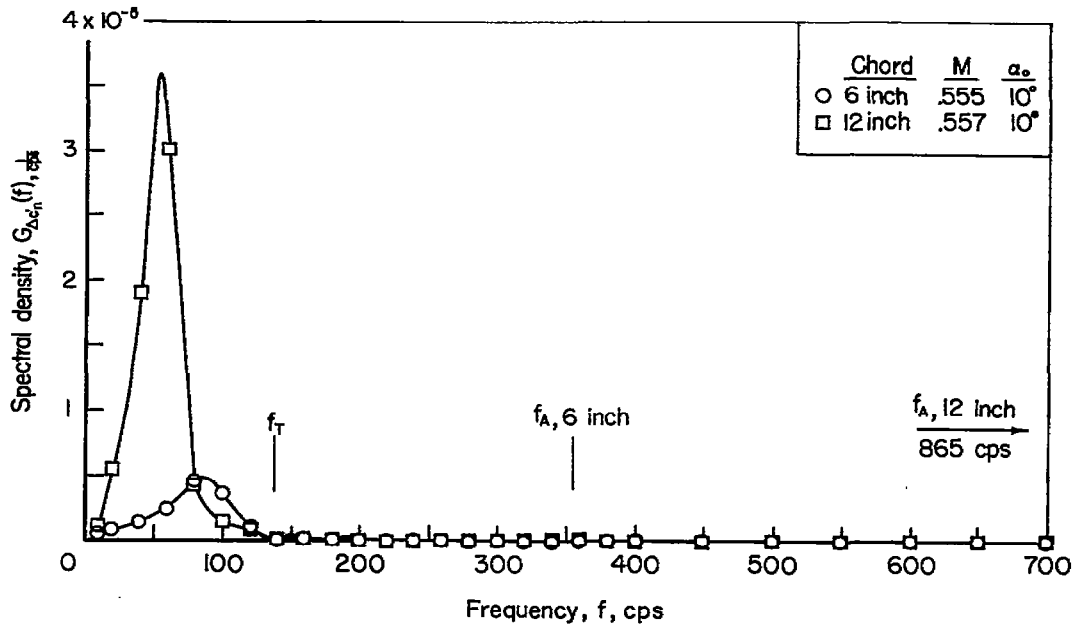


Figure 43.- Comparison of absolute and normalized spectral densities of the 6-inch- and 12-inch-chord NACA 65-213,  $\alpha = 0.5$  profile.

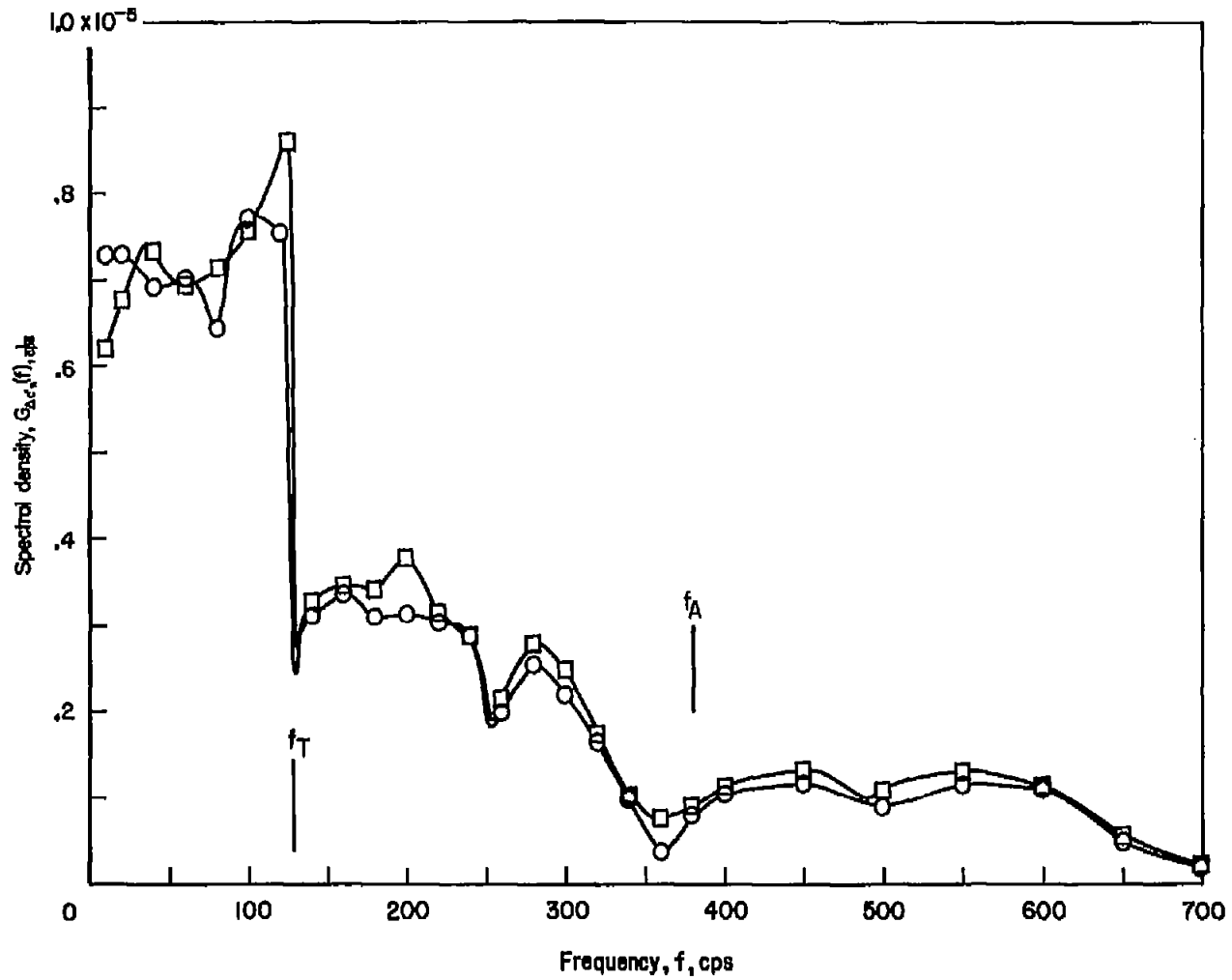


Figure 44.- Comparison of spectral densities measured under identical test conditions and different times; NACA 23013 profile,  $M = 0.655$ ,  $c_l = 0.73$ .

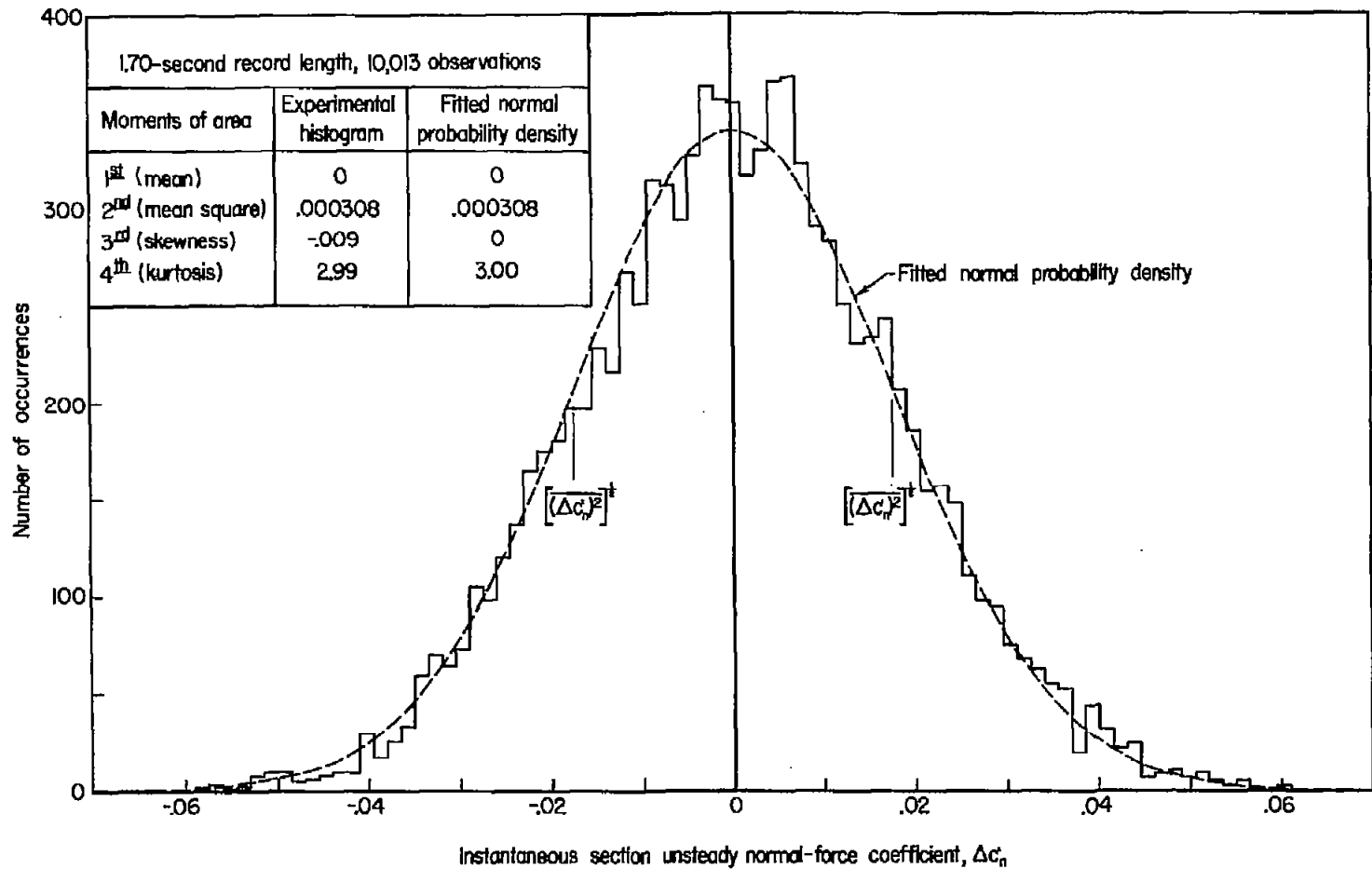


Figure 45.- Histogram of an unsteady normal-force coefficient, and comparison with a fitted normal probability density; NACA 65-213,  $\alpha = 0.5$  profile,  $M = 0.555$ ,  $c_l = 0.93$ .

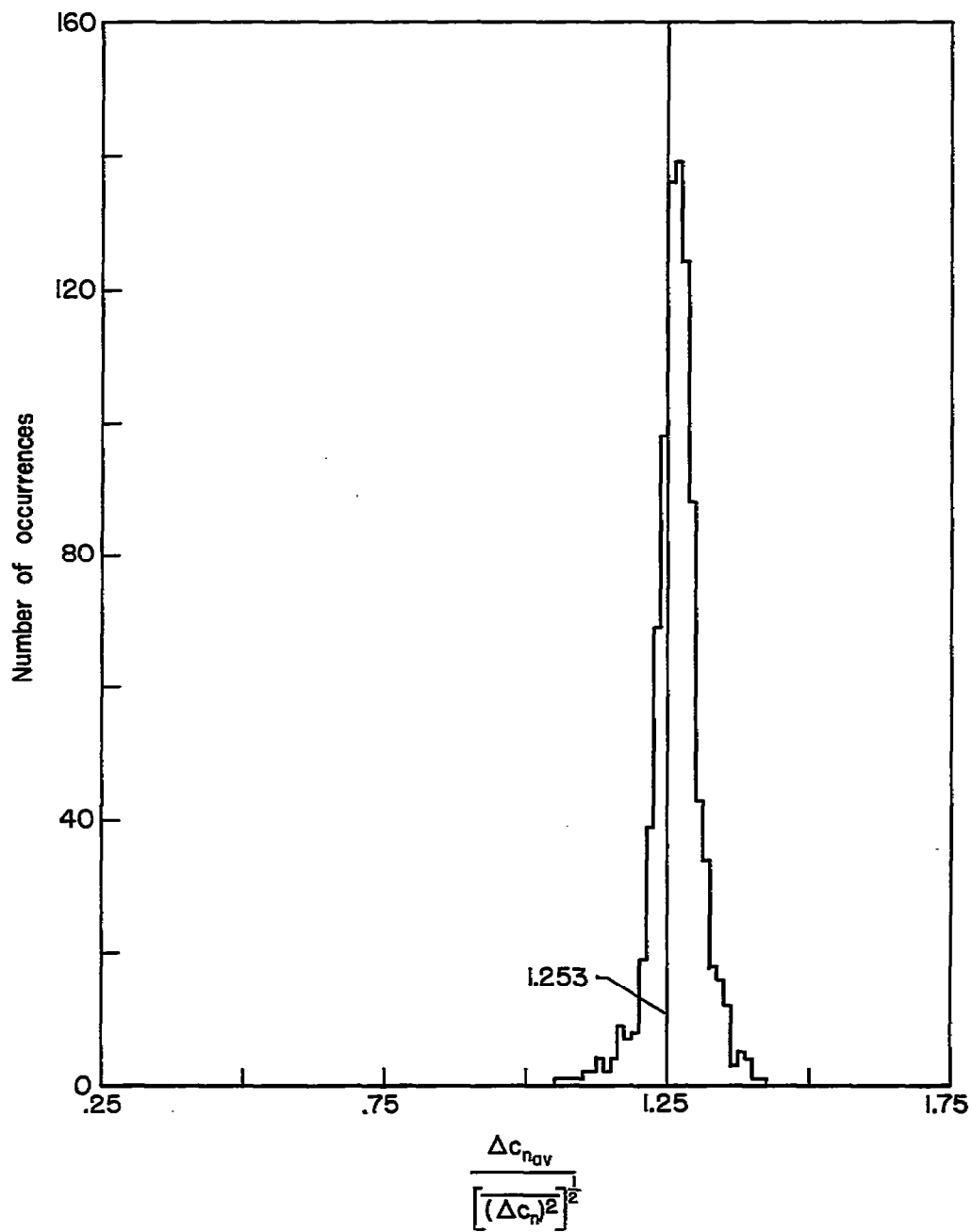
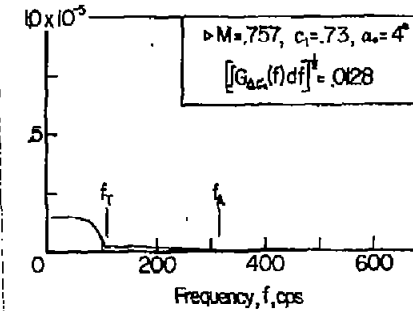
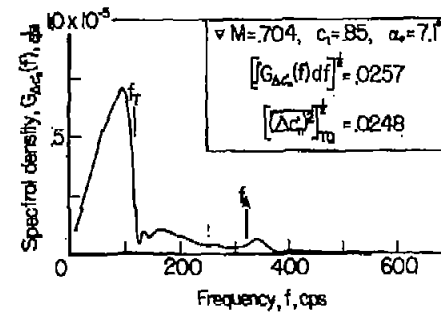
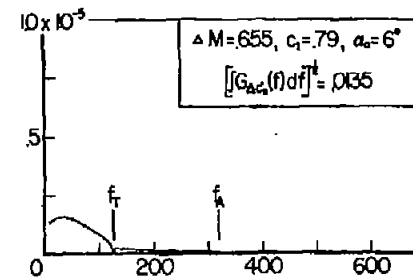
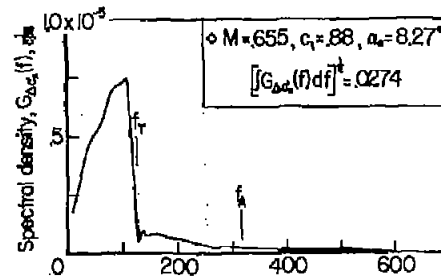
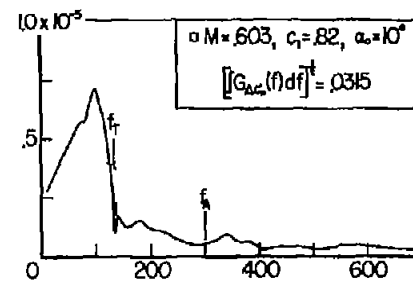
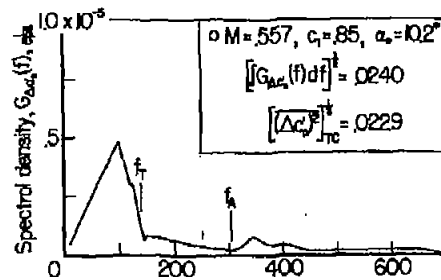
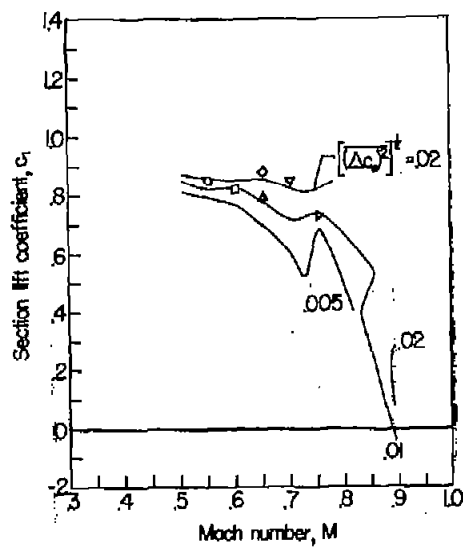


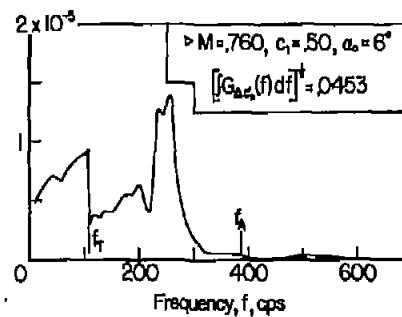
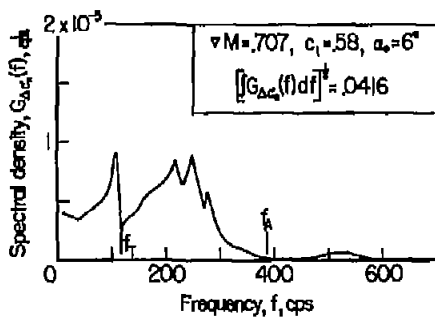
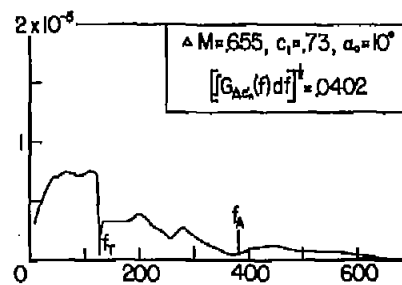
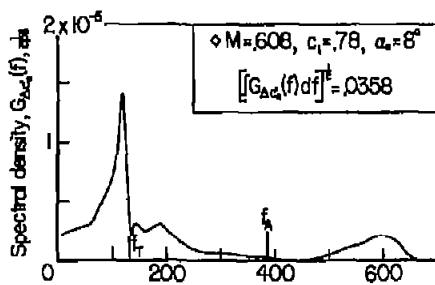
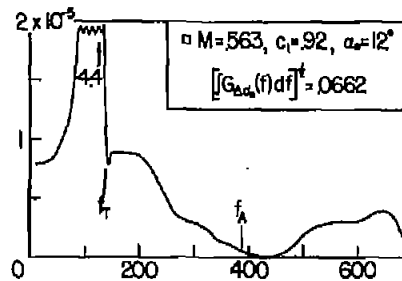
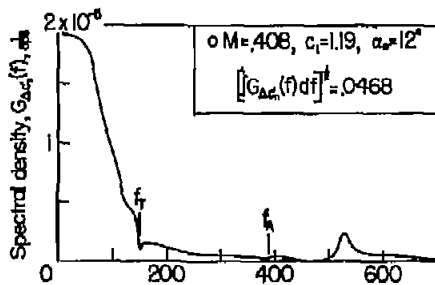
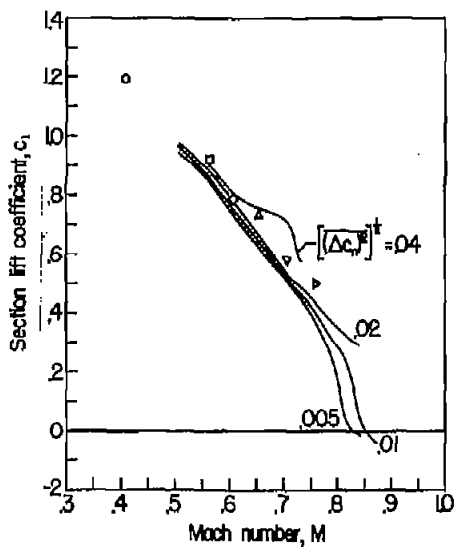
Figure 46.- Histogram of the ratio of the mean of the absolute value of unsteady normal-force coefficient to the root mean square for 887 simultaneous comparisons from nine profiles.



NACA 65-110 profile.

(a) NACA 65-110 profile.

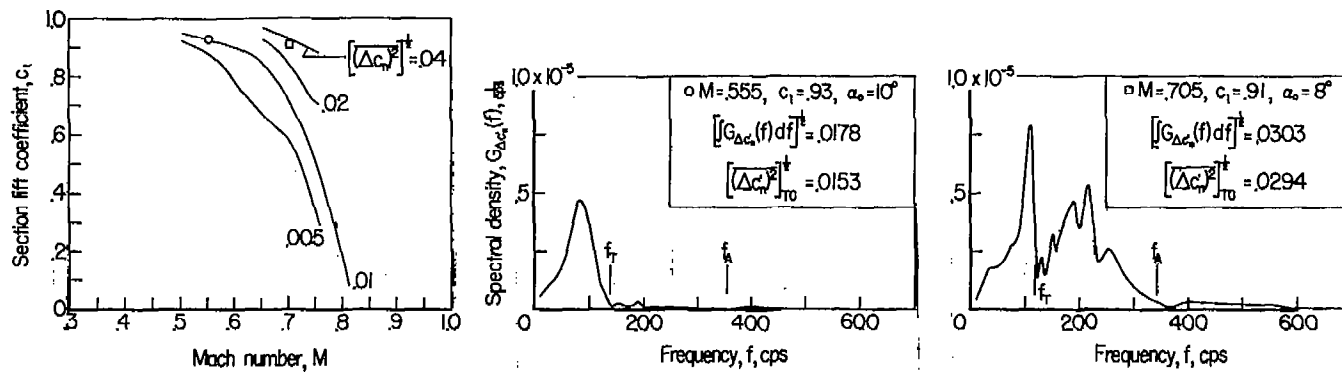
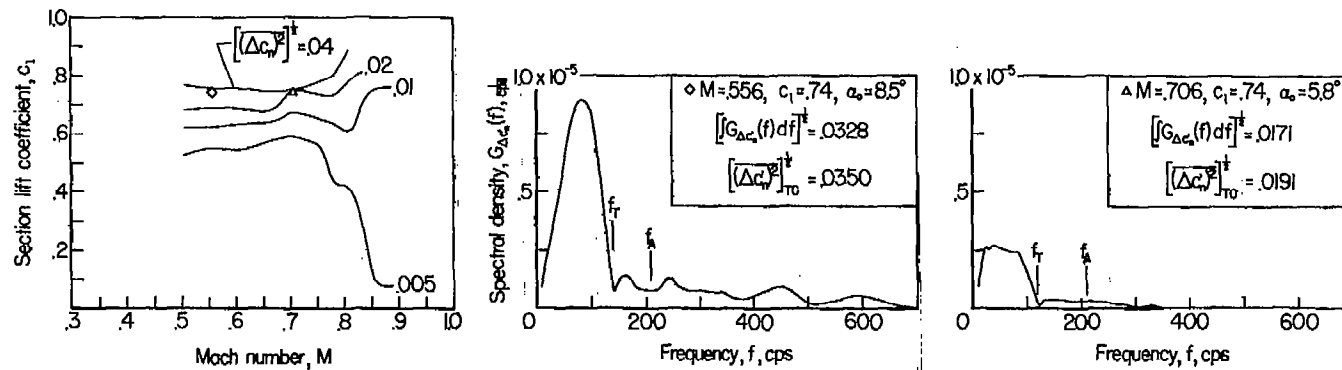
Figure 47.- Spectral densities of the unsteady normal-force coefficient.



NACA 23013 profile.

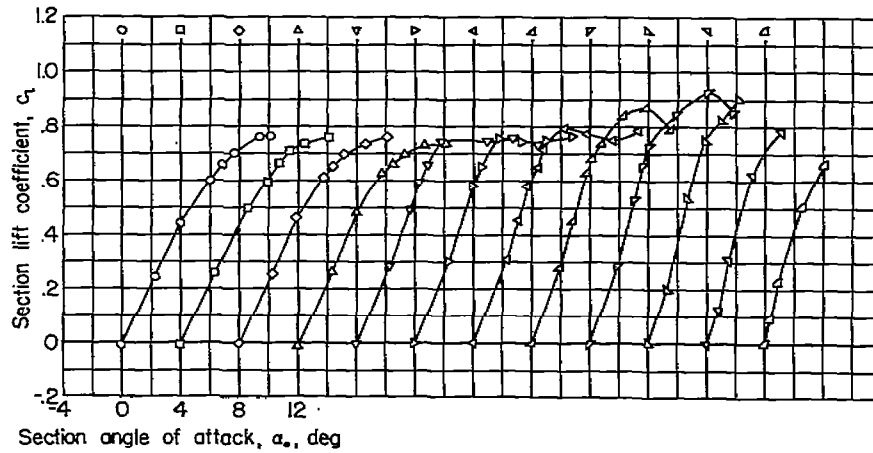
(b) NACA 23013 profile.

Figure 47.- Continued.

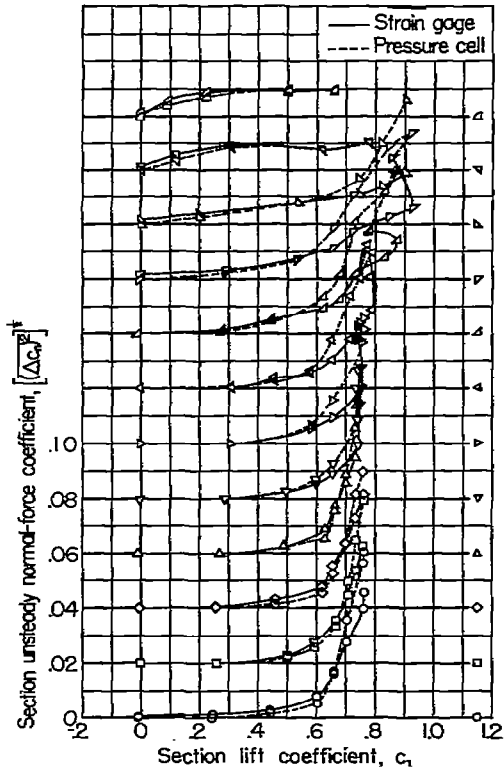
(c) NACA 65-213,  $a = 0.5$  profile

(d) NACA 0006-64 profile.

Figure 47.- Concluded.

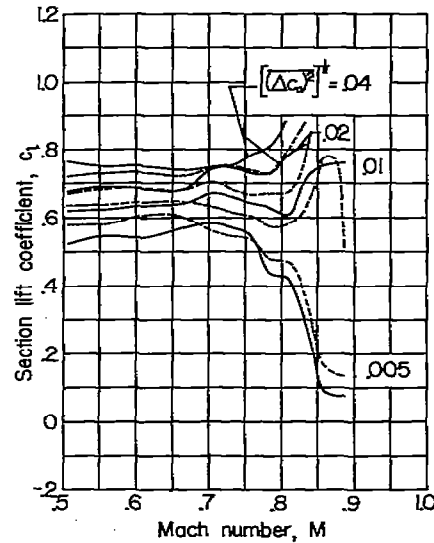


(a) Variation of section lift coefficient with section angle of attack for various Mach numbers.



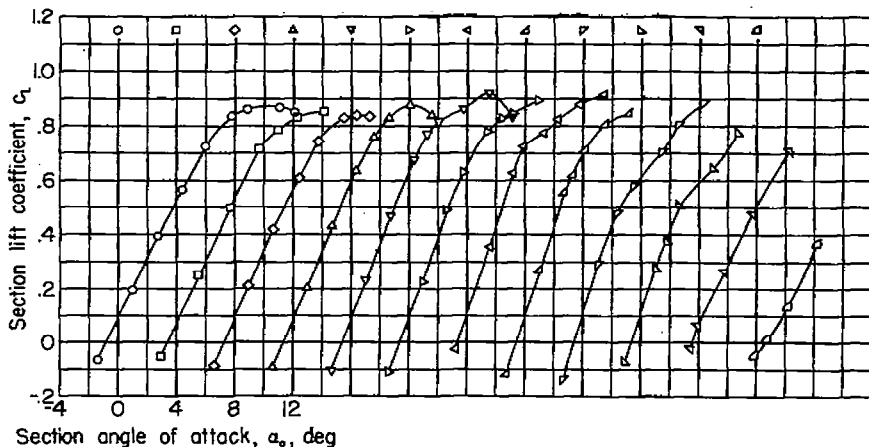
(b) Variation of section unsteady normal-force coefficient with section lift coefficient for various Mach numbers.

Mach number, M		
○ 506	▽ 706	▷ 807
□ 556	▷ 731	△ 832
◇ 607	◁ 755	▽ 857
△ 655	△ 782	△ 886

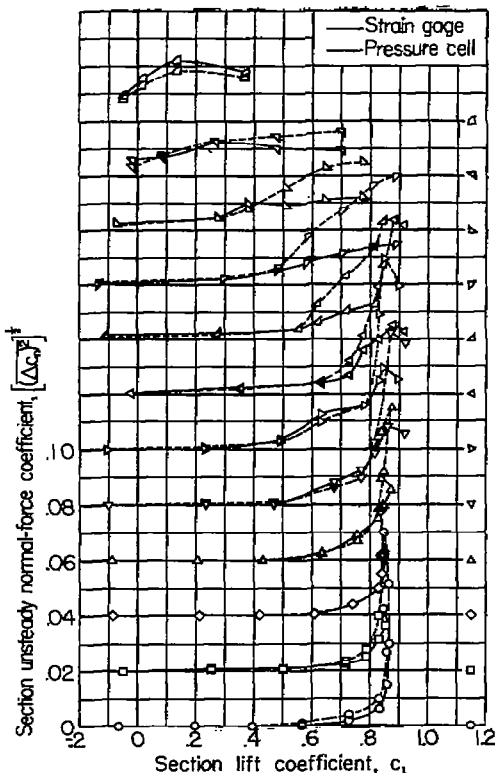


(c) Section unsteady normal-force coefficient contours.

Figure 48.- Comparison of unsteady normal-force characteristics measured with the pressure cells and with the strain gage; NACA 0006-64 profile.

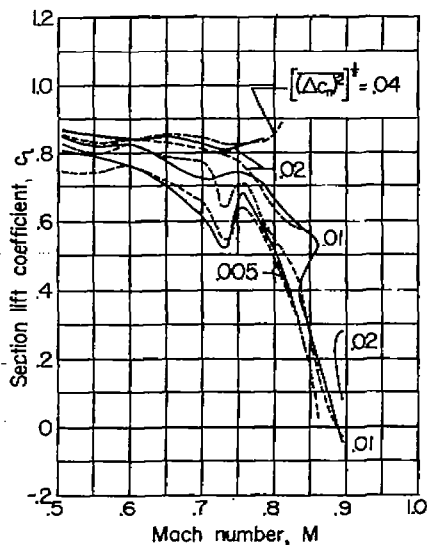


(a) Variation of section lift coefficient with section angle of attack for various Mach numbers.



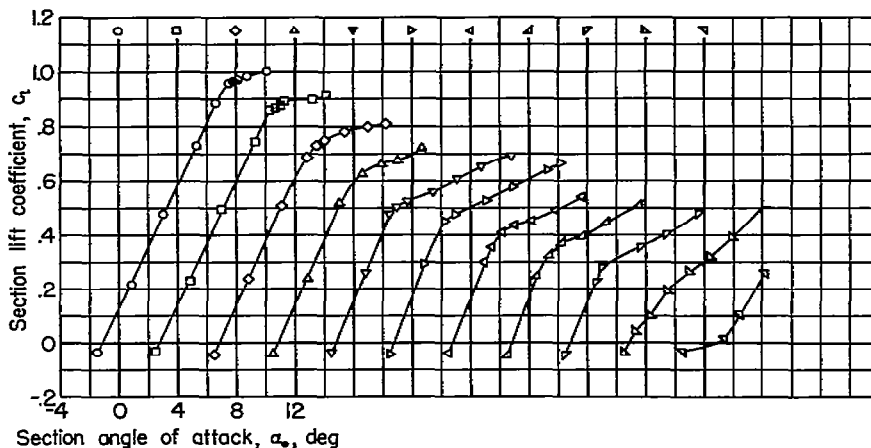
(b) Variation of section unsteady normal-force coefficient with section lift coefficient for various Mach numbers.

Mach number, M		
○ 507	▽ 704	▷ 809
□ 557	▷ 731	△ 835
◇ 603	◀ 757	▽ 862
△ 655	△ 783	△ 894

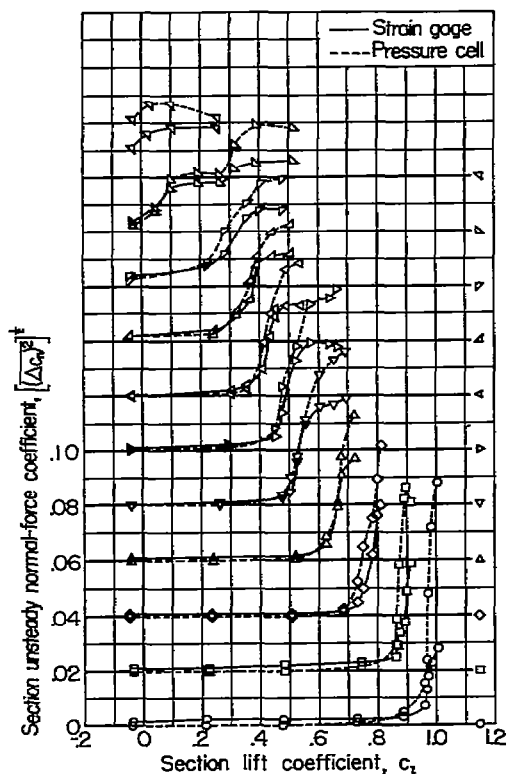


(c) Section unsteady normal-force coefficient contours.

Figure 49.- Comparison of unsteady normal-force characteristics measured with the pressure cells and with the strain gage; NACA 65-110 profile.

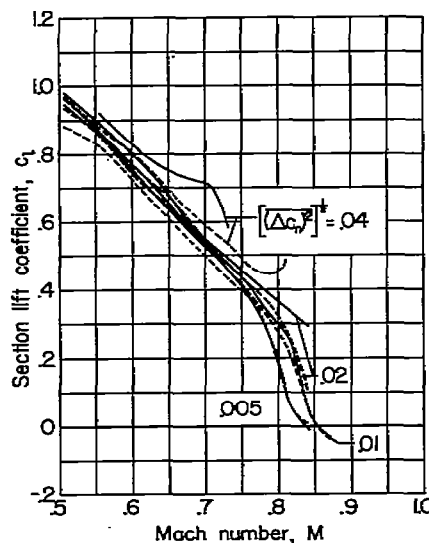


(a) Variation of section lift coefficient with section angle of attack for various Mach numbers.



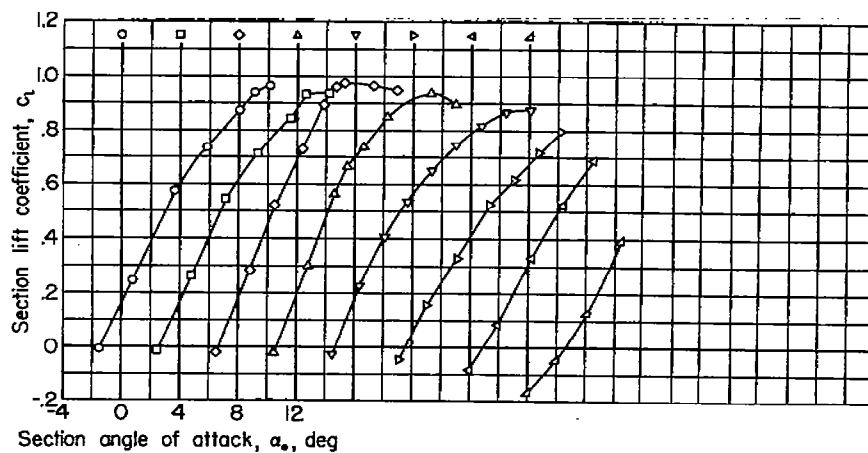
(b) Variation of section unsteady normal-force coefficient with section lift coefficient for various Mach numbers.

Mach number, M		
○ .507	▽ .707	▽ .812
□ .556	▷ .733	▷ .840
◇ .608	◁ .760	◁ .871
△ .655	△ .785	

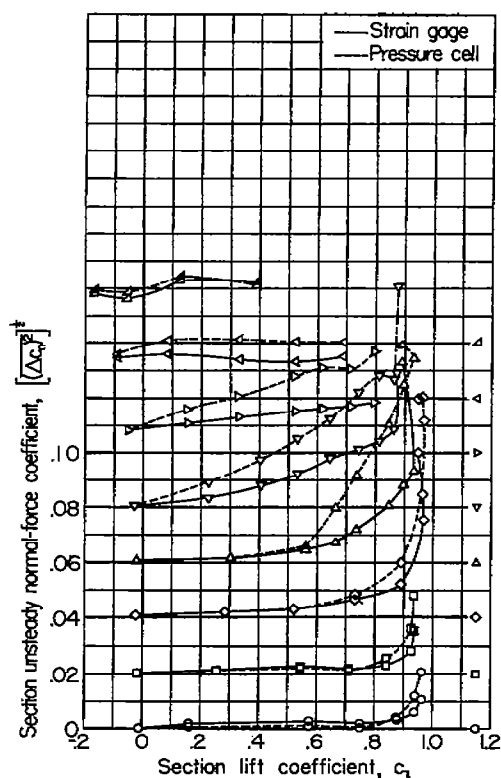


(c) Section unsteady normal-force coefficient contours.

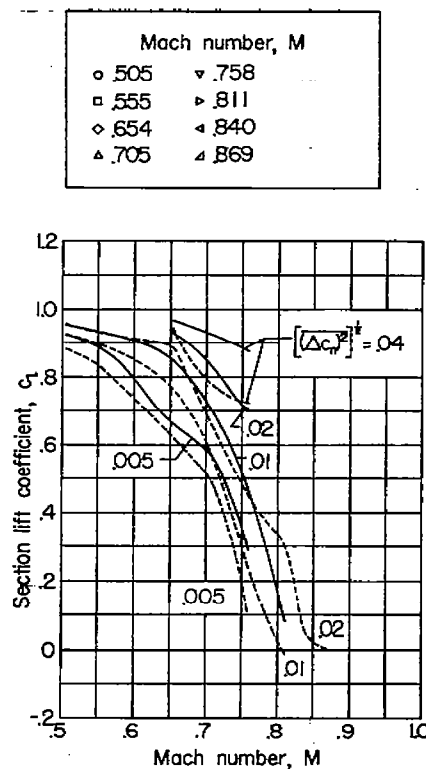
Figure 50.- Comparison of unsteady normal-force characteristics measured with the pressure cells and with the strain gage; NACA 23013 profile.



(a) Variation of section lift coefficient with section angle of attack for various Mach numbers.



(b) Variation of section unsteady normal-force coefficient with section lift coefficient for various Mach numbers.



(c) Section unsteady normal-force coefficient contours.

Figure 51.- Comparison of unsteady normal-force characteristics measured with the pressure cells and with the strain gage; NACA 65-213,  $\alpha = 0.5$  profile.

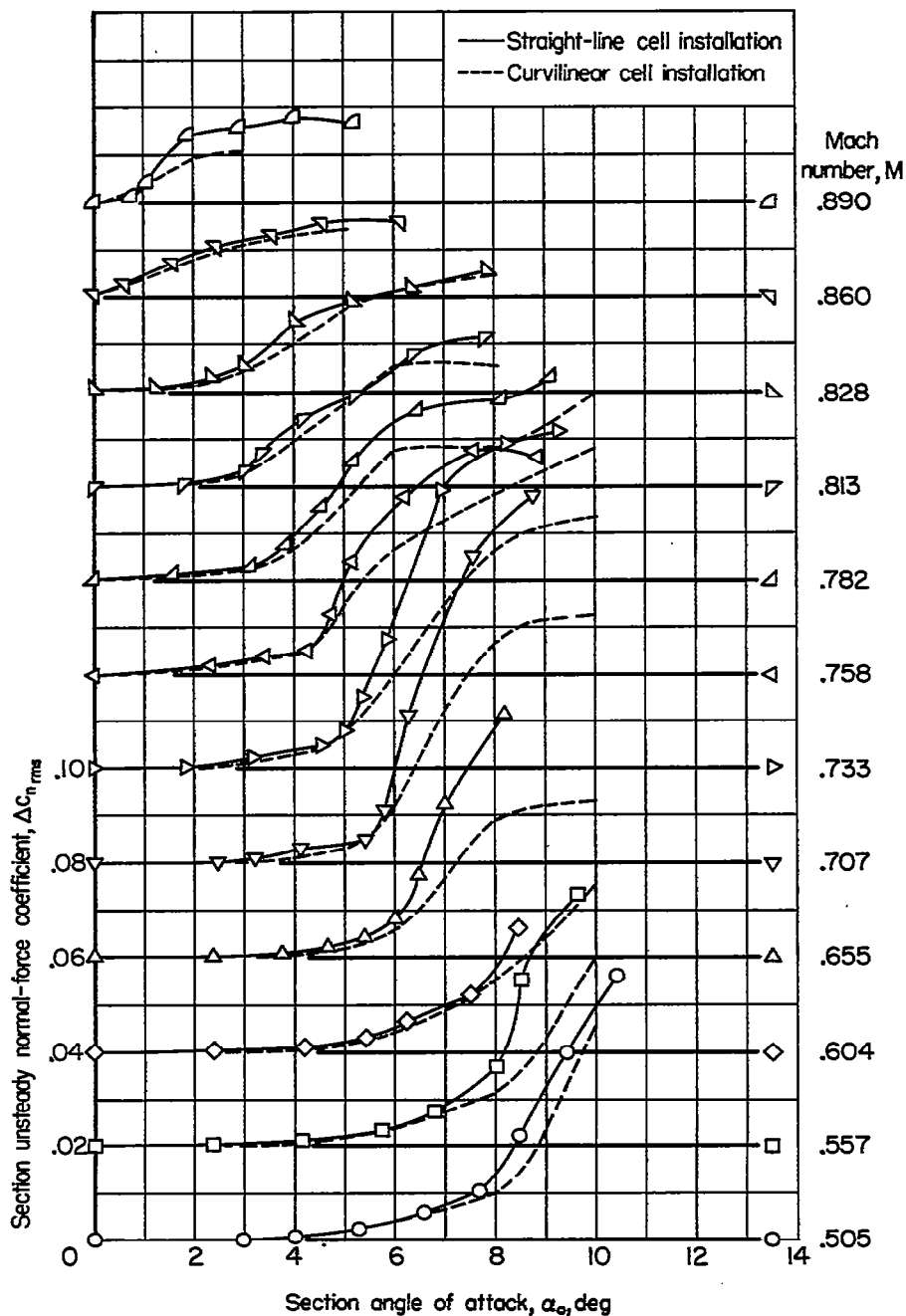


Figure 52.- Comparison of unsteady normal-force coefficients measured with the straight-line and with the curvilinear pressure-cell installations; NACA 65-010 profile.

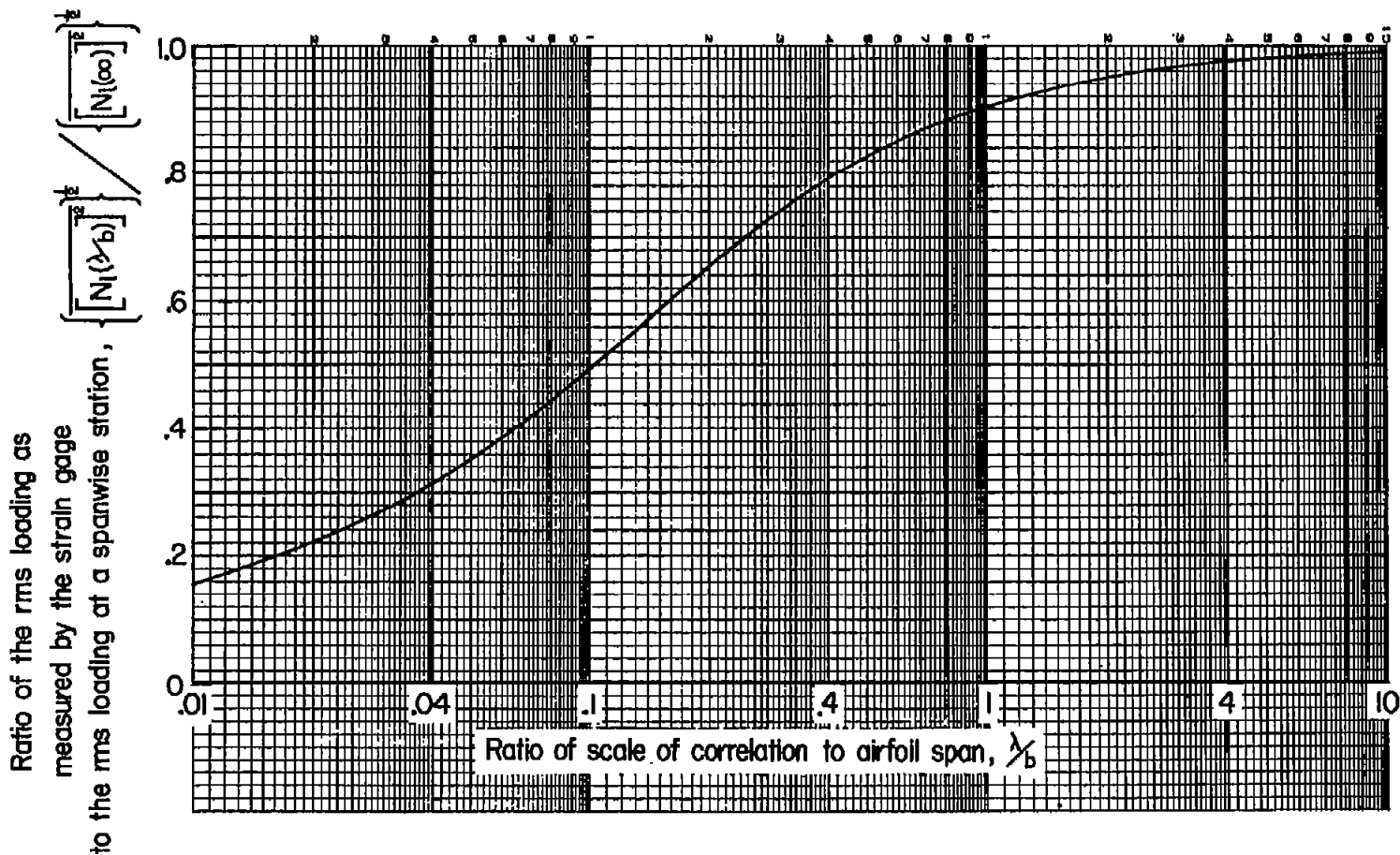
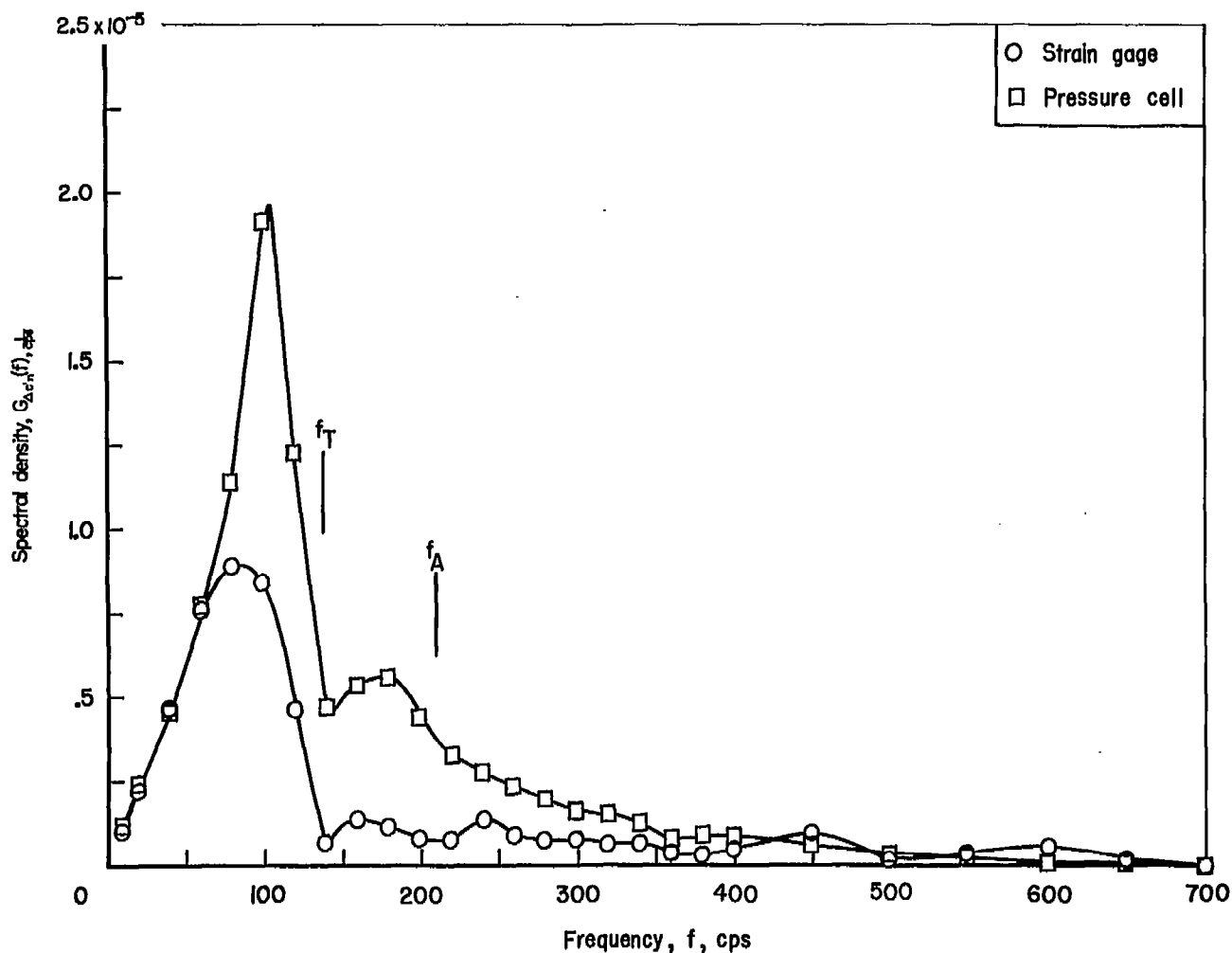
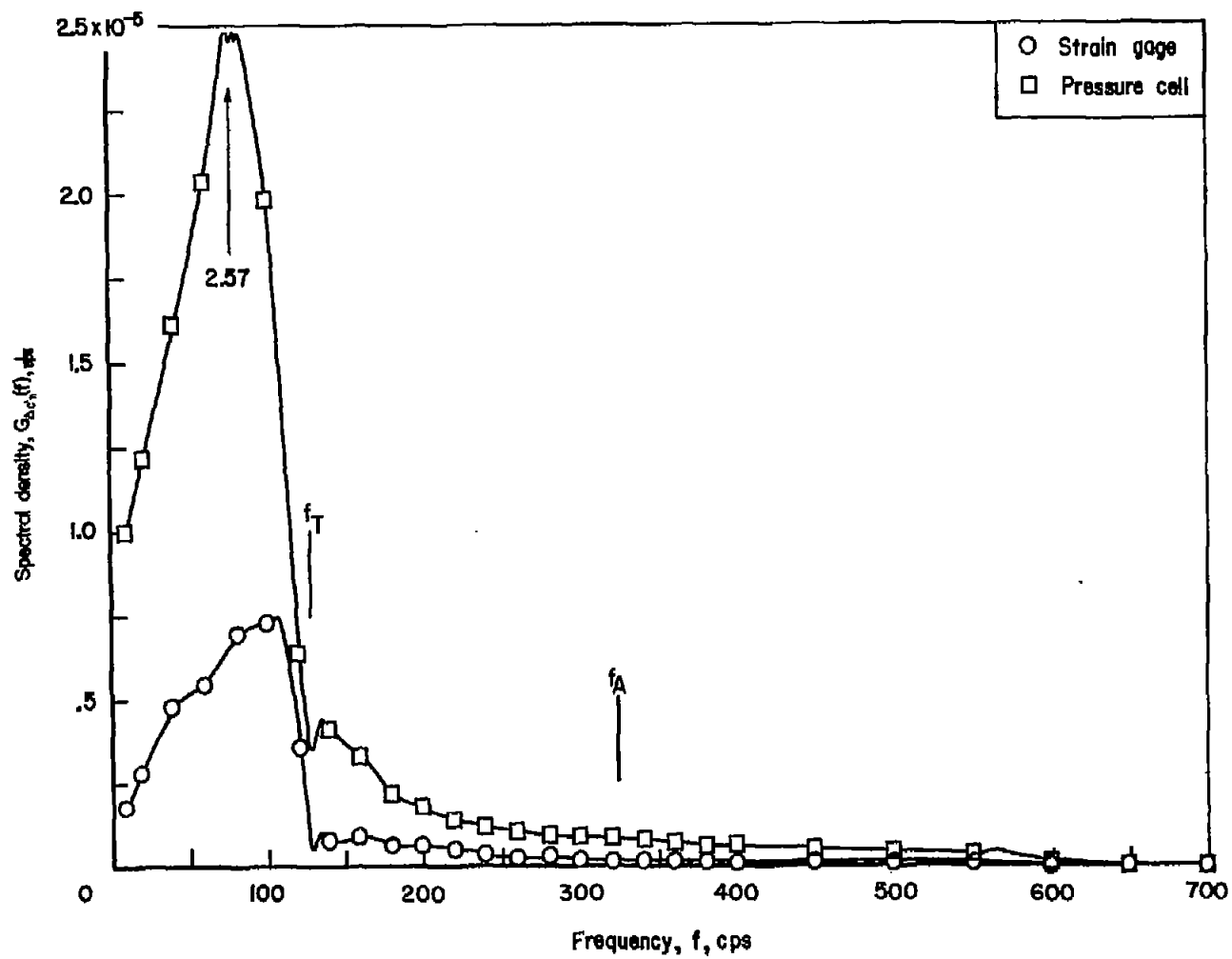


Figure 53.- Estimated effect of the spanwise scale of correlation upon the unsteady normal-force measurements of the strain gage.



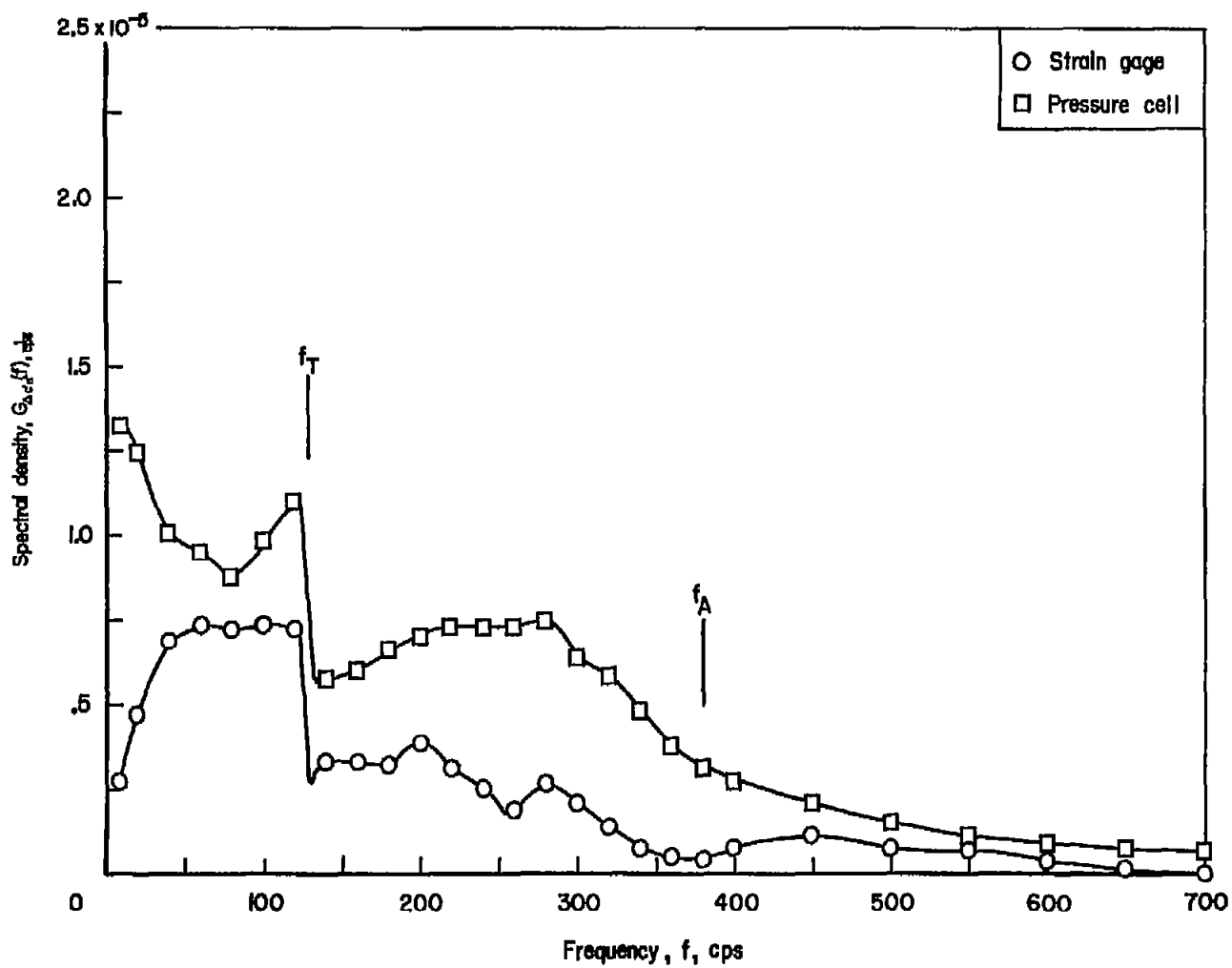
(a) NACA 0006-64 profile,  $M = 0.556$ ,  $c_l = 0.74$ .

Figure 54.- Spectral densities of unsteady normal-force coefficient measured with the pressure cells and with the strain gage.



(b) NACA 65-110 profile,  $M = 0.655$ ,  $c_l = 0.88$ .

Figure 54.- Continued.



(c) NACA 23013 profile,  $M = 0.655$ ,  $c_l = 0.73$ .

Figure 54.- Concluded.

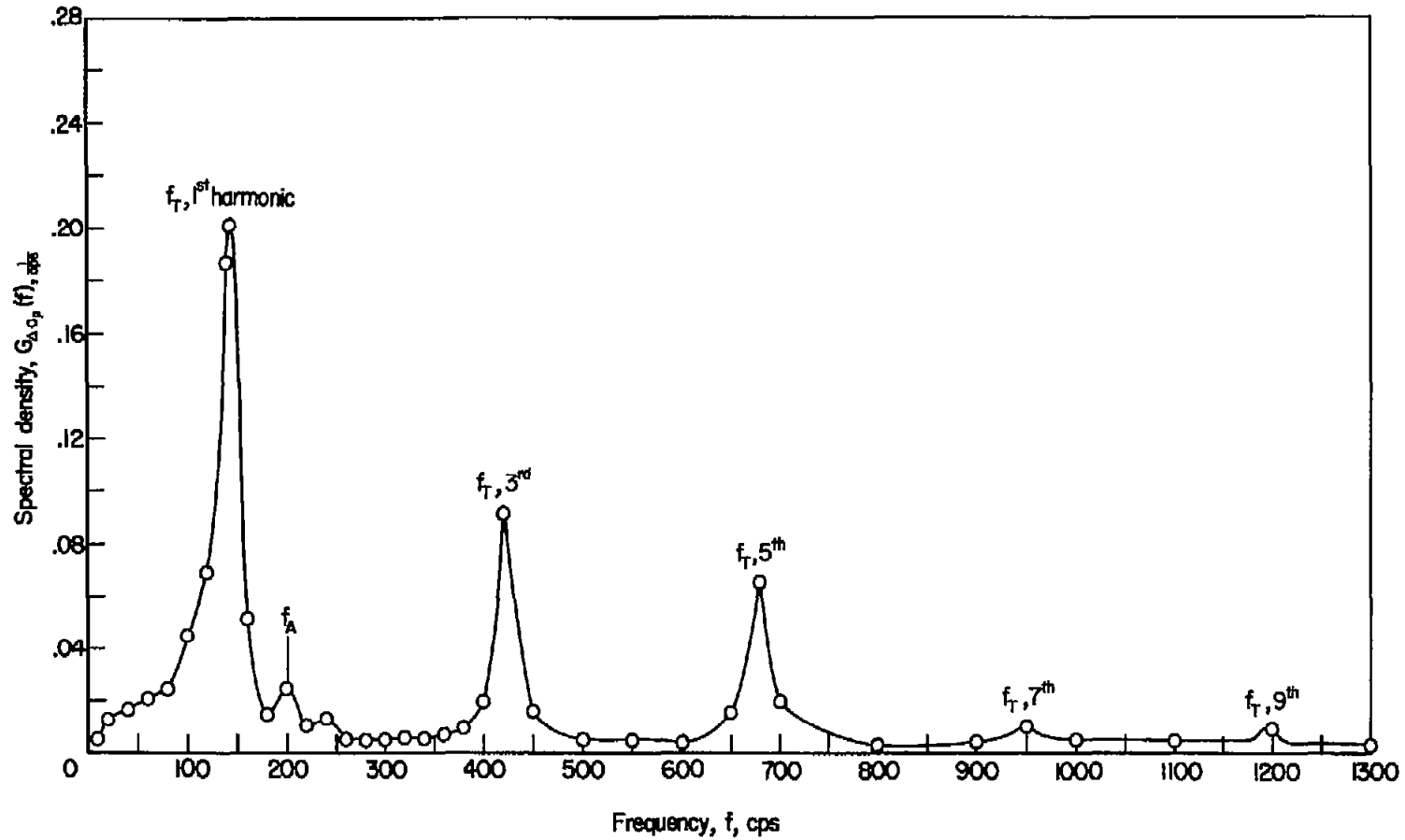


Figure 55.- Spectral density of the pressure coefficient measured with floor and ceiling pressure cells; NACA 0006-64 profile,  $M = 0.556$ ,  $c_l = 0.74$ .